Proceedings of the

☆ ☆ ☆ ☆ ☆ ☆ ☆

OAR

5 April 1966

RESEARCH APPLICATIONS CONFERENCE

OFFICE OF AEROSPACE RESEARCH

STATE DEPARTMENT ★ Main Conference Room ★ Washington, D.C.

Proceedings of the OAR

5 April 1966

★ ★ ★ ★ ★ ★ ★

RESEARCH APPLICATIONS CONFERENCE

OFFICE OF AEROSPACE RESEARCH

OFFICE OF AEROSPACE RESEARCH

UNITED STATES AIR FORCE, WASHINGTON, D. C.

FOREWORD

The publication of the proceedings of the first Research

Applications Conference of the Office of Aerospace Research (OAR)

is one way of demonstrating the unique applications that have

resulted from basic research by the United States Air Force.

The OAR is the prime research agency of the U. S. Air Force.

As such, it is responsible for conducting research within its own

laboratories, and for sponsoring scientific research in the

laboratories of universities, technical institutions and other research

organizations.

The principal product of the OAR is scientific information that is

relevant to the intrinsic needs of the Air Force. However, this

information becomes valuable only when it is used to improve

present Air Force weapon systems and to create new systems. The

applications and potential applications of OAR research results are

the subjects of these proceedings.

Ernest A. Pinson

ERNEST A. PINSON
Brig Gen, USAF
Commander

INTRODUCTION

The Office of Aerospace Research (OAR) - Research Applications Conference is held to acquaint senior government officials in the Washington, D. C. area with research and development contributions made by the OAR to the Air Force and other DOD agencies. It is particularly intended to demonstrate by specific examples the many ways that OAR basic research results are applied to the solution of DOD technical problems.

Most of the research applications papers presented at this conference have the following unique property: The solution to the problem was based upon basic research that was not necessarily oriented toward the problem it ultimately solved. This feature of the conference papers emphasizes an important advantage of maintaining a fundamental research effort in the DOD. New ideas, properly researched, evaluated and reported can greatly reduce the time-to-solution of unanticipated technical problems. Having the full time employment of gifted, experienced, loyal scientists who understand Air Force and DOD problems is an asset of inestimable value.

The examples to follow indicate a few of the research applications that have been made possible by OAR research and provides insight into what may be accomplished in the future with a strong fundamental research program.

HQ USAF

OAR

HQ OFFICE OF
AEROSPACE RESEARCH

Washington, D.C.

Manages the conduct and support of research in those areas which offer the greatest potential for providing new knowledge essential to the continued superiority of the Air Force operational capability. Also manages the conduct and support of specifically assigned exploratory-development efforts.
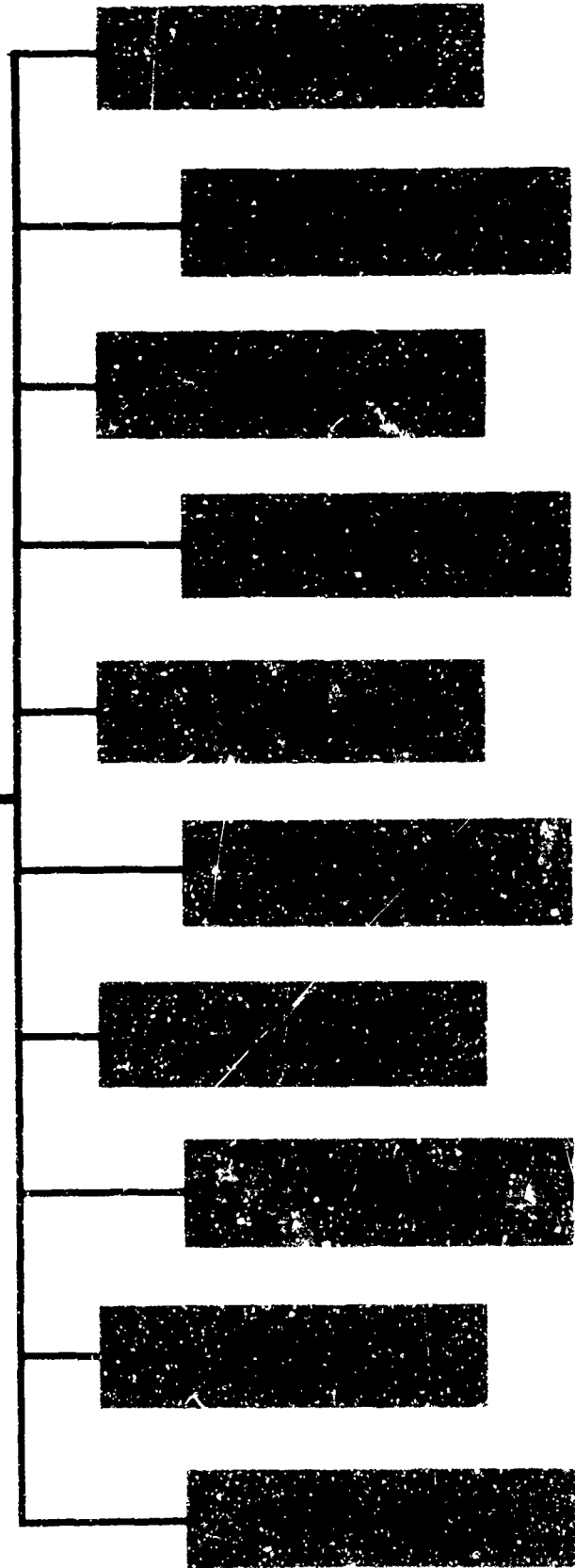
AFCRL

The Air Force Cambridge Research Laboratories, L.G. Hanscom Field, Mass., constitute the Air Force focal point for research in the environmental sciences. These nine AFCRL laboratories also provide a major in-house facility for research in the physical and engineering sciences. They conduct a large and varied research program, including research in all of the environmental sciences, in the physical sciences--primarily radio physics, gaseous and plasma physics, solid-state electronics, quantum electronics, and mathematics; and in the engineering sciences--primarily energy conversion. They also do exploratory-development work in the environment and aerospace environment. Although the primary function of AFCRL is to conduct research within its in-house laboratories, research under contract to outside agencies is used to support the research being carried out by the AFCRL scientists.

AFOSR

The Air Force Office of Scientific Research, located in Washington, D.C., supports extramural research to provide new knowledge and understanding in those sciences which offer the greatest potential for improving the Air Force's present and future operational capability.

As the major Air Force activity for sponsoring fundamental research in the sciences, AFOSR plans, directs, and carries out its research program through more than 1,200 grants and contracts with about 200 colleges, universities, and research organizations in the United States and abroad. Research is supported in nuclear and general physics, chemistry, mathematics, electronics, mechanics, energy conversion, astronomy-astrophysics, and the behavioral, biological, and information sciences. The kind of research sought is fundamentally a quality item.

AFOSR programs may be thought of as supporting research in areas keyed to recognized Air Force problems, as pioneering research which may lead to new technologies or concepts to meet unforseen Air Force requirements, and as providing a window for looking into world-wide science in order to enable the Air Force to draw upon scientific knowledge and ability for future development and application.

ARL

The Aerospace Research Laboratories at Wright-Patterson Air Force Base, Ohio, form a major Air Force in-house research facility in the following areas: physical and engineering sciences, including general physics; solid-state physics; general chemistry; physical chemistry; fluid dynamics; flight mechanics; mechanics of solids and energetics; and theoretical and applied mathematics. Although the primary function of ARL is to conduct research within its in-house laboratories, research under contract with outside agencies is used to support the research being carried out by ARL scientists.

FJSRL

The Frank J. Seiler Research Laboratory at the U.S. Air Force Academy, Colo., is an in-house facility in an academic setting engaged in research in the physical and engineering sciences--primarily general chemistry, physical chemistry, mathematics, fluid dynamics, and flight mechanics.

ORA

At Holloman Air Force Base, N. Mex., the Office of Research Analyses performs analysis and evaluation of future Air Force systems. Under OAR direction, these technically complex studies are made for any Air Force activity. Particularly significant is the fact that they are independent studies. Through this study activity, OAR is provided with critical technology needs which are incorporated into the research program.

EOAR

Since the pursuit of knowledge transcends national boundaries and geographical divisions, the OAR sponsorship of research extends throughout the free world. The purpose of this involvement is to capitalize on the free world's best brainpower with its fresh ideas. In addition, OAR utilizes the unique sources of R. & D. capabilities and takes advantage of a particular geographical location.

The European Office of Aerospace Research, located in Brussels, Belgium, is responsible for the administration of contracts and grants in Free Europe, the Near East, and Africa. All funds for the support of foreign R. & D. come from stateside laboratories as a part of their total programs.

LAOAR

The Latin American Office of Aerospace Research, located in Rio de Janeiro, Brazil, administers the research efforts in South America.

Proposals from researchers located either in Europe or Latin America should be sent to EOAR or LAOAR, respectively.

PFOAR   VFOAR   LOOAR

Other supporting aerospace-research organizations are the field offices located at Patrick Air Force Base, Fla.; Vandenberg Air Force Base, Calif.; and the Los Angeles offices. These field offices maintain liaison among the scientist, the launch team, and the contractors. As a result, small scientific experiments are installed on rockets fired for other purposes, thus insuring that the Air Force receives maximum pay-load utilization.

Conference
Papers

Captain Rinaldo F. Vachino is assigned to the Frank J. Seiler Research Laboratory. Prior to his transfer to FJSRL, Captain Vachino worked with the Synthesis and Analysis Division, Directorate of Engineering, Wright-Patterson AFB, Ohio. where he participated in studies of stability and control of winged and re-entry vehicles, operational evaluations of STOL and VTOL aircraft, and B-70 penetration studies. He received his B.S. in Electrical Engineering from Newark College of Engineering, and his M.S. from the Air Force Institute of Technology. He has completed course requirements for a Ph. D. in Astronautical Engineering at the University of Michigan. The first draft of his dissertation is finished, and the results are being applied to the solution of a number of optimization problems.

A COMPUTATIONAL PROCEDURE FOR OPTIMUM TRAJECTORY AND OPTIMAL CONTROL PROBLEMS

Rinaldo F. Vachino, Captain, USAF

FJSRL, OAR, USAF Academy, Colo 3064.

There are many problems in the field of trajectory optimization and optimal control that are of Air Force interest. One such problem concerns aircraft performance where the objective may be to maximize range, or minimize the time-to-climb of an aircraft within selected constraints. Another concerns injection of a payload into a given orbit while minimizing the propellant. For such a problem one must determine the best programming of the angle of thrust, and the optimal time to initiate coasting and the length of the coasting intervals.

These problems and others in many other fields can be formulated in identical mathematical terms. The resulting mathematical formulation is amenable to treatment by the calculus of variations or by the recent theory of the maximum principle. However, in general, these theories do not lead directly to a solution of the original problem. Instead they lead to another, nearly equivalent problem, the two-point boundary value problem.

In the past, these problems have usually been solved by trial and error methods. Within the last few years, a number of computational procedures aimed at solving these problems has been developed. One of these techniques is called the method of steepest descent [1] and is particularly adapted to digital computer solution of these problems. This method generates a sequence of approximations which converges to the optimum solution. The present paper discusses an extension of this method, provides an example of its application, and lists four typical applications to problems of Air Force interest. The mathematical details and rigor for this extension are found in reference [2].

The Method of Steepest Descent

The method of steepest descent is a systematic procedure which permits one to generate successive corrections to an initial control and change it to the desired optimum control. The usefulness of this technique and its modification can be described in general by considering the mathematical formulation of a problem that might arise in trajectory optimization. The starting point for the mathematical formulation is the system of differential equations satisfied along the flight path or

$$\dot{\vec{x}} = f(\vec{x}, \vec{u}, t) .$$

These equations relate velocities and positions, forces and accelerations, mass and flow of propellants, etc. In particular, $\bar{x}$ represents a vector whose components are state variables. These give the state of the system at any time and so represent the linear and angular positions and velocities of the system. The components of the vector $\bar{u}$ represent the control variables that one has at his disposal to control the system. These controls could be fin displacement, thrust magnitude, vernier engine angle, etc. The system is to change from its initial state to a final state in some optimum fashion, as by minimizing the total time elapsed or the fuel used. The objective of the optimization scheme is to choose the required control variables.

For such a problem the application of the method of steepest descent is easy and direct. One begins by assuming a set of curves which represent the optimum control. With this function one integrates the differential equation of the system until one of the terminal conditions is satisfied. At this point one evaluates the difference between the desired and the actual terminal values of the state variables. Next one perturbs the values of the control variables by a small amount and evaluates the cummulative effect of the instantaneous changes in these controls on the final value of the state variables. At this point one chooses the actual control variation that is most efficient in producing the necessary corrections to the terminal conditions. This variation in control, superimposed on the initial control, serves as a reference control for the next iteration. This procedure is then repeated until the optimum control is obtained.

The modification to the method is in the assumptions on the values chosen for the control variables. It is assumed that these values are bounded. This assumption makes the method applicable to realistic problems since limitations on the controls such as thrust magnitude, or gimbal angle always exist. Such a class of problems is then said to be characterized by inequality constraints on the control variables. In the presence of these constraints a wide class of problems has optimum solutions which are no longer one continuous function of time. Instead they are composed of a finite number of segments or functions, each of which is continuous. The times at which the control function switches from one to another of these adjacent segments are called switching times, and each of these segments is called a subarc.

An additional complexity in this type of problem arises from the fact that the exact occurrence of the switching times must also be determined optimally. Consequently, during the iterative process described in the preceding section one must also derive suitable variations for the switching times and modify them toward their optimum positions. The adaptation of the method of steepest descent that is the subject of this paper provides these iterative variations of the switching times, in an analogous manner to the iterative variations of the continuous components of the control vector.

Example

One application of this method is to the problem of transferring a point mass through a given distance over a flat surface, under the influence of a constant gravitational field, and in the absence of atmospheric and other disturbances. The problem might represent the translation of a moon explorer by means of a back pack along a quasi-parabolic trajectory, so that he departs and arrives with zero velocity. The object is to seek the minimum fuel trajectory traversed by the point mass from all the possible thrust profiles that will cause the point mass to execute the desired change of position.

The system is the point mass, whose state is described by the system of simultaneous differential equations.

$$
\begin{bmatrix} \dot{x} \\ \dot{y} \\ \dot{u} \\ \dot{v} \\ \dot{m} \end{bmatrix} = \begin{bmatrix} u \\ v \\ (T/m)\cos\alpha \\ (T/m)\sin\alpha - g \\ -T/c \end{bmatrix}
$$

where the state variables of the vector $\vec{x}$ are

$$
\begin{bmatrix} x \\ y \\ u \\ v \\ m \end{bmatrix} = \begin{bmatrix} \text{Horizontal displacement} \\ \text{Vertical displacement} \\ \text{Horizontal velocity} \\ \text{Vertical velocity} \\ \text{Mass} \end{bmatrix}
$$

the control variables of the vector $\bar{u}(t)$ are

$$
\begin{bmatrix} T(t) \\ \alpha(t) \end{bmatrix} = \begin{bmatrix} \text{Thrust magnitude control} \\ \text{Direction of thrust from horizontal} \end{bmatrix} ,
$$

c is the effective exhaust velocity and g is the local gravitational acceleration. The thrust acting on the point mass is subject to an inequality constraint that prescribes that the thrust shall be greater than zero but less than some maximum thrust.

Problems of this type exhibit a peculiar behavior. While the inequality constraint on the thrust simply stipulates that the thrust

4

cannot fall below its lower bound of zero, nor exceed its upper bound of
a maximum level of thrust, the actual optimum thrust takes on values
that correspond to one or the other of these two limits, that is, either
the thrust is on or off. Secondly one obtains the situation where the
thrust profile consists of three subarcs in the following order: Thrust-
Coast-Thrust. Thus one wishes to determine exactly when the thrust is
cut off and reignited, as well as the thrust angle as a function of time.
These are the aims of the optimization process.

The computational scheme considered in this study requires an
arbitrary choice of this thrust angle as a function of time and a choice
of times at which to switch the thrust off and then on again in order to
start the iterative process. It is clear that if these choices are truly
arbitrary then in all likelihood the point mass cannot be made to meet
the desired end conditions. Consequently the next aim is to modify this
initial choice so that there is a reduction of the difference between the
desired and the actual terminal conditions. With this arbitrary choice
of parameters, the computational scheme identifies the effect of a small
change of these functions on the terminal errors and on the cost index,
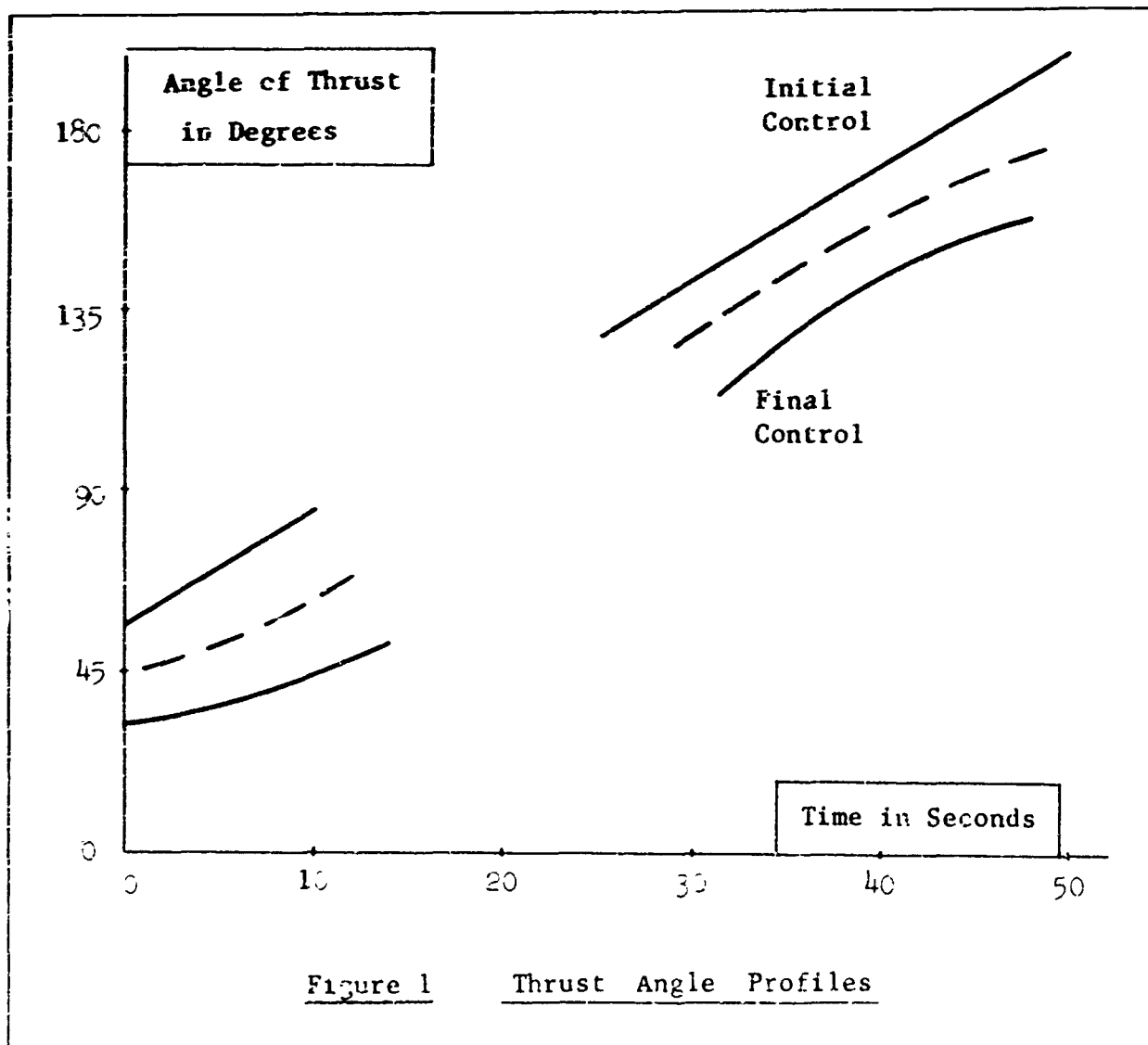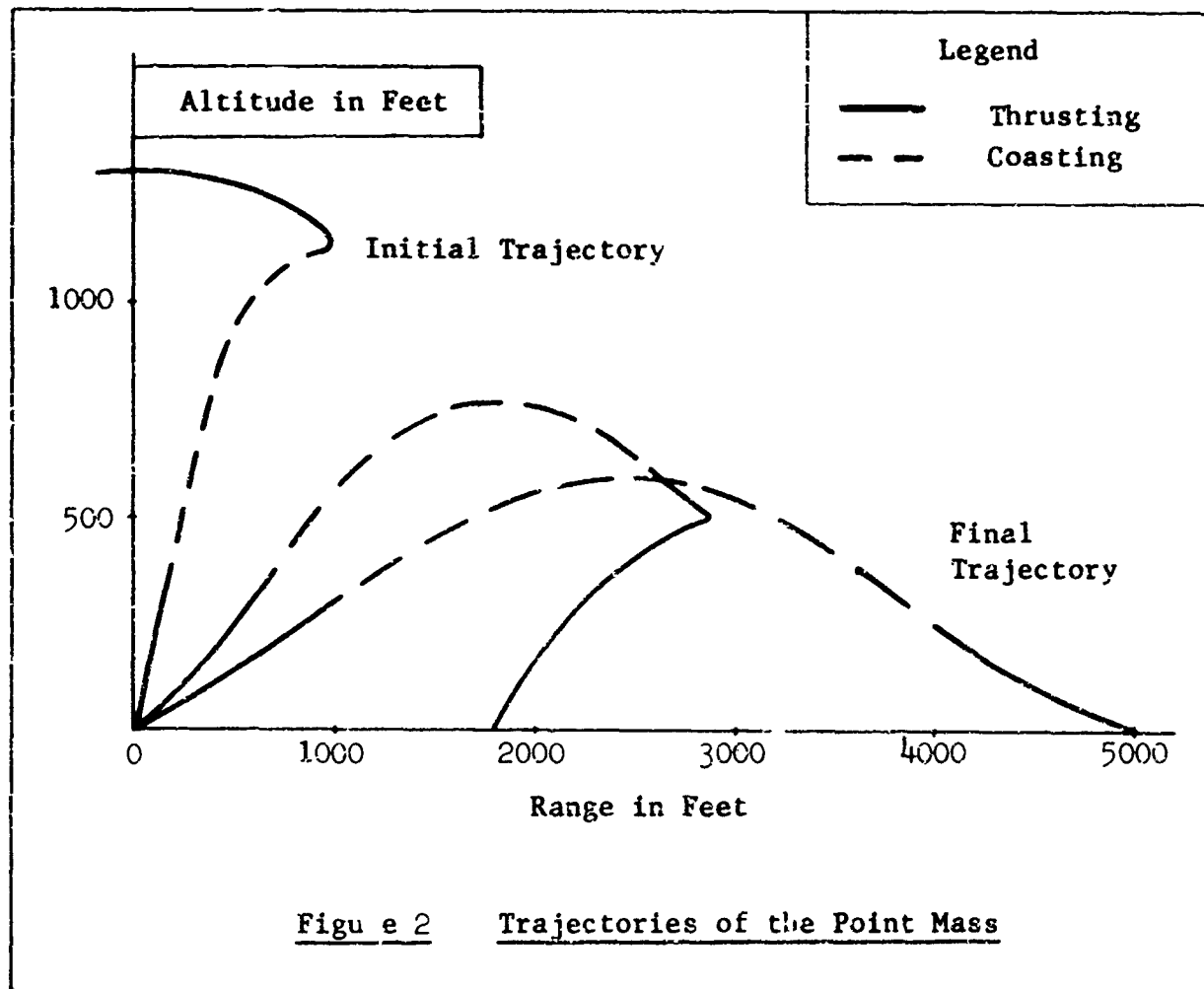and prescribes a modification in each of them.

Figure 1   Thrust Angle Profiles

Figu e 2   Trajectories of the Point Mass

In order to illustrate the solution of thi: problem with a specific example, consider that the point mass starts fr r rest with an initial weight of 248 moon pounds. It is desired that the point mass travel 5000 feet and land with zero velocity. In this prob em the final mass is unspecified, and is the object of the maximization process. Thus by maximizing the final mass, one minimizes the difference between the initial and final masses: this then is the cost index for this problem. The remaining four terminal conditions stipulate that the desired end conditions involve a range distance of 5000 feet, zero altitude, and a soft landing condition. Other constants assumed for the problem are: maximum thrust = 622 lbs, g = 5.27 ft/sec^2, c = 10,000 fps.

The curves in Figure 1 illustrate the gradual progression toward the optimal solution that one obtains by means of the technique described in this paper. The top curve, labeled "In tial Control" and composed of two segments of a straight line, is t f initial thrust angle, $\alpha(t)$, that was assumed in order to translate the point mass. The space between the two segments represents the coasting subarc, when the thrust is zero; consequently the angle of thrust has no significance during

this interval. The remaining two curves represent the thrust profile at two later stages during the convergence process. It can be noted that both the shape of the thrust curve and the times at which the corresponding coasting period begins and end have been modified. The curve labeled "Final Control" is somewhat a misnomer because it implies that it is the optimum solution. This is not the case, because the optimum solution can only be approached to within any desired accuracy, but can never be reached. Thus in practice one terminates the automated iterative computer process on the basis of numerical data associated with each curve. The data for this problem are tabulated in the accompanying table and are discussed presently.

Associated with each thrust profile illustrated in Figure 1, there is a corresponding trajectory which describes the path in terms of height and distance traversed by the point mass. Figure 2 illustrates these trajectories. It can be noted that the desired terminal point, at a range of 5000 feet, is to the right, and the starting point is at the origin of the coordinates. The initial trajectory shows that the point mass went in the opposite direction to that desired. This occurred because the initial thrust profile was assumed arbitrarily, without any prior knowledge of the behavior of the point mass in the gravitational field. The actual impact point was 4141 feet up-range, and since the desired impact point was at 5000 feet down-range, the miss distance is shown as 9141 feet in the accompanying table. The associated impact velocities are also shown. It can be noted from Figure 2 and the table that the other two trajectories have impact points that come monotonically closer to the desired one, and the impact velocities approach zero as a limit, which is the desired soft-landing criterion.

Table

Cycle	Fuel Used	Distance Error	Horizontal Impact Velocity	Vertical Impact Velocity	Gradient	Coasting Initiation	Coasting Termination
	slugs	ft	fps	fps		sec	sec
1	2.5977	9141	-330	-167	0.0301	10.0000	25.0000
30	2.0895	5047	-195	-120	0.0172	10.3500	28.2500
60	1.9985	3207	-120	- 97	0.0141	12.3500	29.9700
90	1.9689	2043	- 68	- 63	0.0089	13.7181	31.5301
120	1.8730	1230	- 35	- 33	0.0031	13.7965	31.4752
150	1.8121	782	- 9	- 12	0.0009	14.1077	31.1275
180	1.7926	27	- 1	- 1	0.0001	14.4642	31.1031

The first column at the left of the table indicates the cycle or iteration number that the computer produced in the process of converging toward the optimum solution. The second column indicates the fuel used in performing this translation of the point mass, which is the object of the minimization process. The sixth column, the gradient, is the most important figure of merit. It tends to zero as the minimum fuel point is reached. This variable, the gradient, is somewhat analogous to the concept of the slope of a curve, which approaches zero as the curve approaches its minimum value. The value of the gradient and the numerical values of the preceding three columns are used as criteria in order to judge how "close" to the optimum solution one has come. How long it takes to reach this condition is a factor that depends on the initial choice of a thrust profile. This in turn depends largely on intuition and a physical understanding of the problem. As problems increase in complexity, and a physical reasoning of the problem becomes more difficult, it is of considerable advantage to have available a method that is insensitive to the initial guess of the control vector. The method of steepest descent also has this desirable property, as was illustrated by the convergence process described in the preceding paragraphs.

Military Applications

Interception of Orbiting Satellites: Problems of short-term prediction of the position of orbiting satellites, using the values of the orbital elements obtained from radar tracking, have long been under study. The difficulties present in these problems arise from the fact that the position and velocity of the satellite in its orbit can only be estimated, with a certain degree of confidence, from the radar data that one uses to calculate the orbital elements.

The problem of intercepting an orbiting satellite whose position and velocity are known only approximately, but with known statistical distribution, may be formulated as the problem of finding the optimum intercept trajectory that maximizes the kill probability. This problem is under study by the Analysis Section of Headquarters, Army Air Defense Command. It appears that the extension of the method of steepest descent is applicable to this problem. Discussions are underway with their personnel in order to identify the elements of this complex problem that could serve as parameters in the optimization scheme.

Tactical Air-to-Air Interceptor Study: In a particular study of tactical air-to-air interception, aerial battles between fighter aircraft are to be considered. From the point of view of the attacker, the aim is to seek a pursuit trajectory that maximizes his chance of hitting his target. On the other hand the target attempts to minimize its chances of being hit, and seeks optimum evasion trajectories. Although this subject falls into the purview of the vast field called differential games, the immediate aim of this study has less ambitious goals. Consequently the

resulting, simplified problem of finding optimum pursuit or evasion
trajectories (in the presence of various inequality constraints on the
turning rates, climb rates, etc.) can be solved using the successive
approximation scheme discussed in this paper. Discussions are underway
with personnel of the Directorate of Synthesis, Systems Engineering
Group, Wright-Patterson AFB, on the applicability of this method. That
directorate has been requested by Headquarters, USAF to conduc_ a
"Tactical Air-to-Air Interceptor Study" as discussed above.

Interplanetary Return Flights: The problem of returning from an
interplanetary flight and landing at a predetermined position on the
earth poses some crucial problems. Perhaps one of the major dilemmas
is that involved in the combined use of retro-rocket braking outside of
the atmosphere, and the use of drag and lift with an ablative shield
within the atmosphere. The retro-rocket firing outside the atmosphere
permits the reduction of the supercircular return velocity to a more
tolerable level for entry into the atmosphere but at the expense of
consuming a considerable amount of fuel. On the other hand, the sole
use of an ablative heat shield could, in connection with the use of
lifting surfaces, serve to effect the desired recovery and landing of
the interplanetary probe.

Either of the two techniques, however, will involve the loss of
mass, either as fuel expended or as material ablated. Thus one would
want to study the optimum mix of rocket braking and atmospheric
deceleration and the time when one ought to change from retro-thrusting
to a coasting period, if any, and the switch to using lifting surfaces
and a heat shield. As part of this optimization study one must consider
the various portions of the return and consequently treat the times at
which the behavior of the system changes as additional parameters to be
chosen optimally. Thus the extension to the method of steepest descent
as described herein is applicable to this problem. A joint study on
this problem with personnel of the von Karman Institute for Fluid
Dynamics, Brussels, Belgium, has been underway since the early summer
of 1965.

Athena Booster: A multi-stage missile of interest to the Air Force is
the Athena booster. The Athena is a four-stage solid propellant booster
with attitude control system that is launched from Green River, Utah,
and whose payload impacts at the White Sands Missile Range. Its purpose
is to deliver test payloads at typical missile re-entry conditions. The
first two stages are fired during ascent; during this period a combin-
ation of spin stabilization and fixed aerodynamic fins stabilize the
missile. The third and fourth stages are spin-stabilized and the third
stage is fired upon command from a ground-based radar at White Sands
Missile Range. The fourth stage fires a fixed time after burnout of the
third stage.

The problem of optimizing the flight path of a multi-stage vehicle
such as the Athena, involves selecting the best times at which to

initiate and terminate the coasting periods, as well as finding the optimum thrust angle for each stage. Even within the restriction imposed by the construction and design of this vehicle and its guidance and stabilization schemes, a number of parameters could be selected optimally in order to achieve maximum payload velocity or a maximum payload capability. The application of the method discussed in this paper to optimize the flight path of the Athena booster has been discussed with a representative of the Aerospace Corporation; the purpose of this discussion has been to identify possible and profitable areas of application of the present method.

Conclusions

The preceding discussion has presented an extension of the method of steepest descent which makes this technique applicable to a more general class of problems. This class of problems is characterized by the presence of inequality constraints on the control variables; these arise from the physical limitations that are present in a realistic environment.

The example used to illustrate the application of this method shows that the method gives rise to a sequence of approximations that converges to the optimum solution, even when the initial control function differs drastically from the optimum control. This is a most desirable characteristic, especially for complicated problems, for which one cannot readily deduce the shape of the optimum control, and is forced to assume some arbitrary function to initiate the convergence process.

The four applications of this method given in this paper represent the wide variety of physical situations that can be represented mathematically in analogous forms; for all of these problems the present method offers an automatic computer technique that calculates their solutions.

References

1. Bryson, A.E. and Denham, W.F., "A Steepest Ascent Method for Solving Optimum Programming Problems", Journal of Applied Mechanics, TASME, Series E, 29:247-257 (June 1962).

2. Vachino, R.F., "Steepest Descent with Inequality Constraints on the Control Variables", SIAM Journal on Control, 4 (1966) To appear.

Dr. E. R. van Driest, an AFOSR contractor, is Chief Scientist of the Ocean Systems Department of North American Aviation. During the past 10 years, under AFOSR contract, he has published over 20 papers in aerodynamics and has made significant contributions to boundary-layer, heat-transfer and drag research for high-speed re-entry of blunt bodies. As Director of North American Aviation Aero-Space Laboratories, forerunner of the Space Sciences Laboratory, he was responsible for basic research in the design of space systems. Dr. van Driest is a graduate of the Case Institute of Technology and holds a Ph. D. in Civil Engineering from the California Institute of Technology. He has been a member of the faculties of the University of Connecticut and the Massachusetts Institute of Technology.

BOUNDARY LAYER STUDIES—PRACTICAL IMPLICATIONS

by E. R. van Driest
North American Aviation, Inc.

ABSTRACT

Research into viscous flow phenomena at North American Aviation, Inc., has provided deeper insight into the mechanism and control of transition from laminar to turbulent flow. Relationships have been derived that give the size of finite roughness elements required to generate a fully turbulent flow depending on Mach number and heating rate and that indicate the effect of intensity of freestream turbulence and amount of pressure gradient on transition. How this control of boundary layer transition can influence the design of high-lift STOL aircraft as well as hypersonic reentry vehicles is discussed.

INTRODUCTION AND STATUS QUO

When a solid body moves through a fluid, such as air, some of the fluid is dragged along by the surface of the body to produce what is called the boundary layer. It is within this boundary layer that the velocity changes sharply from the speed of the body to the fluid medium and thereby produces the shearing friction drag on the body as well as the friction heat transfer to the body. The boundary layer on a 10° cone in supersonic flow is shown by shadowgraph in Figure 1. Because of the thinness of the layer, observation of its growth in such a photograph is practically impossible; therefore, the technique of distorting the field normal to the flow as shown by the schlieren photographs of Figure 2 has been developed.

Transition

It is appropriate at this point to introduce the phenomenon of transition. The sudden change in thickness of the boundary layer along the flow indicates that the initial laminar viscous layer has become turbulent with ensuing vertical spread of turbulent eddies. This change over from laminar to turbulent flow is a result of instability of the basic laminar shearing motion at sufficiently high inertial forces

Re$_\delta$/INCH = 0.5X10^6

Re$_\delta$/INCH = 0.4X10^6

Figure 1. Shadowgraph of Boundary Layer on a 10° Cone at Local
Mach Number of 3.67

relative to viscous restraint, the ratio being called the Reynolds number. Concern for turbulent flow on the part of aircraft designers stems from the fact that inherent in the turbulent boundary layer is an increase of skin friction as well as heat transfer. Even the heat of friction available for transfer is greater, as seen in the insulated wall temperature graphs of Figure 2. It is also noted that the position of transition as indicated by the sudden thickening of the layer and its corresponding rise in temperature moves downstream with decreasing Reynolds number per unit length, signifying that the Reynolds number of transition for this condition of flow over a smooth body is roughly constant.

The direct phenomenon of transition is, then, of immediate importance to the calculation of the performance of such bodies as smooth, high-speed reentry cones owing to the relative drags of laminar versus turbulent flow. Calculation of the heat transfer is even more significant. However, the position of transition is not known for such high speeds and heat transfer rates, let alone more understanding of the heat transfer itself with turbulent flow. Of course these problems would be minimized if turbulent flow could be eliminated by some process such as suitable shaping of the body, suction, sufficient cooling, or even by some turbulence suppressor in the form of long-chain polymers.

Separation

Another important phenomenon that affects the lift and drag and general performance of low- and high-speed aircraft is separation of the flow from the aircraft or parts of the aircraft. This phenomenon is caused by the direct interaction of the boundary layer with an external pressure field, particularly an increasing pressure or adverse pressure gradient against which the flow must move. It is a well-known fact that the slower moving fluid in the boundary layer cannot negotiate a sufficiently strong pressure gradient and, therefore. must flow away (i. e., separate) from the surface. As mentioned above, separation especially imposes limits on aircraft performance capability. At low speed during take-off and landing, it can limit the amount of lift capability because of stalling and loss of control effectiveness. At high speed, it can limit the maximum subsonic speed relative to the velocity of sound (Mach number) because of compressibility effects on drag and control effectiveness and can limit the supersonic lift-drag ratio capability by limiting the amount of favorable wing twist and camber possible.
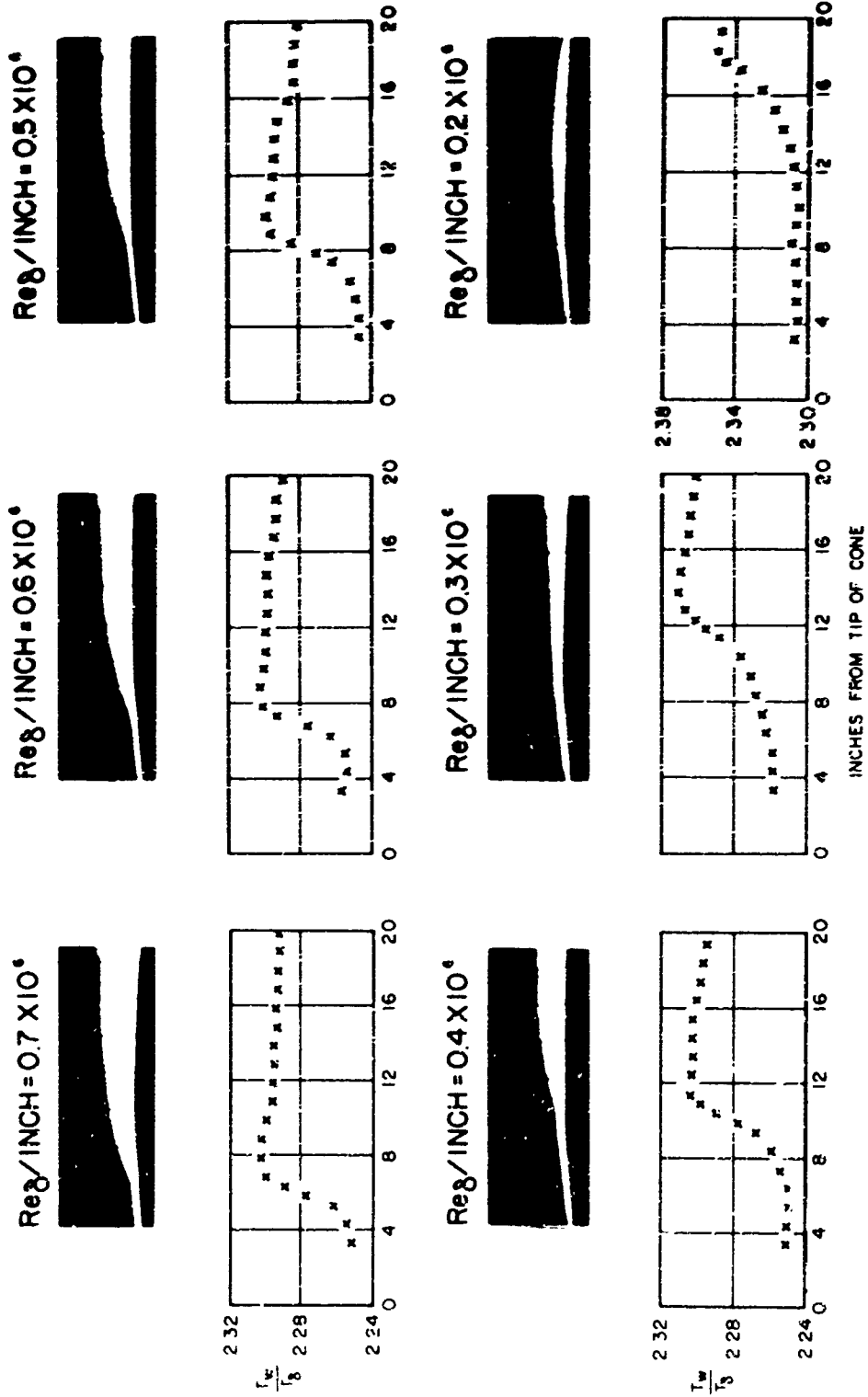
14

Figure 2. Magnified Schlieren Pictures and Temperature
Distributions for a Boundary Layer on a Smooth 10°
Cone at Local Mach Number of 2.71

Shape control

Transition and separation are related, however, in that adverse pressure gradients may induce them and, conversely, in that falling (favorable) pressure gradients retard them. The former effect is an unwelcome parasite which often results from attempts to obtain high lift or low drag. The latter effect can be taken advantage of by properly shaping a body or wing section to produce a long run of falling pressure, thereby delaying transition and separation. But, as is readily seen, a falling pressure is always associated with a rising pressure to get back to freestream conditions; therefore, judicious design must be carried out to minimize the effects of adverse pressure gradient. An example of airfoil section design for purposes of delaying transition to the point of just preventing separation is the 66 Series NACA profile. These airfoils are however very sensitive to roughness but do increase the subsonic Mach number at which drag due to separation from local shock waves begins to rise drastically.

Vortex generators

Since separation is caused by an adverse pressure gradient acting on the slower moving fluid in the boundary layer, it follows that a turbulent boundary layer with its higher-speed air nearer the surface should separate later. This is indeed true; therefore, either the boundary layer before laminar separation may be artifically made turbulent by simple roughness elements or even larger elements, called vortex generators, may be installed to reach well into the flow and bring higher-energy air nearer to the surface to delay separation. The latter, more efficient method is used on the inboard upper surface of the wing of the Boeing 707 to induce flow attachment over the inboard ailerons for better control effectiveness during take-off and landing and during cruise when local shocklets appear over the wings and promote separation. Vortex generators are also being used in supersonic inlets to jet engines and on tail surfaces of fighter aircraft wherever the boundary layer may separate because of local shocks.

Bleed (suction) control at inlets

The efficiency with which a high-speed induction inlet system performs can be improved through the utilization of boundary layer bleed. The removal of low-energy air from the boundary layer not only provides a higher total pressure recovery at the engine face but also acts to stabilize the terminal shock. Furthermore, the adverse

16

effects of shock-induced boundary layer separation on inlet control
pressure signals are avoided. Finally, the stability range (i. e., range
of operation without mass flow resonance) is increased. Thus, the
overall efficiency of a high-speed induction system is improved. Of
course, the air removal is routed overboard and exhausted through
ducting in a manner to provide additional thrust to the air vehicle as
well as to provide forced blowing over flaps to gain lift through pre-
vention of separation. This total system has been applied to the
XB-70A vehicles with flight test results indicating very high inlet
performance.

STOL aircraft

STOL aircraft, such as the COIN concept intended for use in
Viet Nam, make considerable use of knowledge of boundary layers and
its control. High lift for take-off and landing is required with its
associated requirement for adequate control at high lift and low air-
speed. This means extensive use of leading edge slats and trailing
edge flaps with natural or forced blowing through the slots and over
the airfoil as well as blowing through and over the flaps to control
separation and thereby gain the required high lift. The additional use
of spoilers to destroy lift and descent quickly without stalling the entire
wing section and for air brakes along with adequate use of vortex
generators are expected.

Summary remarks

The presence of viscosity, as manifest by the boundary layer,
is a detriment and a benefactor as well. In supersonic flight, it is
mainly a detriment because lift is derived mainly from shock com-
pression and the boundary layer is the source of drag and heat transfer
as with high-speed reentry vehicles. On the other hand, in subsonic
flight the presence of viscosity is a benefactor because from it is
derived all lift through the concept of circulation. Therefore, the
problem of attainment of high lift at low speeds reduces to the problem
of generation of high circulation which requires delayed separation
until the very end of the aircraft wing tip or flap, through whatever
method is available.

RESEARCH ON ROUGHNESS EFFECTS

In the above paragraphs, it has been discussed how turbulent
boundary layers are mostly detrimental yet can be used to advantage

in aircraft design. Therefore, the artificial control of turbulent layers, that is, the artificial control of transition, is a desirable tool of the aerodynamicist. Since it was expected that the size of such roughness would be affected by compressibility and strong heating rates, it was desired to know that dependence for practical missile and aircraft design. An effective method of control, as seen above, is by use of solid elements protruding into the flow. These elements, called roughness elements in this discussion, must be of sufficient size and placed at a proper position along the flow to induce transition and thenceforth provide a turbulent boundary layer. Therefore, under contract with the AFOSR, roughness studies have been conducted in recent years in the 12-inch supersonic wind tunnel of the Jet Propulsion Laboratory at the California Institute of Technology to determine the size of single roughness elements (spheres) required to bring about transition on a smooth, 20-inch, 10° cone with supersonic flow but without heat transfer to or from the boundary layer. Thus, in these experiments, only the speed effect was studied. The means of measurement of transition is illustrated in Figure 2.

Results of the experiments are shown in Figure 3, using data from References 1 and 2 for local Mach numbers M_δ of 1.90, 2.71, and 3.67. The horizontal scale for Reynolds number Re_k is proportional to the minimum size of roughness k and the vertical scale for Reynolds number Re_{x_k} is proportional to the position x_k of the roughness from the tip of the cone. From these data the following numerical formula was found:

$$Re_k = 32.8 \left(1 + \frac{\gamma - 1}{2} M_\delta^2\right) Re_{x_k}^{1/4} \qquad (1)$$

For flat plates the constant must be changed to 43.2.

While this formula is appropriate for supersonic speeds with no heat transfer into or out of the aircraft structure, it is not applicable to conditions with high heat transfer rates, such as during flights of the X-15 or reentry of hypersonic vehicles. Therefore, further experiments were carried out with a cooled model—this time a 42-inch, 10° cone in the 20-inch JPL supersonic wind tunnel. The data are plotted in Figure 4 as a function of temperature ratio T_w/T_δ across the boundary layer, the decrease of which from adiabatic (zero heat transfer) condition represents cooling of the boundary layer or heat

transfer into the cone. These tests were performed at Mach number 2.71. From the data, a new formula for minimum trip size including heat transfer was obtained (Reference 3).

$$Re_k = 33.4 \left[(1 + \frac{\gamma-1}{2} M_\delta^2) - 0.81 (\frac{T_{aw}}{T_\delta} - \frac{T_w}{T_\delta}) \right] Re_{x_k}^{1/4} \qquad (2)$$

where the constant of Equation 1 has been slightly adjusted to include the data of Figure 4 and T_{aw} is the recovery temperature, which is a measure of the temperature rise due to internal friction in the boundary layer. Although this latter formula is reliable for moderate super-sonic speeds and heat transfer rates, it is expected to predict reasonably well the size of roughness required to induce transition at hypersonic speeds with large heating rates as in the case of reentry ballistic missiles. One practical use of such knowledge would be in the sole induction of transition for experimental study of heat transfer from turbulent boundary layers at high speeds, high Reynolds numbers, and high heating rates. Of course, such knowledge is useful even at low speeds for wind tunnel testing when the effects of a high Reynolds number are to be simulated with an induced turbulent boundary layer. Before closing this section, it is of practical significance to add that this research on roughness can be used to give an indication of the degree of natural roughness that can be tolerated on an engineering surface before transition sets in.

RESEARCH ON FREESTREAM TURBULENCE AND PRESSURE GRADIENT EFFECTS

While it is seen that roughness-induced transition has practical importance in a number of aspects such as turbulent flow simulation and prevention of separation, yet the ever-present freestream turbulence as well as pressure gradient (body shape) are of equal significance in the control of transition. Again under contract with the AFOSR, the writer studied the effect of external pressure fluctuations associated with freestream velocity fluctuations on the velocity profile of the laminar flow and found the following relation between freestream turbulence u'/u_δ (root-mean-square velocity fluctuation divided by the average flow outside the boundary layer) and the Reynolds number Re_x of a flat plate (proportional to the distance to transition) such that the local laminar flow breaks down to turbulence:
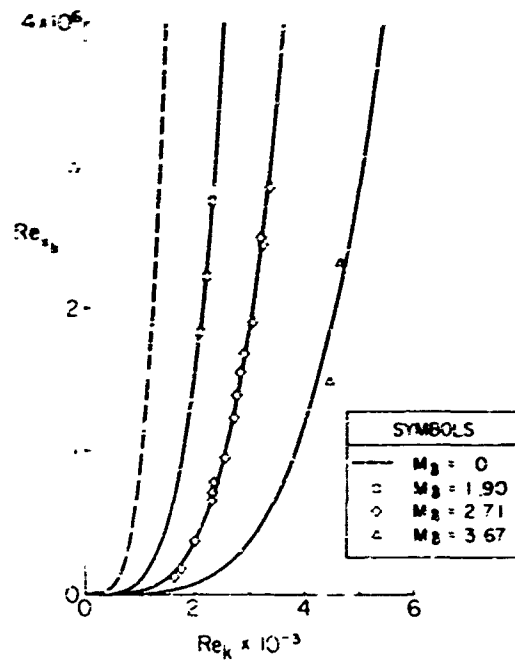
Figure 3. Effective Trip Size Reynolds Number on a Cone Versus
the Trip Position Reynolds Number for Various Mach
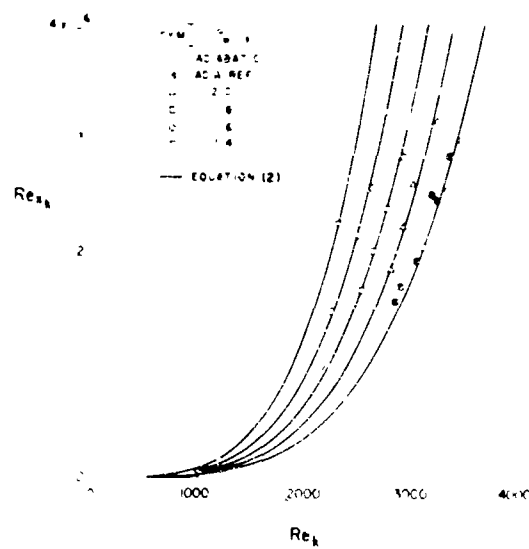Numbers Without Heat Transfer

Figure 4. Effect of Heat Transfer (Cooling) on Roughness-Induced
Transition on a Cone at Local Mach Number of 2.71

$$\frac{1690}{Re_x^{1/2}} = 1 + 19.6 \, Re_x^{1/2} \left(\frac{u'}{u_\delta}\right)^2 \tag{3}$$

This relationship is plotted in Figure 5 and seems to fit the available data fairly well. The practical implication of this analysis is that it not only gives a numerical value for the position of transition in terms of freestream turbulence but also verifies the underlying notion of the vorticity (shear) layer used in its derivation (Reference 4).

The concept of shear layer Reynolds number basic to Equation 3 also allows the pressure gradient dp/dx to be included in the transition relationship. Thus the following expression may be derived:

$$\frac{9860}{Re_\delta} = 1 - 0.0485 \, \Lambda + 3.36 \, Re_\delta \left(\frac{u'}{u_\delta}\right)^2 \tag{4}$$

where Λ is the Pohlhausen parameter proportional to the pressure gradient and Re_δ is the Reynolds number in terms of the local thickness δ is the boundary layer.

Equation 4 is a very useful relation because with it, one can determine the position of transition on a given body at a given speed and, furthermore, even shape a body for best performance, i.e., least drag.

A recent application of this combined theory of freestream turbulence and pressure gradient to the calculation of transition on an underwater torpedo shape is of interest. The torpedo is the Dolphin whose shape is obtained by revolving a laminar flow airfoil (66 series) about its chord. The configuration and corresponding pressure distribution is shown in Figure 6. The body, designed by the Ocean Systems Division of North American Aviation, Inc., was drop-tested to a depth of some 800 feet in the Pacific Ocean off Catalina Island to determine its performance characteristics. A hydrophone was mounted on the surface of the body at 50-percent chord so internal recording equipment could detect the first bursts of turbulence. In order to compare such data with the above theory, calculations of the transition Reynolds number Re_s in terms of distance s from the nose of the body were carried out and plotted in Figure 7 as a function of chord station for various freestream turbulence levels. Also plotted in Figure 7 is the computed time for transition bursts to first appear in terms of station during the drop-test trajectory. A playback of the record gave a time
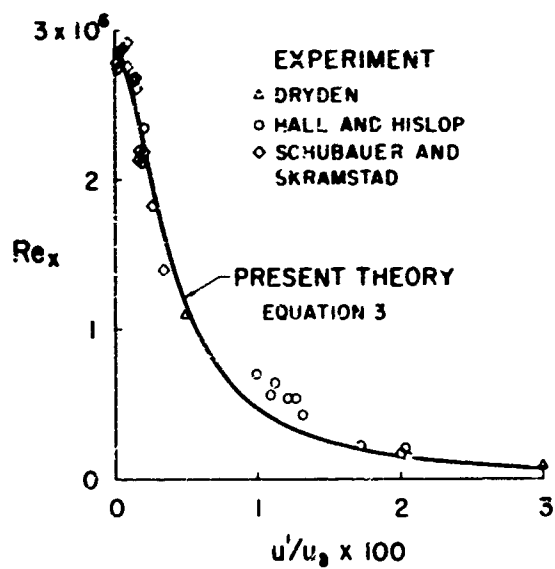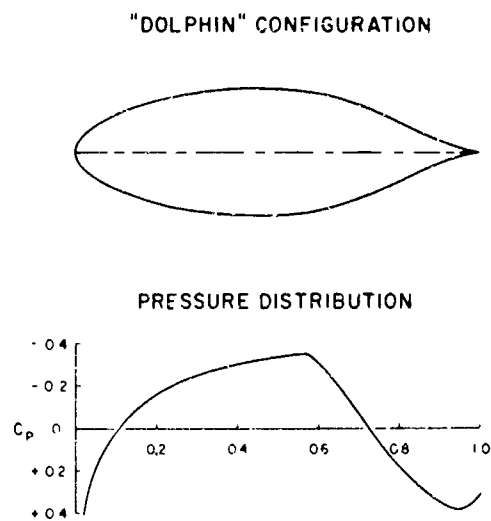
Figure 5. Effect of Freestream Turbulence on Transition

Figure 6. Configuration and Pressure Distribution of Dolphin Body

of 3. 5 seconds until the first bursts appeared, which substantiated the theory in Figure 7.

The above research on freestream turbulence and pressure gradient effects had to do with low-speed aerodynamics. Extension to high-speed flow with heat transfer is essential, particularly for application to hypersonic reentry vehicles.

RESEARCH ON NON-NEWTONIAN ADDITIVES

An exceedingly intriguing means of turbulence control is the possible use of long-chain polymers or turbulence suppressors. Owing to current interest in the phenomenon of drag reduction as a result of addition of such polymers to flowing water, attention was given under the present AFOSR contract to the stability of non-newtonian fluid flow because it was felt that these polymers were non-newtonian and that stabilization of the fluid by the additives was the cause of such drag reduction.

The simplest mathematical form for shear τ of a non-newtonian fluid was assumed, viz., the Bingham liquid:

$$\tau = \tau_y + \mu \frac{du}{dy} \tag{5}$$

where τ_y is the yield stress to be overcome by initial relative motion du/dy. Using the Kármán momentum integral, one obtains the following relationship for thickness of a laminar boundary layer on a flat plate, viz.,

$$Re_x = \frac{0.882}{c_y^2} \left[\frac{c_y Re_\delta}{3.45} - \ell n \left(1 + \frac{c_y Re_\delta}{3.45} \right) \right] \tag{6}$$

in which c_y is the yield stress coefficient. Having this expression and the shear layer Reynolds number

$$\frac{\rho y^2 \left(\dfrac{du}{dy} \right)^2}{\tau_y + \mu \cdot \dfrac{du}{dy}} = 2465 \tag{7}$$
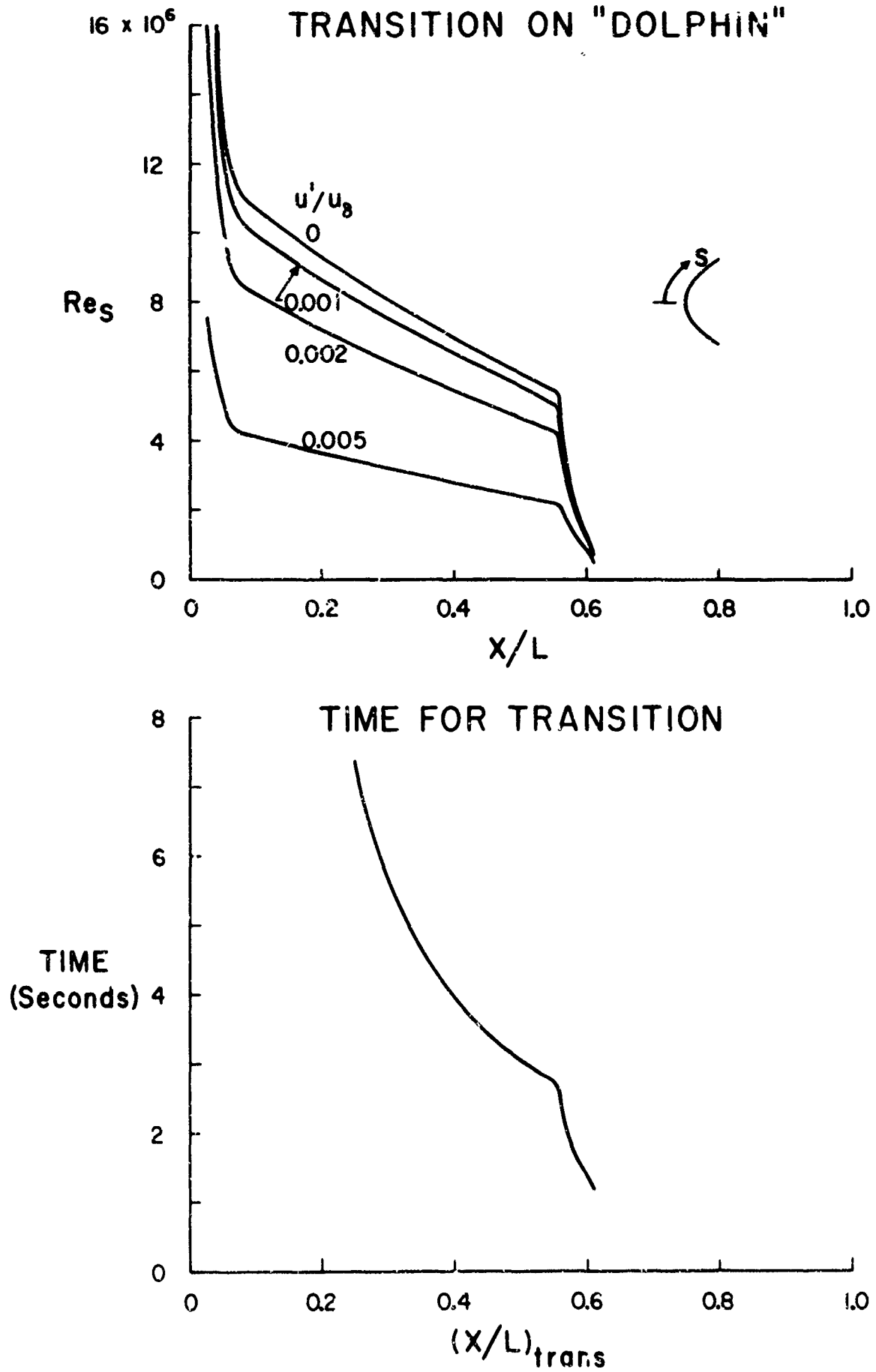
Figure 7. Transition Reynolds Number Versus Chord Station and
Time for Transition to Occur During Drop Test for Dolphin

as a criterion for transition from laminar to turbulent flow, the interesting result was obtained that the transition Reynolds number Re_{x_T} proportional to distance x_T to transition increased rapidly with yield stress coefficient c_y and, in fact, became infinite at the small value $c_y = 0.00025$. This variation is shown in Figure 8, verifying fully the prediction that non-newtonianism of the type in Equation 5 can lead to stability and, therefore, decrease in total drag owing to delay of boundary layer transition.

Calculations of friction for laminary boundary layers on flat plates with pseudoplastic (Equation 5) as well as with dilatant type of Bingham fluid,

$$\tau = -\tau_c + \mu \frac{du}{dy} \tag{8}$$

are of practical interest and are plotted in Figure 9. Note that the stress τ_c in Equation 8 represents a repellant stress within the fluid. Of special attention is the possibility of attaining drags in laminar flow less than for ordinary newtonian fluids; however, transition will be encouraged which would tend to mitigate the effect.

REFERENCES

1. E. R. van Driest, and C. B. Blumer, "Boundary-Layer Transition at Supersonic Speeds—Three-D mensional Roughness Effects (Spheres)," Journal of the Aerospace Sciences, Vol. 29, No. 8, August 1962.

2. E. R. van Driest, and W. D. McCauley, "The Effect of Controlled Three-Dimensional Roughness on Boundary Layer Transition at Supersonic Speeds," Journal of the Aerospace Sciences, Vol. 27, No. 4, April 1960.

3. E. R. van Driest, and C. B. Blumer, "Summary Report on Studies on Boundary Layer Transition for Years 1963-64," SID 64-2191, North American Aviation, Inc., 1964.

4. E. R. van Driest, and C. B. Blumer, "Boundary Layer Transition: Freestream Turbulence and Pressure Gradient Effects," AIAA Journal, Vol. 1, No. 6, June 1963.

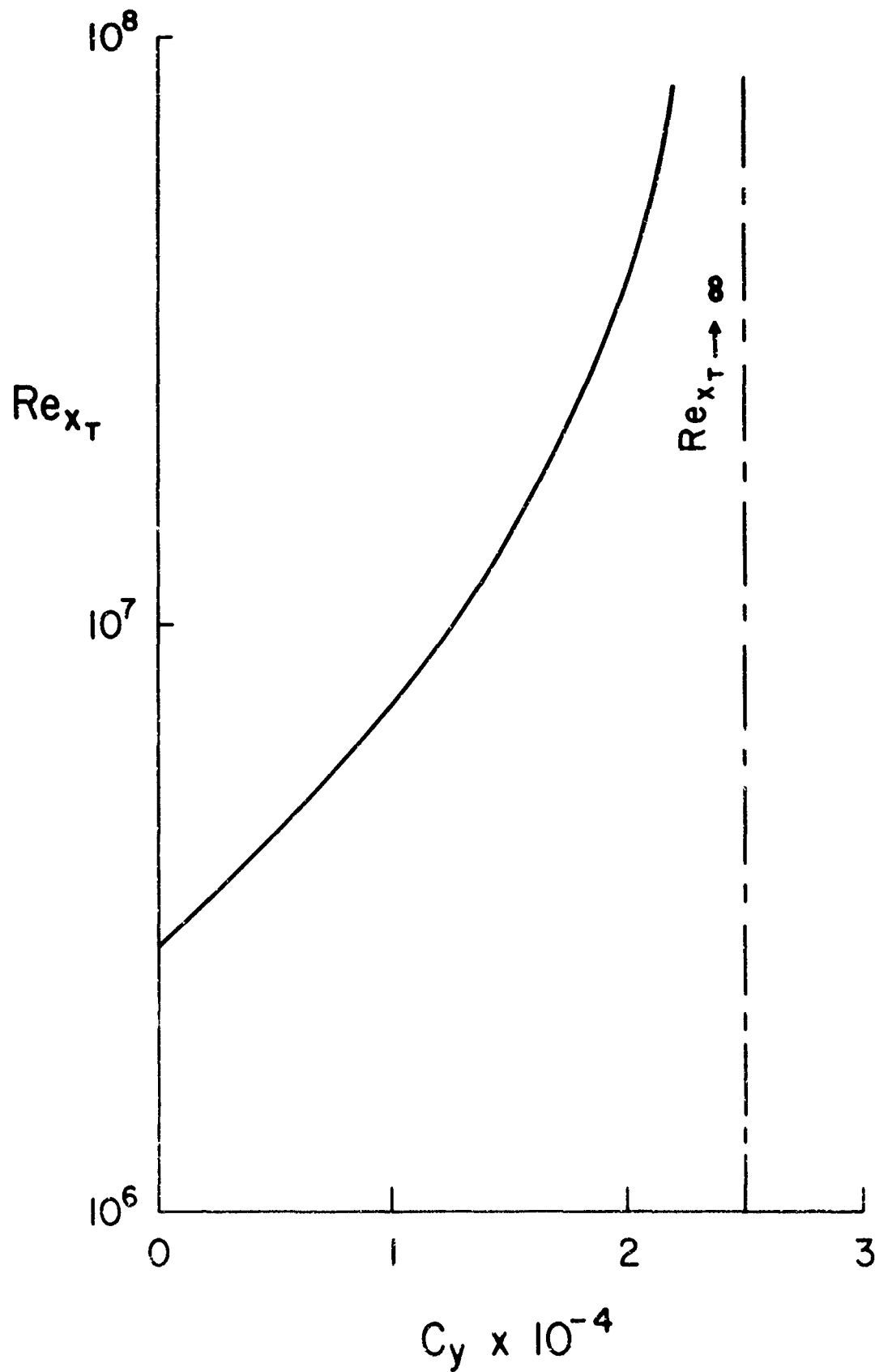# TRANSITION AS A FUNCTION OF THE YIELD STRESS COEFFICIENT

Figure 8. Transition as a Function of the Yield Stress Coefficient for a Flat Plate

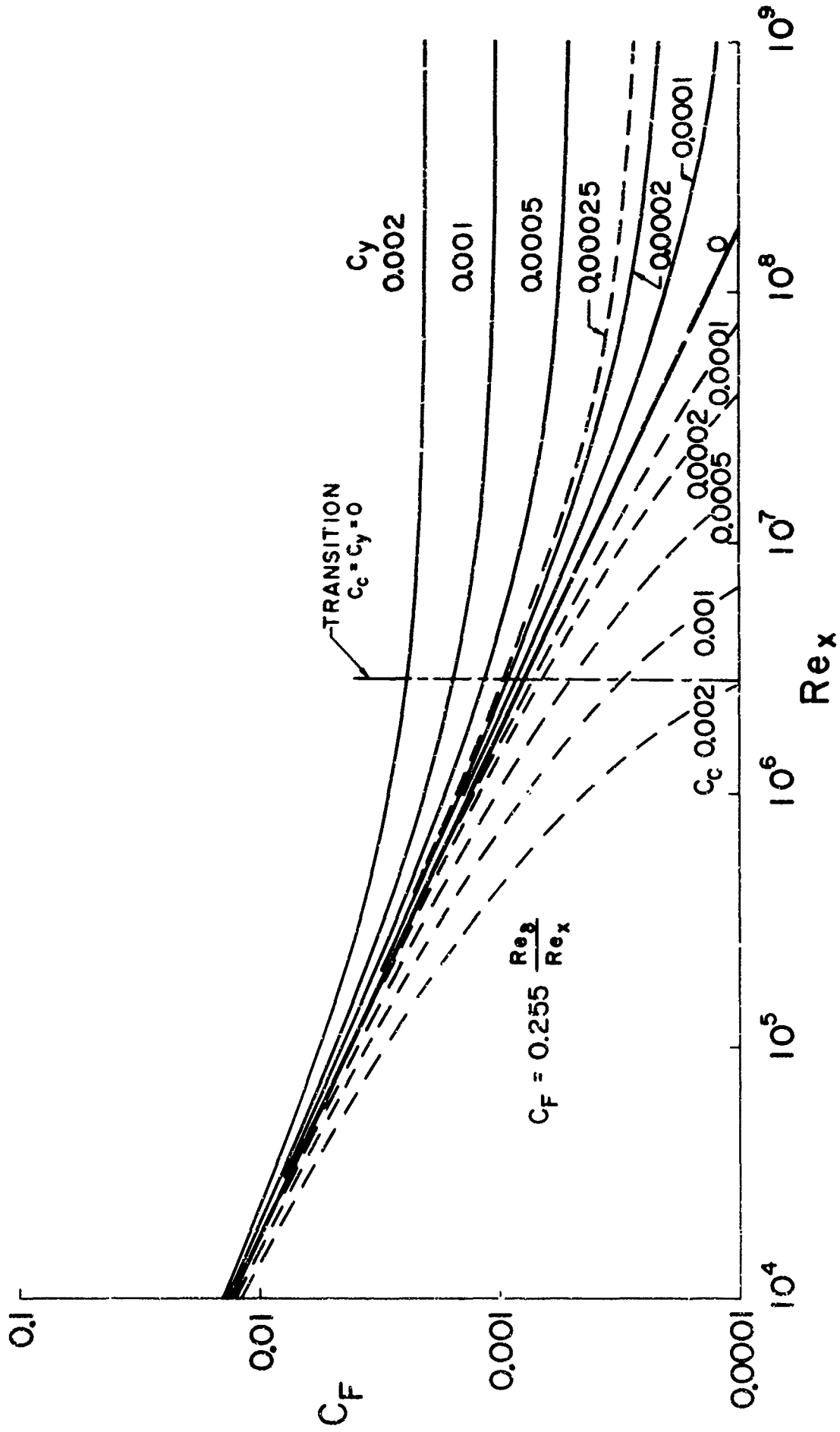MEAN FRICTION COEFFICIENT FOR LAMINAR FLOW ON A FLAT PLATE
(BINGHAM LIQUID)

Figure 9.   Average Friction Coefficient for Laminar Flow on a Flat
Plate for a Bingham Liquid

NOMENCLATURE

k	roughness element height
x_k	distance along surface to roughness element, measured from beginning of boundary layer
s	distance along surface, measured from stagnation point
x_T	distance to transition, measured from beginning of boundary layer
u	velocity
y	distance normal to surface, measure from surface
x	distance along surface, measured from beginning of boundary layer
u'	root-mean-square velocity fluctuation
u_δ	velocity at outer edge of boundary layer
ρ	fluid density
ρ_δ	fluid density at outer edge of boundary layer
μ	fluid viscosity
μ_δ	fluid viscosity at outer edge of boundary layer
λ	ratio of specific heats
p	pressure
τ	fluid shear stress
τ_w	shear stress at wall
τ_y	yield stress
τ_c	repellant stress

28

c_y yield stress coefficient,

c_c repellant stress coefficient,

δ boundary layer thickness

M_δ Mach number at outer edge of boundary layer

T_w temperature at wall

T_δ temperature at outer edge of boundary layer

Λ Pohlhausen parameter $(-\delta^2/\mu u_\delta)\, dp/dx$

C_F average friction coefficient, $2 \int_0^x \tau_w\, dx/\rho u_\delta^2$

X distance along chord of body from nose

L chord length

T_{aw} recovery (adiabatic) wall temperature

Re_k Reynolds number of trip, $\rho_\delta u_\delta k/\mu_\delta$

Re_x Reynolds number of distance x, $\rho_\delta u_\delta x/\mu_\delta$,

Re_{x_T} Reynolds number of distance to transition, $\rho_\delta u_\delta x_T/\mu_\delta$

Re_s Reynolds number of distance s, $\rho_\delta u_\delta s/\mu_\delta$

Re_{x_k} Reynolds number of trip position x_k, $\rho_\delta u_\delta x_k/\mu_\delta$

Re_δ Reynolds number of boundary layer thickness, $\rho_\delta u_\delta \delta/\mu_\delta$

First Lieutenant John W. Steurer is assigned to the Fluid Dynamic Facilities Research Branch, Aerospace Research Laboratories. Lt. Steurer holds a B.S. and M.S. in Aeronautical Engineering from the University of Notre Dame. In 1961, he received a doctoral assistantship at the University of Arizona, where he completed his course work toward a Ph. D. in Aerospace Engineering. He expects to finish his dissertation while at ARL. Lt. Steurer is an associate member of Sigma Xi, and recently was accepted for full membership in the AIAA.

SUPERSONIC COMPRESSOR RESEARCH

JOHN W. STEURER
1st Lt, USAF
Fluid Dynamics Facilities Laboratory
Aerospace Research Laboratories
Office of Aerospace Research
Wright-Patterson Air Force Base, Ohio

ABSTRACT

Supersonic compressors offer the advantages of lightness of weight, compactness, and simplicity of design due to high pressure ratios per stage and high inlet Mach numbers.

This paper describes: (1) a new concept of supersonic compressor blading developed at ARL, (2) a mathematical model of the flow process developed at ARL for performance prediction and optimization purposes, (c) a description of and some preliminary results of the experimental program currently underway.

I. INTRODUCTION

The increasing importance attached to air breathing flying vehicles capable of supersonic cruise has caused a strong resurgence of interest in the development of advanced air breathing engines. Such engines usually consist, at least in part, of a turbojet or turbofan. One of the most critical components of the turbojet or turbofan engine is the axial compressor which precedes the combustion zone of the power plant. This compressor must compress efficiently with minimum dimensions and weight. To be realistic, the weight considered must include that of the inlet diffuser which may amount to a considerable part of the aircraft structure in the case of an efficient supersonic inlet. Similarly, the compression efficiency must include the performance of the inlet diffuser in order to be meaningful.

One of the main disadvantages of the axial flow compressor is its relatively low pressure ratio per stage. Therefore, to achieve an overall high pressure ratio some axial flow compressors are built with as many as 17 stages. A compressor with a large number of stages is expensive, difficult to build, excessively long, suffers a weight penalty, and poses a serious logistics problem.

Supersonic compressors have two very attractive features: (1) a high pressure ratio per stage, and (2) the ability to accept high inlet Mach numbers. A high pressure ratio per stage reduces the number of stages needed to fulfill an overall engine requirement and, therefore, reduces the engine's cost, complexity, size, and weight. The ability to accept high inlet Mach numbers simplifies the inlet diffuser problem.

Technically, the supersonic compressor has been considered to be any compressor stage utilizing supersonic flow over the entire blade span. Typical of this type are compressors having relative inlet Mach numbers in the range of 1.5 to 2.0 and total pressure ratios on the order of 3.0 to 5.0. Currently, high performance transonic compressors operate at relative inlet Mach numbers between 1.0 and 1.5 and total pressure ratios on the order of 2.0.

The increased performance of the supersonic compressor is not achieved without some sacrifice in efficiency. Whereas transonic compressors operate with an isentropic efficiency between 85-90 percent, a comparable efficiency of about 80 percent is predicted for supersonic compressor operation. A generalized comparison of compressor performance is shown in Figure 1.

The research program on supersonic axial compressors at the Aerospace Research Laboratories is focused on the investigation of a particular blade design philosophy. This is the concept of the blunt-trailing-edge design, an idea which was conceived at ARL and first reported in 1959 (Reference 1).

II. THE BLUNT-TRAILING-EDGE BLADE DESIGN

The blunt-trailing-edge concept is that type of blading which can accept supersonic flow entering the blade row over the full span. The passage has essentially constant area between adjacent blades. An example of the geometry is shown in Figure 2. This configuration was chosen primarily for two reasons. First, with conventional

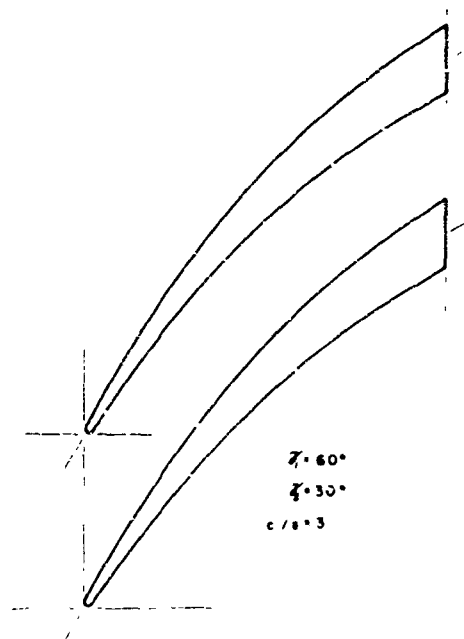| Perf-rmance Parameter	Type of Compressor		
	Subsonic	Transonic	Supersonic
Total Pressure Ratio per Stage	1 2	1 2 - 2 0	3 0 - 5 0
Isentropic Efficiency (%)	90 - 94	85 - 90	80
Relative Inlet Mach Number	less than 1 0	1 0 - 1 5	1 5 - 2 0

Figure 1. Compressor Performance Comparison

Figure 2. Circular Arc Supersonic Rotor Blading

blading having relatively sharp trailing edges, supersonic flow nearly always separates from the convex surface so that the effective cross section of healthy flow does not differ greatly from one having constant area. Second, a relatively efficient form of supersonic diffusion known as pseudo-shock diffusion is known to occur in constant area ducts and it was hoped to achieve a similar condition in a rotor. An illustration of this process is shown in Figure 3. The passage wall boundary layers cannot sustain a normal-shock pressure gradient so a pseudo shock formed which is actually a series of small normal shocks with bifurcated ends caused by shock/boundary-layer interaction. The loss in total pressure experienced by the flow passing through this series of shocks is considerably less than would be caused by a single normal shock at the inlet Mach number. However, dissipative forces in the turbulent wall zones cause the overall loss associated with a pseudo-shock condition to be roughly equivalent to a normal shock having the same upstream Mach number. Therefore, the variation of total pressure ratio with upstream Mach number for a normal shock is used in order to approximate the relationship between total pressure loss and Mach number for a pseudo shock. A more elaborate discussion of pseudo-shocks may be found in Reference 2.

The greatest portion of the remaining losses is caused by the sudden enlargement of cross section as the flow departs from the rotor. These losses are at a minimum when the relative outlet Mach number is as low as possible; therefore, it is important to achieve as much diffusion as possible within the rotor.

III. STATOR BLADE DESIGN

Supersonic compressor flows characteristically exhibit a high degree of turning. Absolute outlet angles on the order of 60 degrees are obtained. To realistically evaluate the overall performance, a stator capable of turning the flow back to the axial direction was designed. The stator consists of two rows of double circular arc blades. An illustration is shown in Figure 4. This design was chosen to allow a portion of the high velocity gas flowing along the bottom surface of the first blade to be "injected" on to the upper surface of the second blade. The effect is to delay separation and permit a higher degree of turning.
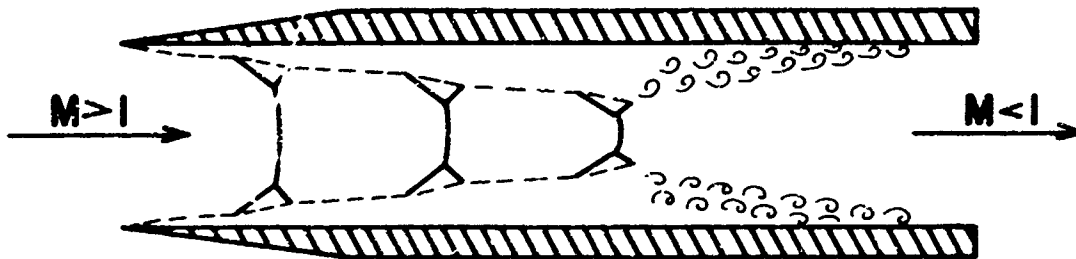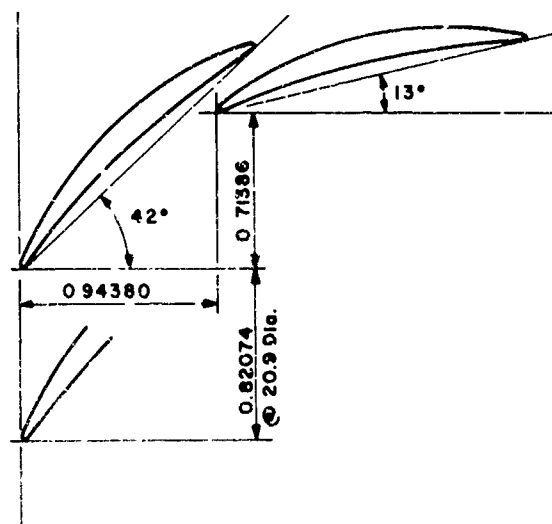
Figure 3. Shock/Boundary-Layer Interaction in Pseudo-Shock Diffusion

Scale — 2 1

Dimensions in Inches

80 Blades Per Row

Constant Cross-Section, Hub to Tip

Figure 4. Compound Stator Blade Orientation

IV. ARL'S RESEARCH PROGRAM

The research program is divided into three coordinated efforts. Within ARL, emphasis has been placed on the understanding of the basic flow phenomena characteristic of blunt-trailing-edge supersonic compressor blading. The natural result of this study is the development of methods of performance prediction and of ideas for detail refinements to the basic blading to improve aerodynamic efficiency. These efforts have provided an input to supporting experiments being conducted at the Arnold Engineering Development Center (AEDC) and at the von Karman Institute for Fluid Dynamics in Belgium (vKIFD).

The experimental facility at AEDC has been set up to test the supersonic rotors and the complete stages developed at ARL. An illustration of the facility is shown in Figure 5. A complete description of the facility is given in Reference 3.

The more modest effort at vKIFD in Belgium includes some experiments with actual blunt-trailing-edge rotors operating in freon. In addition, some cascade studies have been undertaken.

a. Theoretical Program

The aim of this in-house program was to develop a mathematical method of predicting the quasi-three-dimensional performance of a blunt-trailing-edge supersonic rotor. The flow analysis is termed quasi-three-dimensional because tangential blade to blade variations are neglected. In the solution, losses associated with the boundary layer growth on the blades, hub, and casing have been grouped with the losses due to curvature and the pseudo-shock diffusion process

to determine an overall loss coefficient. Losses due to secondary flows (i. e. flow leakage between blade and casing) have been neglected. Losses due to the abrupt area increase downstream of the rotor trailing edge have been considered separately.

Computer solutions for various configurations and flow conditions are now available. Some of these results are presented in Figure 6 to show the design-speed (100% speed) performance of the ARL rotors as a function of trailing-edge thickness to blade spacing ratio. The solid lines refer to the circular arc rotor shown in Figure 2 and the dashed lines to the modified rotor shown in Figure 7. A more detailed description of the theoretical program is given in Reference 4.
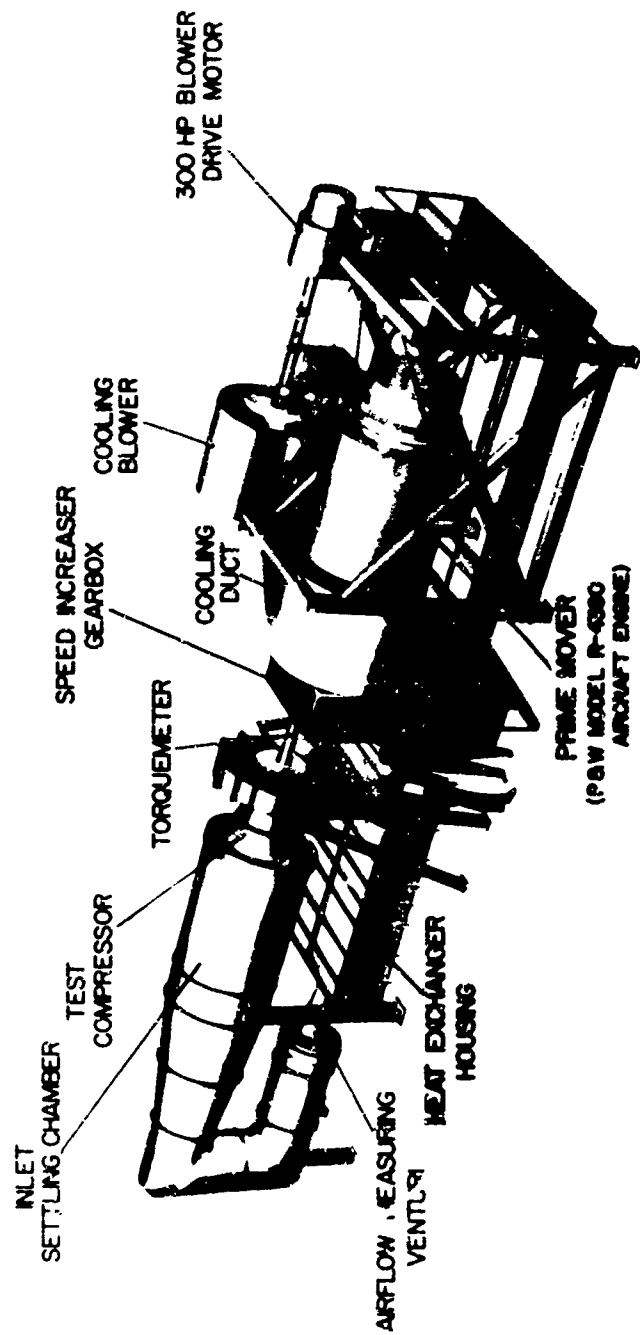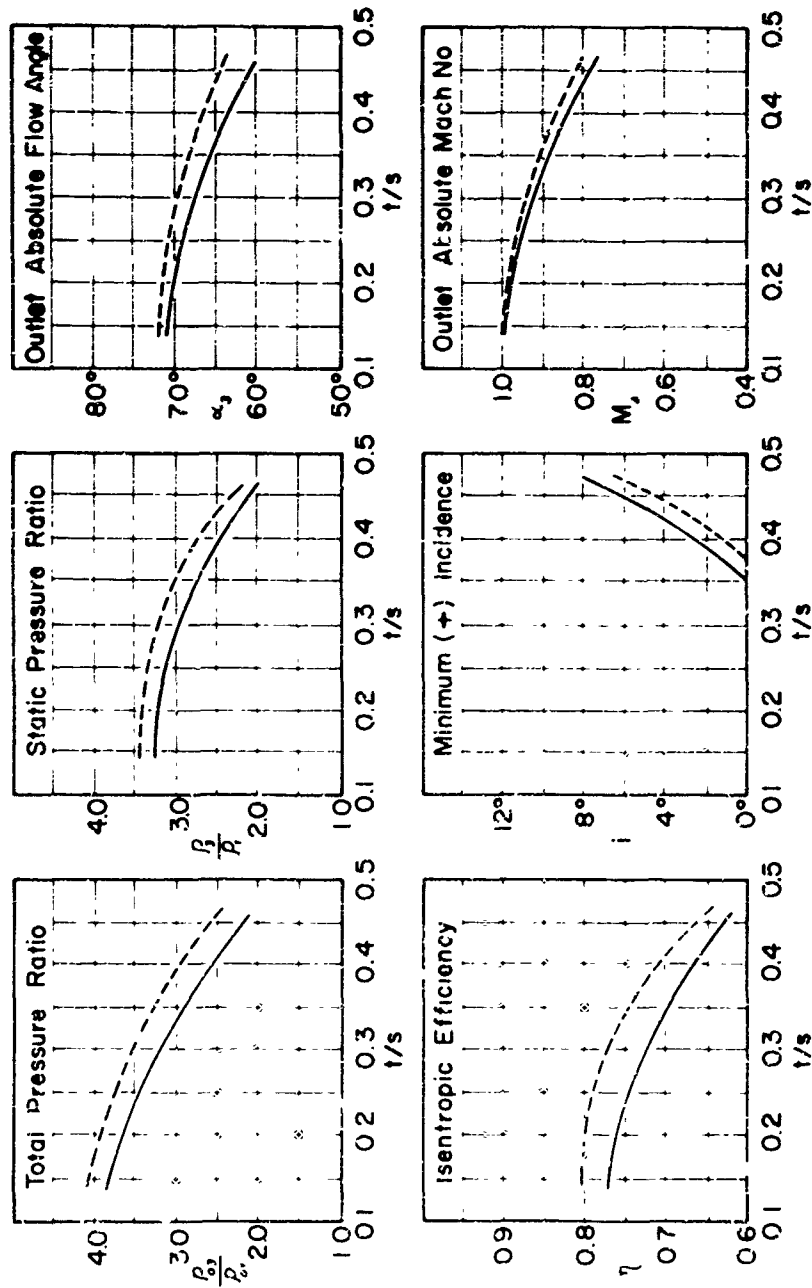
Figure 5. Supersonic Compressor Test Rig

Figure 6. Theoretical Design-Speed Performance for the
ARL Rotors

b.   Experimental Program

Two aerodynamically similar supersonic rotors are currently under test at AEDC. Both rotors have blunt-trailing-edge blading with a chord length to spacing ratio (solidity) of 3. 0, an inlet blade angle of 60 degrees from axial, and an outlet blade angle of 30 degrees from axial. Both rotors have a hub to tip ratio of 0. 9, tip to tip diameter of 22 inches and are intended to operate at a tip-radius relative inlet Mach number of 1. 7.

The first-generation rotor, which was shown in Figure 1, has blade surfaces composed of simple circular arcs. The second-generation rotor, Figure 7, has blade surfaces following a mathematically prescribed curvature distribution. The second-generation rotor is expected to perform more efficiently than the first because the relatively straight inlet portion of the blading will permit the flow to diffuse to a lower Mach number before encountering significant blade curvature. The turning losses should be reduced and the diffusion process in the passage should be more efficient.

Presently, experimental data is available on only two rotor configurations. The first-generation rotor, shown in Figure 8, was recently tested at AEDC. It is of the circular arc design and has a thickness to blade spacing ratio of 0. 395. A second rotor, differing slightly in design from the one tested at AEDC, and with a thickness to blade spacing ratio of 0. 275, hub to tip ratio of 0. 85 and tip to tip diameter of 16 inches, was tested at the von Karman Institute for Fluid Dynamics in Belgium. The performance characteristics of these two rotors are shown in Figures 9 and 10.

Mechanical problems prevented the vKIFD rotor from realizing the design speed. For the maximum speed reached, 92 percent of design speed, a pressure ratio of 2. 9 with an efficiency of 78 percent was obtained. Comparable test conditions for the rotor at AEDC produced a pressure ratio of only 2. 1 with 60 percent efficiency. The better performance of the vKIFD rotor is attributed to the much lower thickness to spacing ratio. The fact that data is not yet available for a rotor operating at the optimum thickness to spacing ratio illustrates the importance of developing an accurate mathematical model. To initiate design and construction of a rotor concurrent with the development of the facility at AEDC, use was made of the then available methods of blade design. These methods were based on the results of two-dimensional cascade studies and on the experience gained during

$\chi_1 \cdot 60°$

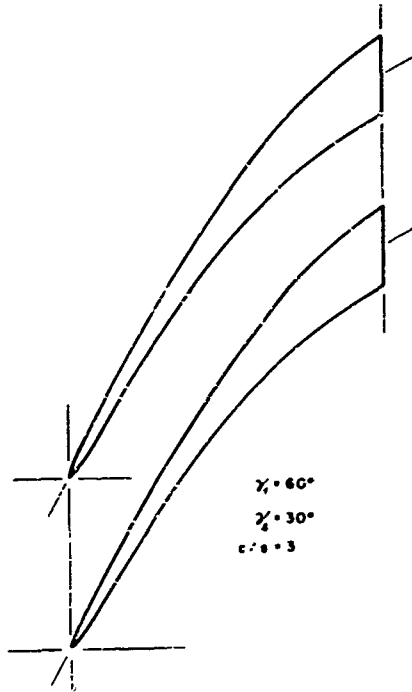$\chi_4 \cdot 30°$

$c/s \cdot 3$

Figure 7. Second-Generation Supersonic Rotor Blading
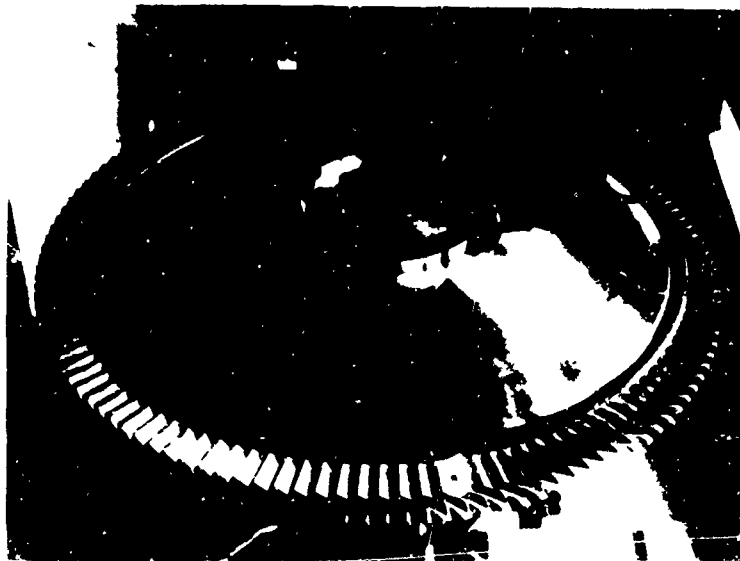

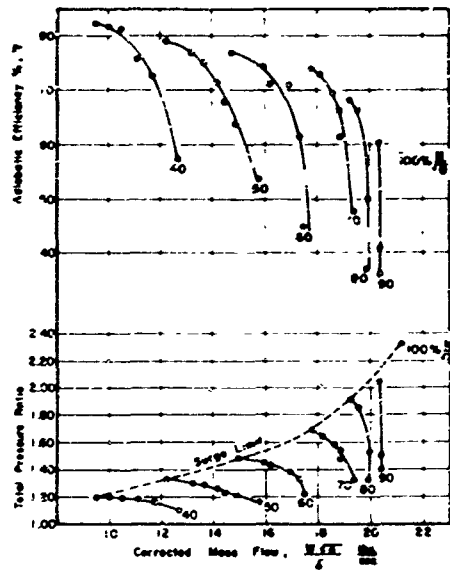Figure 8. Circular Arc Supersonic Rotor

Figure 9. Preliminary Performance Characteristics,
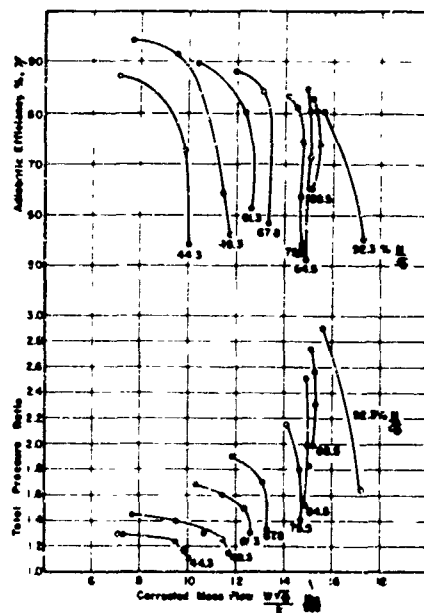Circular Arc Rotor

Figure 10. Preliminary Performance Characteristics,
vKIFD Rotor

42

the test program conducted at ARL on a 5-inch-diameter, blunt-trailing-edge rotor (Reference 1). They did no⁺ adequately describe the complex flow processes. Subsequent development of the more accurate prediction technique, the theoretical program previously discussed, pointed out the design error before the test data was available and the present experimental performance was anticipated.

Future tests will be conducted at reduced thickness to spacing ratio. In addition, leading edge modifications are planned for the first rotor to test the effects of leading-edge bluntness. Likewise, annulus modifications are planned for the second rotor after its initial tests to determine if a converging annulus in combination with somewhat thinner blunt-trailing edges would significantly reduce the sudden enlargement loss. Stator development is being pursued concurrently with the rotor investigations.

SUMMARY

In some applications such as small gas turbines, direct-lift engines, and supersonic cruise engines, the use of a supersonic compressor could substantially reduce the cost, complexity, size, and weight of the overall system. The supersonic compressor research program conducted by ARL has obtained results which while not yet conclusive are very encouraging. However, in spite of our anticipated ability to demonstrate this type of compressor, the proof of this development is still in its application to production engines. For this, we encourage integration of this system into a specific engine requirement.

ACKNOWLEDGMENT

VI. REFERENCES

1. E. G. Johnson, H. von Ohain, M. O. Lawson, K. R. Cramer, "A Blunt Trailing Edge Supersonic Compressor Blading," WADC TN 59-269, 1959.

2. H. W. Emmons (Ed.), Fundamentals of Gas Dynamics, Princeton University Press, 1958.

3. C. T. Carmen, "Development of the Supersonic Compressor Test Facilities at the Arnold Engineering Development Center," AEDC-TR-65-169, 1965.

4. A. J. Wennerstrom, S. Olympios, "Quasi-Three Dimensional Solutions for the Blunt-Trailing-Edge Supersonic Compressor," ARL 66-   (to be published).

44

First Lieutenant Robert Poplawski is assigned to the Swirl Chamber Research Group at the Aerospace Research Laboratories. He holds a B.S. degree in Mechanical Engineering from the University of Massachusetts, and was graduated from the Air Force Institute of Technology in 1964 with an M.S in Aeronautical Engir ering. Lt. Poplawski is an associate member-at-large of Sigma Xi.
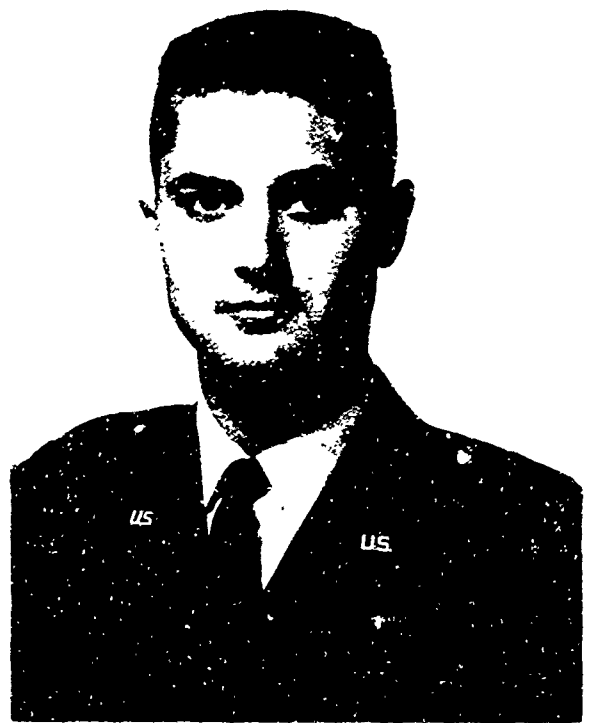
First Lieutenant Roger A. Miller is serving as a mechanical engineering officer in thermomechanics at the Aerospace Research Laboratories. He received his commission as a distinguished graduate of the University of Maryland ROTC program. In 1965, he graduated from the Air Force Institute of Technology with an M.S. degree in Materials Engineering. Lt. Miller is a member of the American Society of Mechanical Engineers and the Society of American Military Engineers.

THE ARL INERTIAL PARTICLE SEPARATOR FOR

MILITARY TURBINE POWERED VEHICLES

LT. ROGER A. MILLER
LT. ROBERT POPLAWSKI

AEROSPACE RESEARCH LABORATORIES
OFFICE OF AEROSPACE RESEARCH
UNITED STATES AIR FORCE
WRIGHT-PATTERSON AIR FORCE BASE, OHIO

I. INTRODUCTION

As previously pointed out by Green and Lane[1], dusts, smokes, and mists could be collected by gravitational settling, inertial and centrifugal separation, washing and wet scrubbing, electrostatic precipitation, filtration, and sonic or ultrasonic agglomeration. Each of these methods has found application in various industries depending in general on the type of particle one desires to separate, the concentration of particles, the required efficiency of collection and the economy of a particular method.

Gravitational settling is usually considered impractical for a particle of size less than 50-100 microns because of the large

This work at the Aerospace Research Laboratories (ARL) was initiated under Project 7116 on a means of ultra-microscopic particle separation (less than one micron). While ARL's principal interest is in the general area of internal flow, including basic studies on supersonic swirl flow under Project 7116, a by-product of this research is in the area of dust separation. This paper is devoted to the specific fallout of the basic research-separation techniques and the potential use for military turbine powered vehicles

settling time required. Thus, it has no possible application in the separation problem for turbine powered vehicles.

Inertial particle separators, and in particular the cyclone separators, have found wide application in industry because of the simplicity of operation, low investment cost, low maintenance costs, low resistance to gas flow, and ability to separate 100% of all particles above a range of 20-30 microns. Unfortunately, the commercial separators cannot efficiently separate out particles below 10 microns and thus their application has been limited.

Electrostatic precipitators, although capable of separating out extremely fine particles, require high voltages (25-100 KV) for operation, high initial investment, and have numerous dust removal problems. For example, dry materials sometimes must be dislodged from the electrodes by mechanical means. For wet substances, arrangements must be made to wash off the collecting electrodes. The degree of complexity thus makes the electrostatic precipitator unsuitable for gas turbine vehicle operation.

Washing and wet scrubbing would require carrying a liquid on the vehicle. Since this would increase vehicle weight and complicate logistics and maintenance, washing and wet scrubbing is not considered practical for turbine vehicles.

Filtration of dust laden gases with cloth, viscous, or fibrous filters have been used extensively in the automotive industry and on both fixed and mobile turbine engines[2]. They possess the ability to separate out extremely fine particles (less than one micron), however, as the run time increases, the pressure drop across the filter increases and eventually the filter must be cleaned or replaced. The interval between cleaning or replacement will vary depending upon the dust concentration. Since maintenance and logistics present problems, it appears that filters would not be practical for all military turbine powered vehicles operating in dusty environments. For example, helicopters might employ filters when maintenance is not a large problem; however, tanks operate many miles from central maintenance units and filters are not practical.

Sonic and ultrasonic methods are used to agglomerate particles so that they can be collected by some other means. The equipment consists of a generator, a resonant enclosure and a collector such as a cyclone. The generator sets up standing waves in the enclosure where the particles are coagulated. After coagulation they are separated by

a cyclone or some other type of separation device. Sonic and ultrasonic methods have been found to be effective down to approximately 0.1 micron. However, the sound generators must have outputs of 10 to 15 kilowatts, the concentration of the particles must be high, and the frequency required for agglomeration depends upon the particle size. Sonic and ultrasonic coagulation has only found limited application and it is not practical for military turbine vehicles because of the amount and complexity of the required equipment.

A summary of the capability of the various types of commercial particle separators is given in Fig. I[3]. From this figure and the previous discussion, it is apparent that only a greatly advanced inertial separation can meet the following requirements:

1. Efficient separation of micron size particles.
2. Low pressure drop.
3. Compactness.
4. Low ejection energies for dust removal.
5. Usable for mobile installations.
6. No replenishment, i.e., water for liquid scrubbers.
7. No maintenance.

The main problem of current commercial separators is the inability to satisfy the first four listed criteria.

Since so many areas in advanced nuclear, electrical, and chemical propulsion, pumping techniques and other advanced energy conversion and transfer processes depend upon multi-component and multi-phase flows and ultra microscopic separation, a portion of the energetics research at ARL has concentrated in this general and fundamental research regime. The following section describes briefly the history, general results and theoretical considerations involved in this research. One specific application of this research, an inertial particle separator for military turbine vehicles, and future plans for this particular by-product will also be discussed.

II. BASIC RESEARCH

Inertial Particle Separator Research

In the early part of 1961, scientific personnel at the Aerospace Research Laboratories (ARL), initiated a program to study advanced nuclear propulsion processes. From the results of this study[4], an expanded research program was formulated which included a fundamental approach toward solutions of ultra microscopic particle separa-

tion. This fundamental approach concentrated on areas such as super-
sonic two-phase flow, free condensation, and swirl or curved flows.
Investigations were conducted on swirl flow devices of high specific
volume flow capacity with exit Mach numbers in the subsonic and super-
sonic ranges. The initial considerations were focused upon secondary
flow phenomena, determination of tangential Mach number capabilities
and the energy transfer phenomena involving vortex decay in the regions
near the axis of symmetry. Fundamental investigations on separation
phenomena in two-phase flow included: similarity considerations for
particle separation including the effects of turbulence, particle size and
density, and the nature and the conditions of the carrier gas.

Based on the results of a two-phase flow analysis, a low-pressure-
ratio pilot model swirl chamber was constructed in late 1961, which
for the first time employed a reversed secondary flow pattern. Ex-
perimental tests of this device were made using talcum powder and air.
From the theoretical analysis, separation of a 2.5 micron size particle
was expected. The experiments confirmed that the crude model separated
all particles above two microns [5]. Based on these results, a high pres-
sure chamber was designed and fabricated of steel (see Fig. 2). Aero-
dynamic testing was performed from mid 1963 to early 1964 [6]. These
tests led to the design of a new multiple injection chamber (see Fig. 3)
which has been subjected to extensive aerodynamic and performance
tests [7,8]. Because of the difficulty in probing the high pressure swirl
chambers, low pressure chambers (see Fig. 4) were used extensively
for particle separation studies, flow pattern visualization, and for
diagnostic probe development.

Because of the testing success, many possible applications in the
classified and unclassified areas are under investigation. These ap-
plications include: electro and magneto fluid dynamic energy transfer
processes, medical uses, novel nuclear propulsion concepts, and an
inertial particle separator for military gas turbine powered vehicles,
which is the subject of this paper.

Inertial Separator for Military Turbine Vehicles

ARL's in-house results in the field of inertial particle sep-
arators for ultra microscopic particles encouraged represent-
atives of the Detroit Arsenal, Army Tank Automotive Center, to
request of ARL to undertake an in-house investigation of the use
of an inertial particle separator for micron sized separation.
The separator would be used for military gas turbine powered

surface vehicles. Approaching the problem of dust damage to turbine engines, three areas of ingestion were considered: gross damage, erosion, and deposition.

Gross damage to gas turbine engines usually is caused by ingestion of nuts, bolts, rocks or other relatively large objects. In general, gross damage can be minimized by good housekeeping practices, carefulness and/or the use of coarse screens. Thus, separation of the large objects from the gas flow is only a desirable feature of an inertial particle separator and not a requirement.

Erosion and deposition are mainly caused by particles above one micron. This contributes to severe engine damage and can result in complete engine failure. However, to protect military gas turbine engines, the four previously mentioned separator attributes must be satisfied. These are, particle size separation (η), pressure drop (ΔP_t), compactness, and minimum energy required for dust ejection (ξ'). For instance, separators are commercially available which can satisfy one or the other of these requirements but not all simultaneously. Conventionally clustered cyclone separation may satisfy compactness and have low pressure drops but cannot satisfy the low ejection energy requirements.

Some of the initial research separators that ARL has used to satisfy these requirements are shown in Figures 5 through 9. Fig. 5 is a high dust loading chamber designed specifically to study dust retention within a swirl chamber. It is an outgrowth of the low pressure multiple injection chamber as shown in Fig. 4 which was designed to study ultra microscopic separation and therefore has a relatively "high pressure drop" (70 inches of water). For this reason, it is not suitable as a dust cleaner on the inlet of a turbine vehicle.

Figures 6 through 9 are illustrations of the various experimental chambers used to study optimization in design for dust cleaners to be used on military turbine vehicles. A discussion of this test program and the results obtained to date can be found in the later chapters of this report.

Since the fundamental approach was taken to solve the ultra microscopic separation problems a large amount of the know-ledge can be directly applied to the microscopic separation case. In both cases the particle dynamics and the fluid flow patterns are

the same, but they differ in the pressure drop required for separation. The flow patterns of the ARL reverse flow devices and pressure drop requirements are discussed in the following section.

By relaxing the <u>ultra</u> microscopic separation requirement however, devices have been built which will separate particles in the micron size range with pressure drops on the order of 7 inches of water. These devices were designed specifically as dust separators for use on military turbine powered vehicles in response to a need for which there is no commercial solution available[10].

III. ARL FLOW PATTERNS

ARL initial fundamental studies have shown that in order to have effective separation of ultra microscopic particles, a number of requirements must be satisfied[8]. The principal features of these requirements are high angular velocities, long residence times, low turbulence levels, and prevention of leakage of dust laden boundary layers into the exhaust region.

An illustration of a swirl chamber that satisfies the above principal requirements is shown in Fig. 10 (which is a schematic of Fig. 3 and illustrates the flow pattern). The fluid dynamic process can be briefly described as follows:

The entering air is tangentially admitted along the chamber walls. This injection method slightly overcompensates the skin friction torque created by the end walls, thereby reversing the secondary flow, as illustrated in Fig. 10. The reversed flow pattern provides the following major advantages:

(1) A flow field inside the chamber of the free vortex type is generated, thus providing high pressure ratios and high angular speeds.

(2) Long residence times due to the separation process beginning at the center of the chamber.

(3) Low perturbation level since the disturbed gas is ducted out of the chamber (through the exit duct shown in the figure).

(4) Centrifuged particles are swept into the exit duct and out of the chamber while the clean air is discharged through the exhaust into the compressor intake.

The "flow reversal" as treated in the references[4,6,7,8,9], has been found to be effective for both sub micron particle and phase separation. In the case of phase separation, condensation of vapors has been used to form a mixture of a gas and sub micron particles. Using air and a small amount of water vapor, experiments by Fletcher et al,[8] have shown that 90% of the condensation cloud (see Figs. 11 and 12) could be separated under the proper conditions. The water droplets formed in the swirl chamber were found to range between 0.25 and 0.30 microns by classical light scattering techniques. The high pressure devices investigated by Fletcher have high pressure drops (greater than 100 psi) and the low pressure devices designed for ultra microscopic particle separation still have pressure drops on the order of 70 inches of water.

IV. ARL EXPERIMENTAL DUST SEPARATION RESEARCH

A systematic research program has been devised and experimental studies have begun. This program has the objective to determine the most important separator parameters upon the following major performance characteristics.

1. Separation efficiency (η); Effects of;

   a. Inlet scrolls versus inlet vanes (figs. 6 and 7).
   b. End wall admission (Fig. 9).
   c. Reverted geometries (Fig. 8).
   d. Geometric scaling by multiple units.

2. Reduction of total pressure drop through separator (ΔP_t); Effects of;

   a. Radial outward diffusion of core flow downstream of the exit.
   b. Axial length of exit tube.

3. Minimum dust ejection energy (ξ); Effects of;

   a. Radial distance between core and dust ejection region.
   b. Mode of scavenging air admission.

4. Maximization of volume flow per unit frontal area (compactness); Effects of;

   a. Ratio of exit diameter to chamber diameter.
   b. Ratio of axial length to exit diameter.
   c. Ratio of axial to tangential velocity of core flow.

The major experimental single unit chambers have been fabricated. Some of the important experiments have been completed, but the investigations are still in an early stage. The experimentation on dust ejection has shown that the minimum energy required for dust ejection is obtained at the maximum radial distance between core and point of ejection. It has been found that the required secondary scavenging air can be less than 1/3 of one per cent of the intake flow rate (the pressure required can be less than five psig). This is one to two orders of magnitude better than current cyclone separator scavenging capabilities. The overall separation performance of the chamber constructed as in Fig. 6 with an outer chamber diameter of ~10 inches and an exit opening of ~5 inches has been determined as follows:

a. Using coarse Arizona road dust (0-200μ, see Appendix for size distribution), separation efficiencies of 97% by weight, were obtained. The separation efficiency was 75% using fine Arizona road dust (0-5μ, see Appendix).

b. Flow rates of 500 cfm were obtained.

c. A pressure drop of 7.5 inches of water occurred through the device.

d. Maximum particle size escaping from the exhaust ranges between 2 and 3 microns.

Additional experiments have been conducted using flow rates of 750 cfm and 1000 cfm through this type of chamber with all other results as indicated above remaining essentially the same.

As the investigations continue (on a single unit device constructed as shown in Figs. 6 through 9), along the lines indicated in the first paragraph, it will be possible to obtain, with a clustered device, the performance parameters shown in Table I. Fig. 13 shows the schedule of work that will lead to a clustered device with the optimum configuration. The program is designed to initially optimize on each of the characteristics listed in paragraph one. Subsequent study of the relationships between these performance factors will yield the optimum separator performance characteristics.

Table I

Projected Characteristics of the ARL Clustered Separator

$\dot{m}/A$	Mass flow rate/separator frontal area	1.5 lbm/sec ft^2
L	Length of separator	1/2 ft
η	Separation efficiency	100%($\geq 1\mu$)
ΔP_t	Total pressure drop	4 inches H$_2$0
ξ	Scavenging air required for dust ejection (% of total flow rate)	0.5%

V. CONCLUDING COMMENTS

The early work at the Aerospace Research Laboratories was directed toward the general area of internal flow, a part of which is ultra microscopic particle separation research using vortex and curved flows. Because of the ultra microscopic particle separation requirement, the separator had a high pressure drop. Experiments showed the high pressure drop chambers were capable of separating over 90% of the water vapor introduced into the chamber, and thus verified theoretical models. As a result of the basic research in vortex flows, ARL was asked to consider the application of this research to a dust separator for turbine engines operating in a dusty environment. Since a dust separator on a turbine must have a high separation effectiveness, low pressure drop, be compact, require low dust ejection energy, and be relatively maintenance free, the combination of requirements are different in some aspects from consideration of the more difficult problem of ultra microscopic particle separation. For example, the dust separator must operate with only about 4-10 inches of water pressure drop while the high pressure devices operate with pressure drops near 100 psi and greater. However, the fundamental flow patterns remain essentially the same and thus research in one area has added to knowledge in the other.

The dust separators which have been tested at ARL show an overall separation capability equal to or greater than any commercially available unit. For example, as previously noted, the amount of scavenging air required for dust ejection (automatic cleaning) is one to two orders of

54

magnitude less than commercial separators. The separators being designed and built at ARL have the potential to increase particle separation capability without an increase in pressure drop. The flow rate per unit frontal area (cfm/sq ft) will also increase to a value comparable to or greater than the commercial separators. Thus, the future ARL Dust Separators are potentially superior to any commercially available device.

REFERENCES

1. Green, H. L., and Lane, W. R. Particulate Clouds: Dusts, Smokes, and Mists. D. Van Nostrand Co. Inc., Princeton, N. J. 1957

2. Mund, M. G., and Wright, T. E. "Design, Development and Application of Air Cleaners for Gas Turbines". Presented at SAE Summer Meeting June 11-15, 1962, Atlantic City, N. J. Paper No. 538B.

3. Lapple, C. E. Stanford Research Institute, 1959.

4. Hasinger, S., Mills, R. H., and von Ohain, H. J. P., Aerospace Research Laboratory Internal Document (Not Circulated). Jan. 1962.

5. Report on Research, 1 Jan. 1962 - 30 June 1964. Aerospace Research Laboratory Report Number ARL 64-1, July 1964, p VII-35.

6. Fiorino, T. D., Jr., and Poplawski, R., "Experimental Optimization of the Reverse-Flow Swirl Chamber". Aerospace Research Laboratories Report Number ARL 65-66, April 1965.

7. Poplawski, R. and Pinchak, A., "Aerodynamic Performance of Reversed Flow Vortex Chambers", Aerospace Research Laboratories Report Number ARL 65-219, October 1965.

8. Fletcher, E. C., Gyarmatny, G., and Hasinger, S., "Phase Separation in a Swirl Chamber". ARL Report in Progress.

9. Keller, M. R., and von Ohain, H. J. P., "Research Relevant to the Gas Core Reactor" Aerospace Research Laboratories Report Number ARL 64-189, October 1964

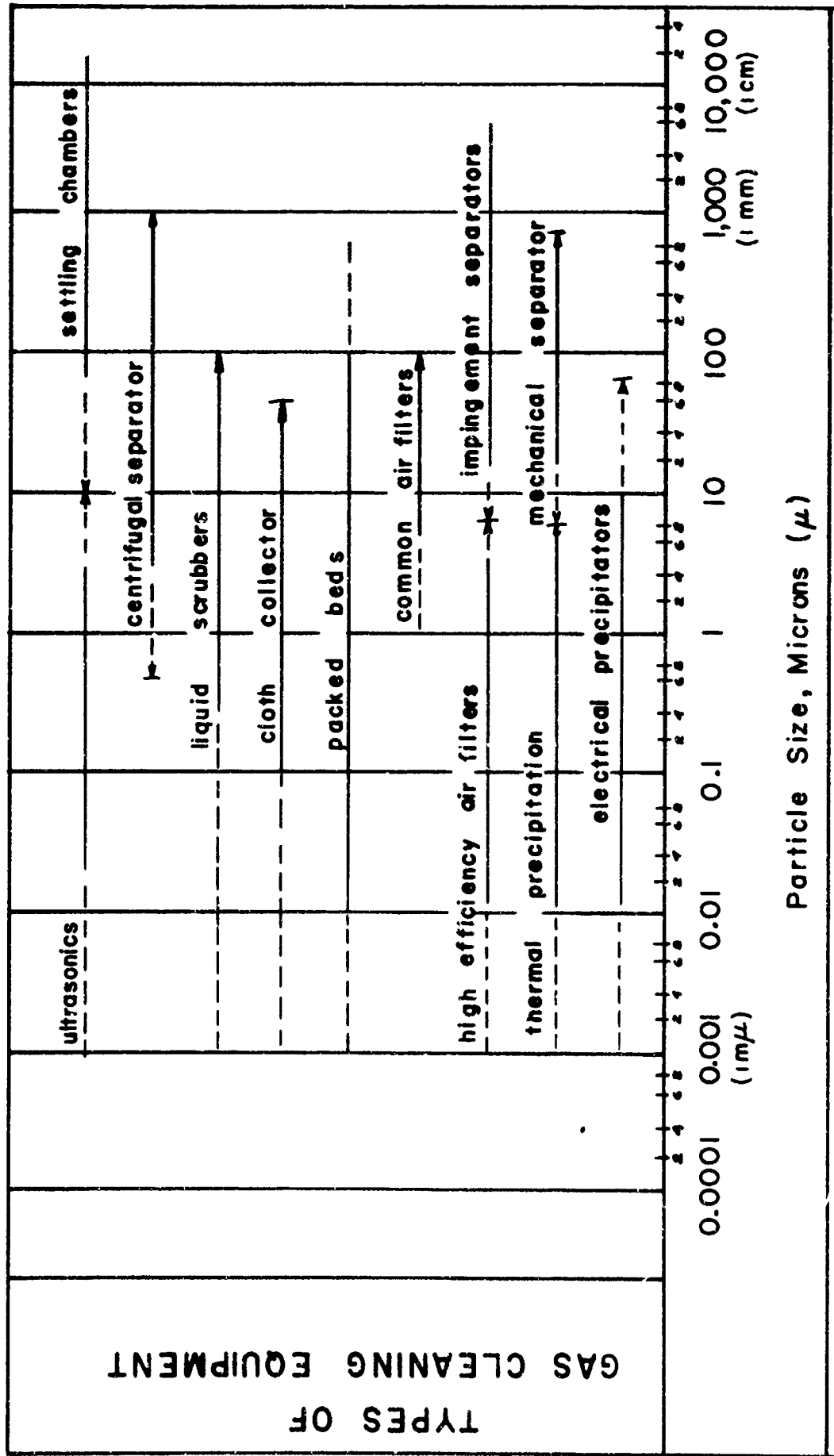10. Childs, R., U. S. Army Tank Automotive Center, Warren, Michigan Private Communication.

56

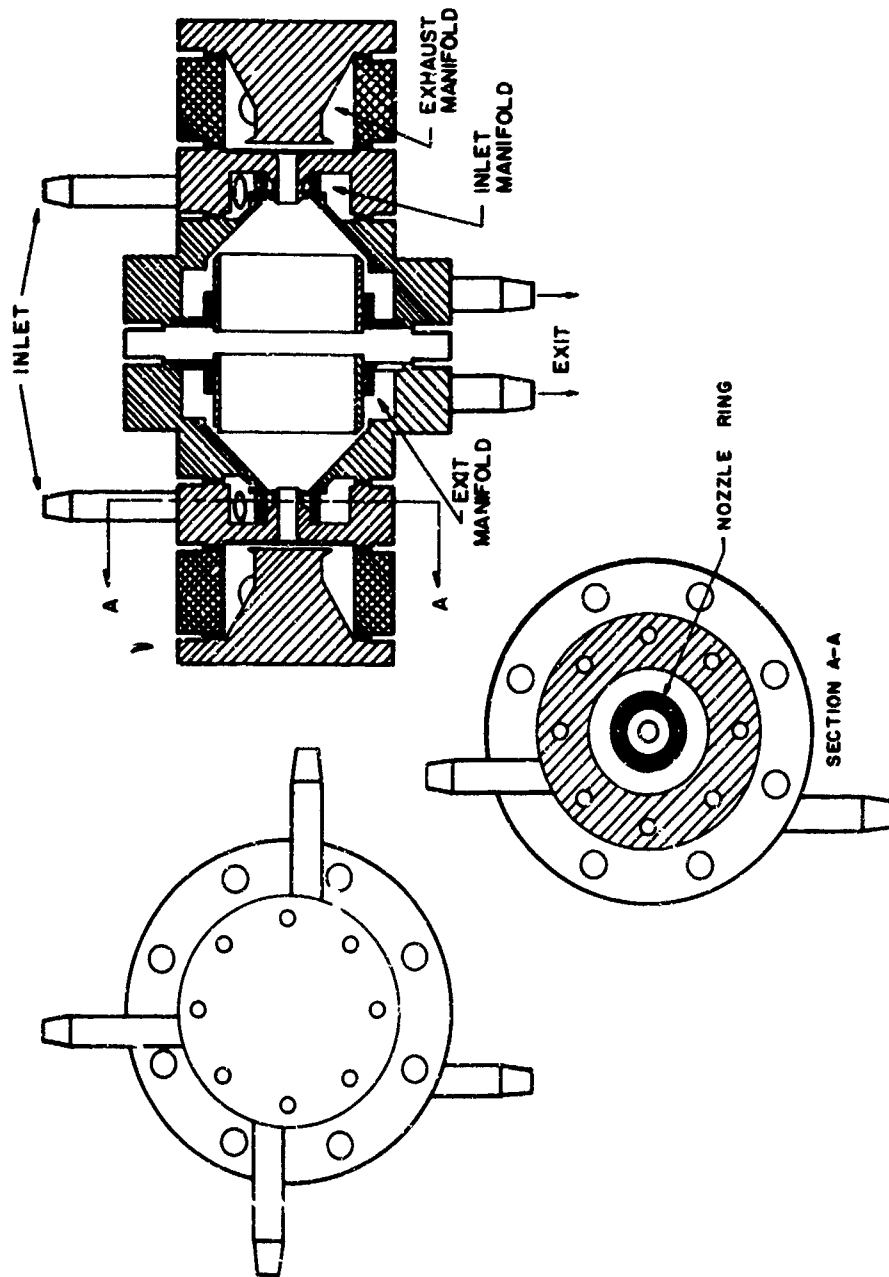Figure 1. Gas Cleaning Equipment for Various Particle Sizes
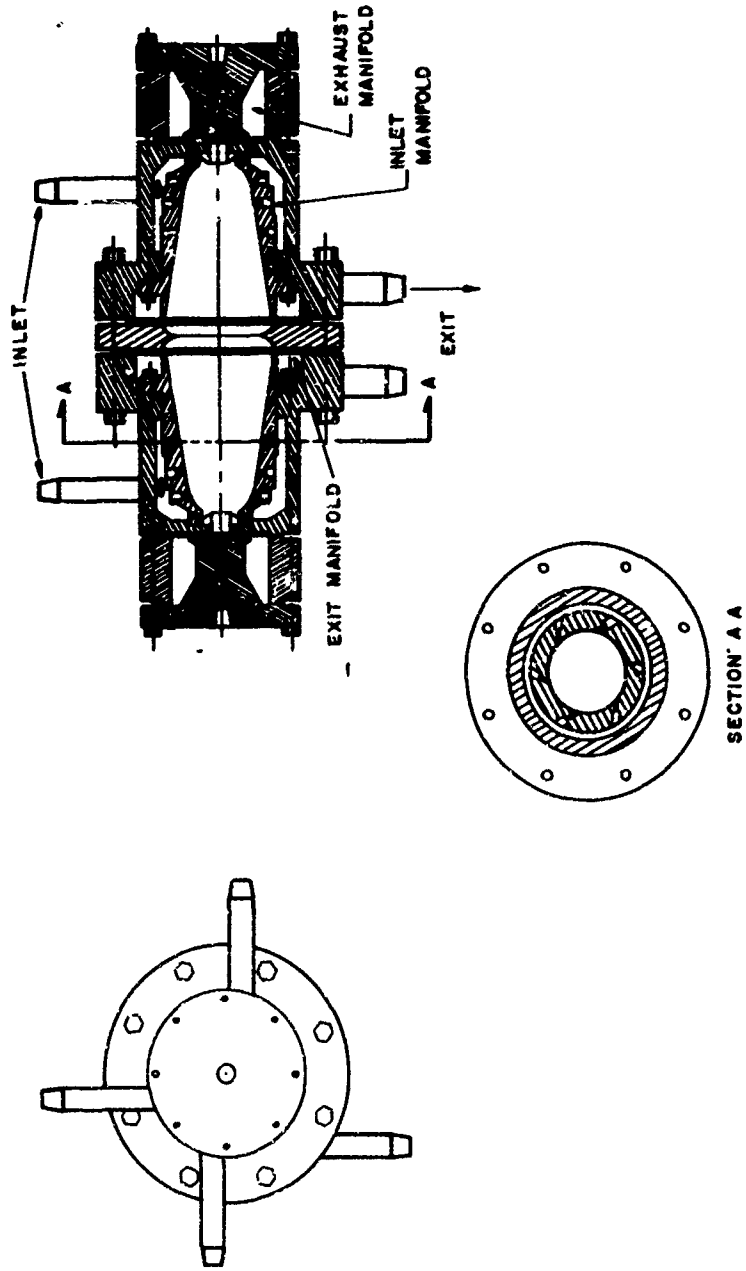
Figure 2. First High Pressure Swirl Chamber

Figure 3. Internal Geometry–High Pressure Swirl Chamber (Multiple Injection)
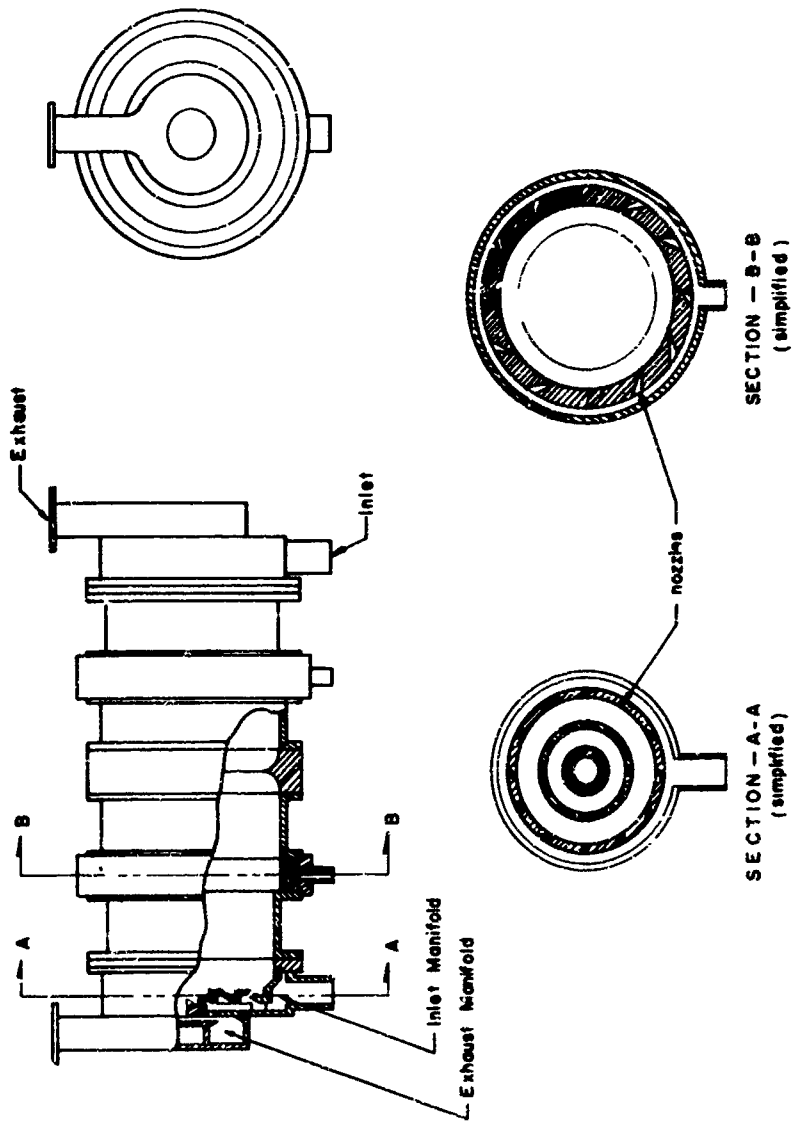
Exhaust

Inlet

B

B

A

A

Inlet Manifold

Exhaust Manifold

nozzle

SECTION — B-B
(simplified)

SECTION — A-A
(simplified)

Figure 4. Internal Geometry of Low Pressure Swirl Chamber
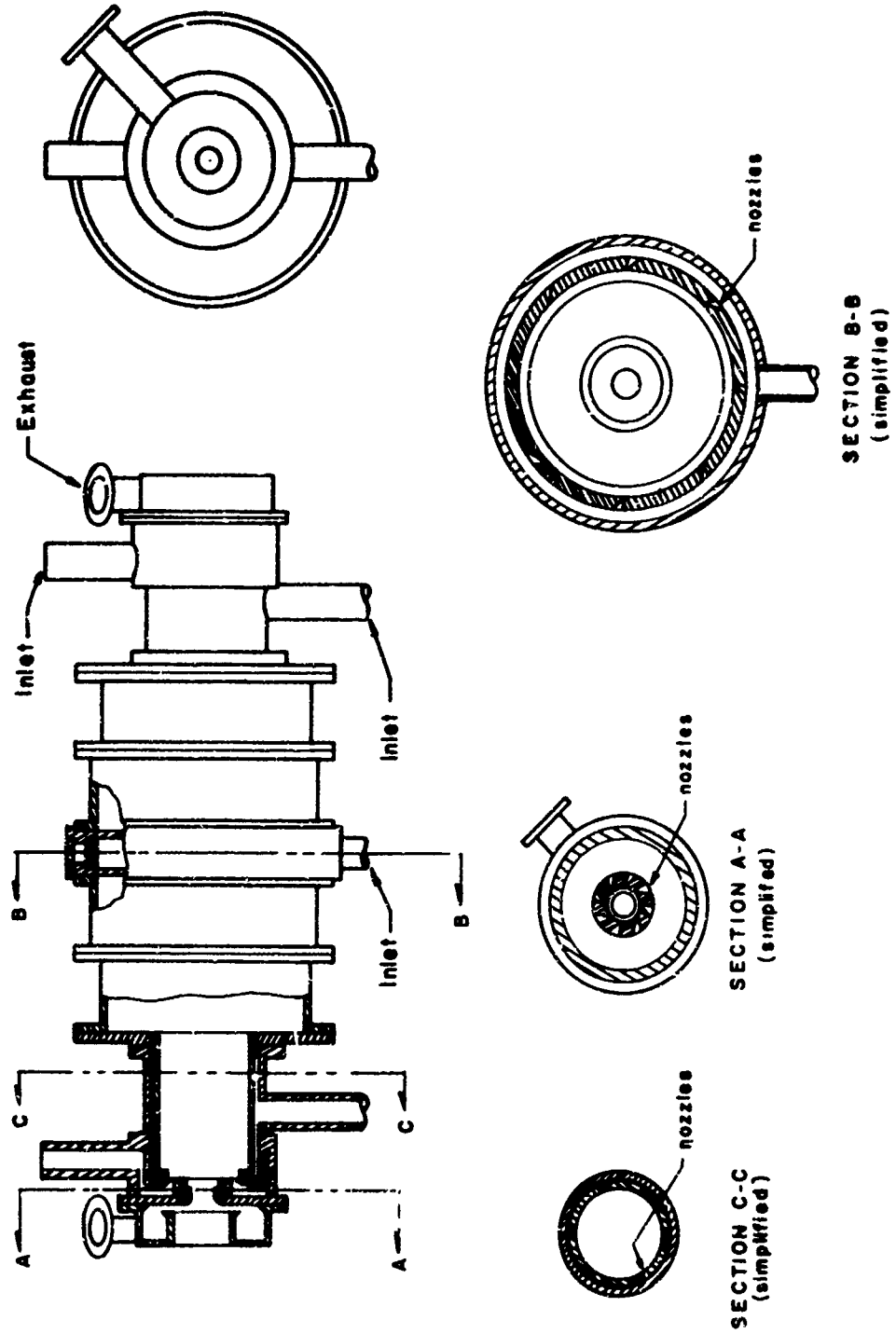
Figure 5. High Dust Loading Research Swirl Chamber

INLET

INLET

C

C

EXIT

B

B

A

A

COAXIAL
TUBULAR
INSERTS

INLET AND EXIT DUCTS
HAVE RECTANGULAR CROSS-SECTION

SECTION C-C
INLET SCROLL

SECTION B-B
EXIT SCROLL

EJECTOR
AIR FLOW

EJECTED
DUST

FLOW TO
COLLECTION BAG

SECTION A-A
DUST EJECTOR

Figure 6. ARL Dust Separator-Mark I (Scrolled Inlet and Outlet)

CUTAWAY SHOWING
INLET VANE ASSEMBLY

VANE DETAIL

SECTION B-B
EXIT SCROLL

EXIT

EJECTOR

AIR FLOW

SECTION A-A
DUST EJECTOR

EJECTED
DUST

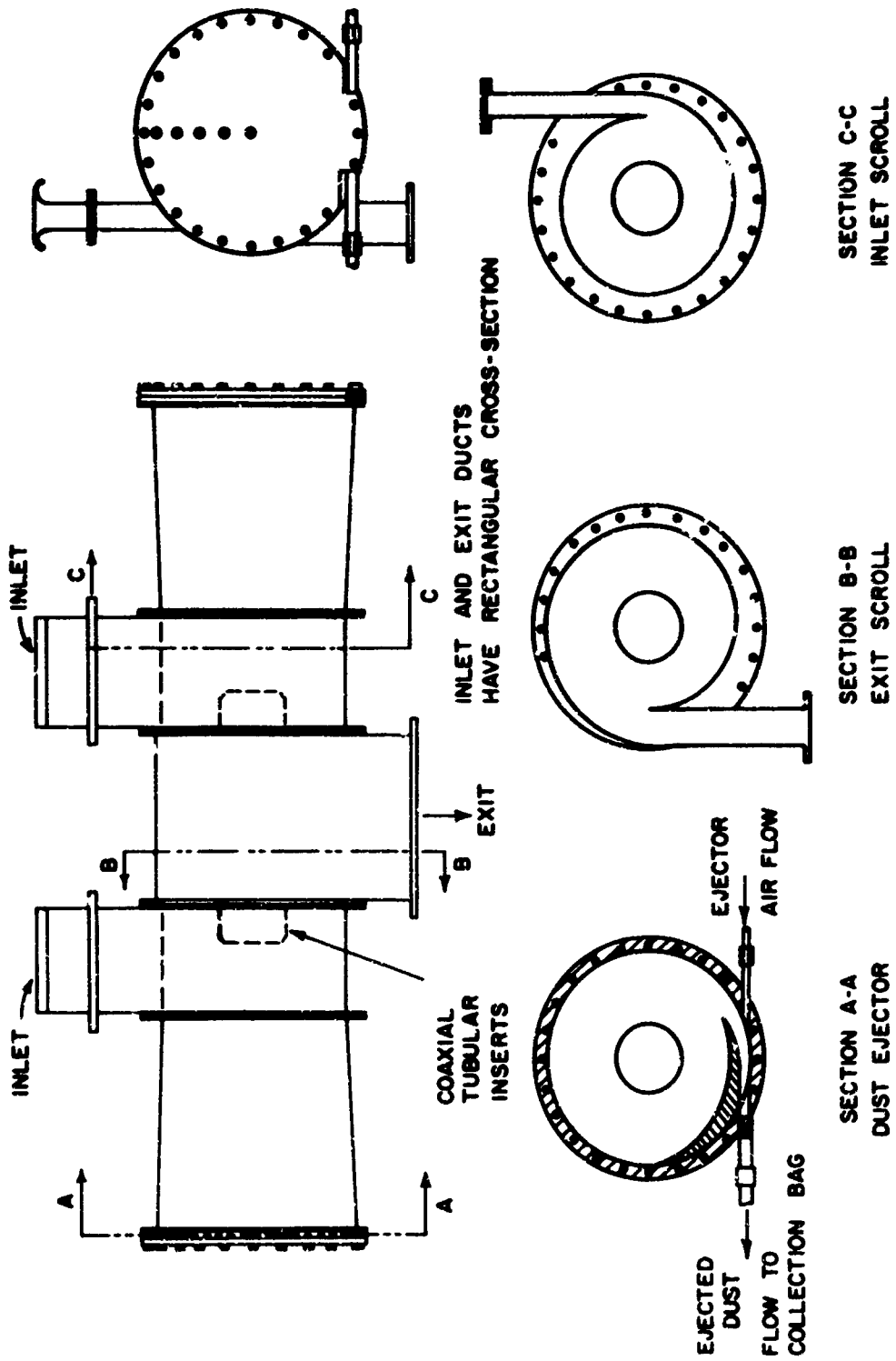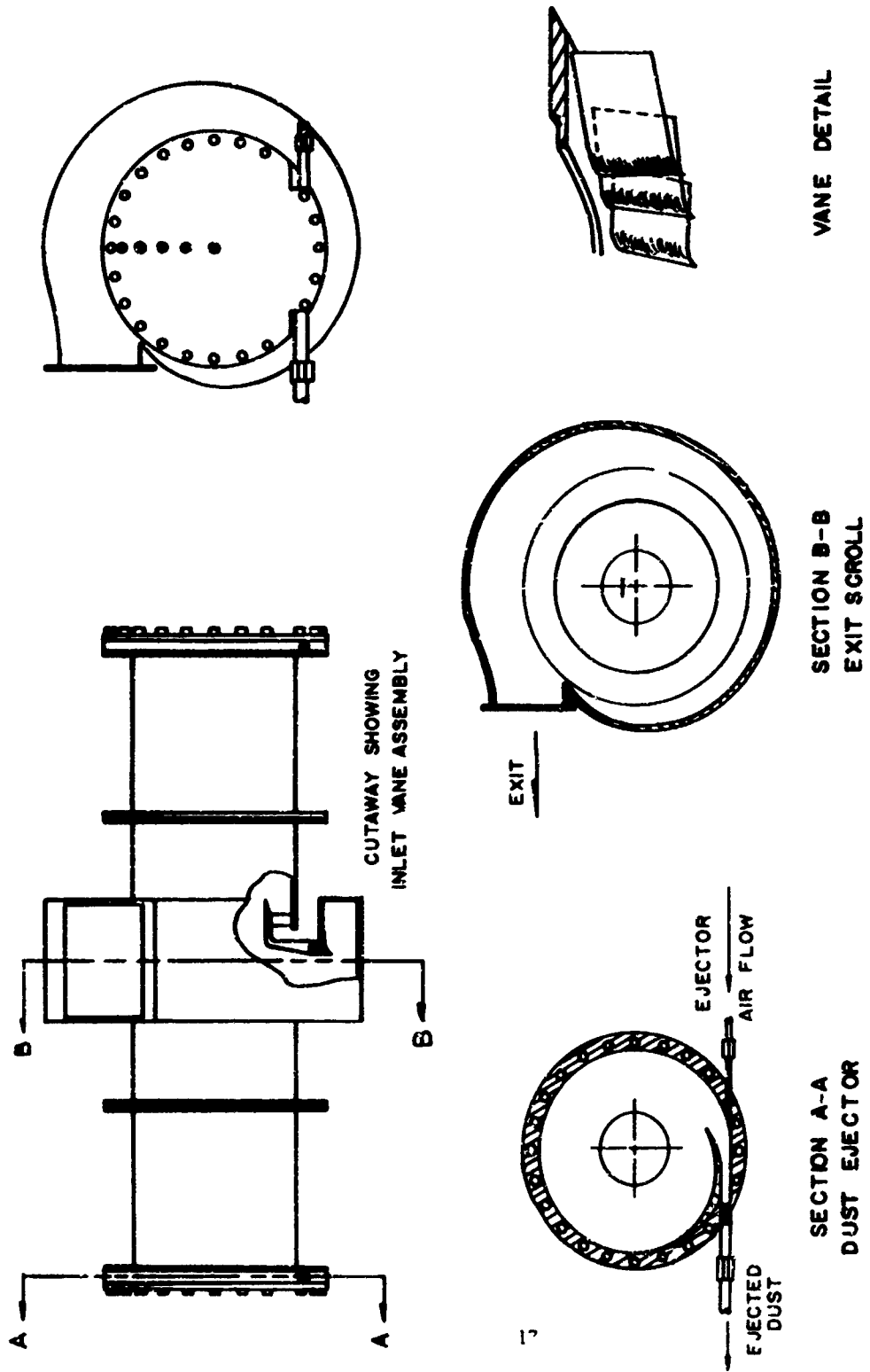Figure 7. ARL Dust Separator–Mark II (Vane Inlet and Scroll Outlet)
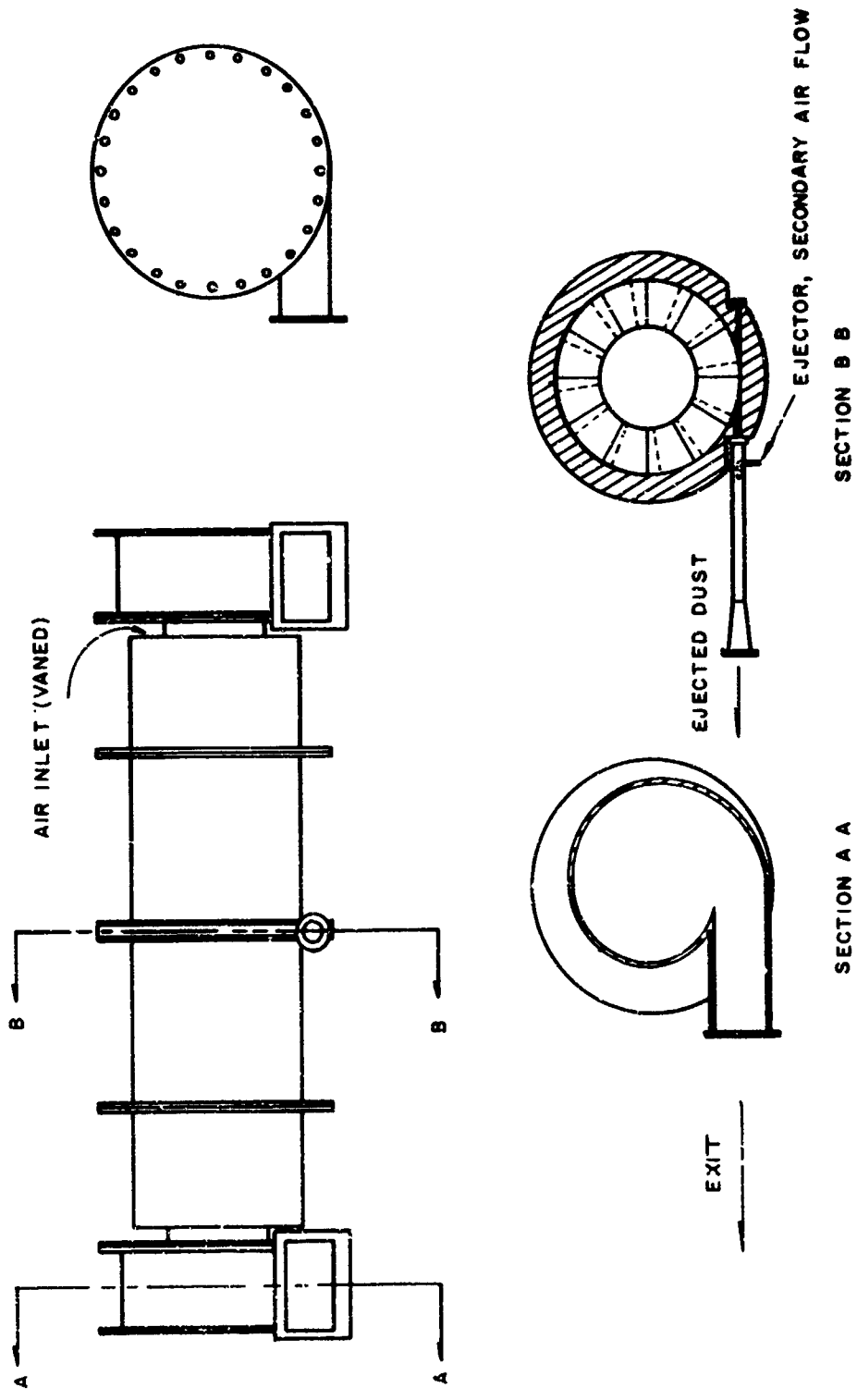
Figure 8. ARL Dust Separator-Mark II (Vane Inlet and Scroll Outlet-Reverted Configuration

END WALL
BLEED AIR

EXIT

END WALL
BLEED AIR

CUTAWAY SHOWING
INLET VANE ASSEMBLY

INLET VANES

SECTION A-A
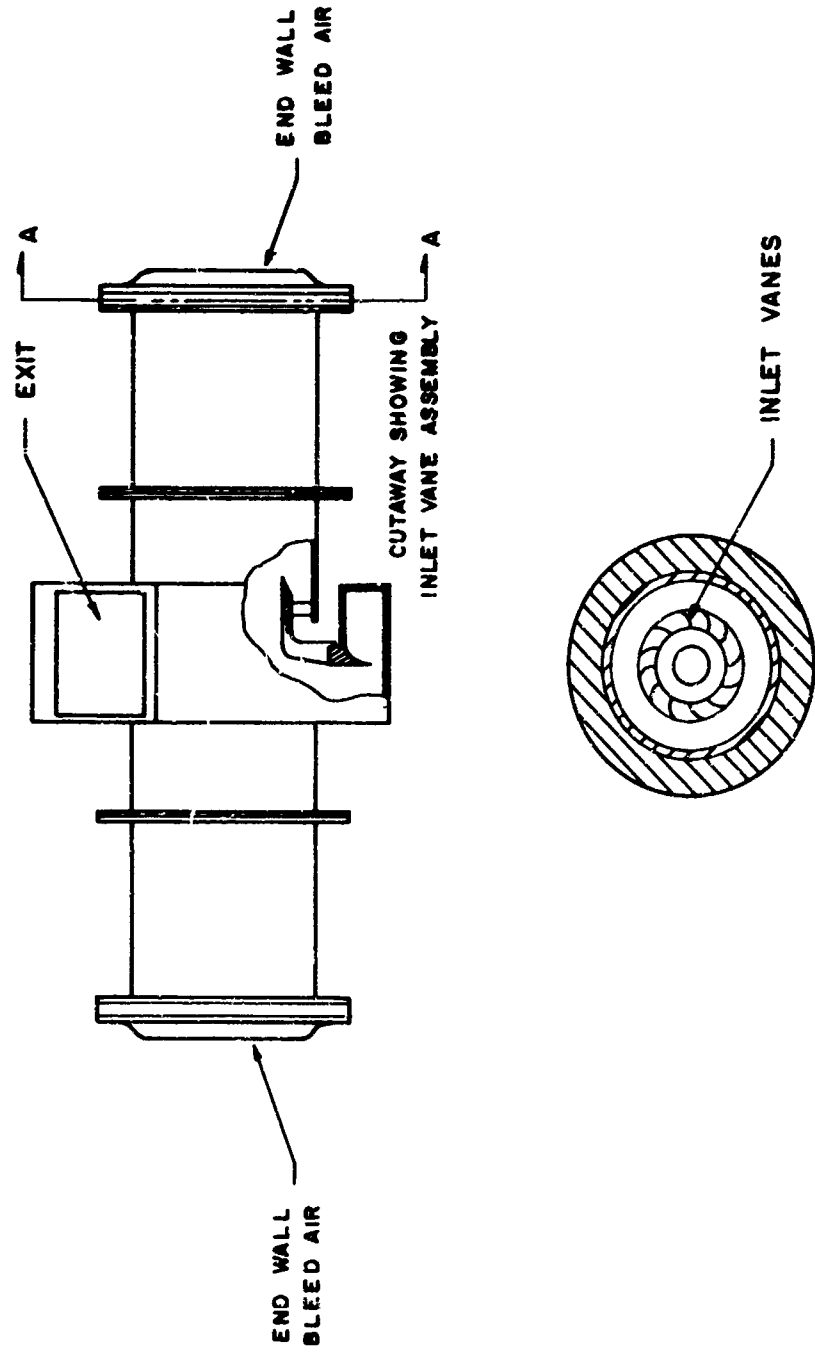
Figure 9. ARL Dust Separator–Mark II (Vane Inlet and Scroll Outlet–End Wall Bleed)

PRIMARY GAS
FLOW PATTERN

SECTION A–A

REVERSED SECONDARY
GAS FLOW PATTERN

INLET

EXIT

PARTICLE
FLOW
PATTERN

EXHAUST

Figure 10.   Swirl Chamber with Reversed Secondary Flow

Figure 11. Condensation Cloud in High Pressure Multiple Injection Chamber (Fletcher et al)

Figure 12. Radial Light Slice Showing Condensation Cloud in High Pressure Multiple Injection Chamber (Fletcher et al)
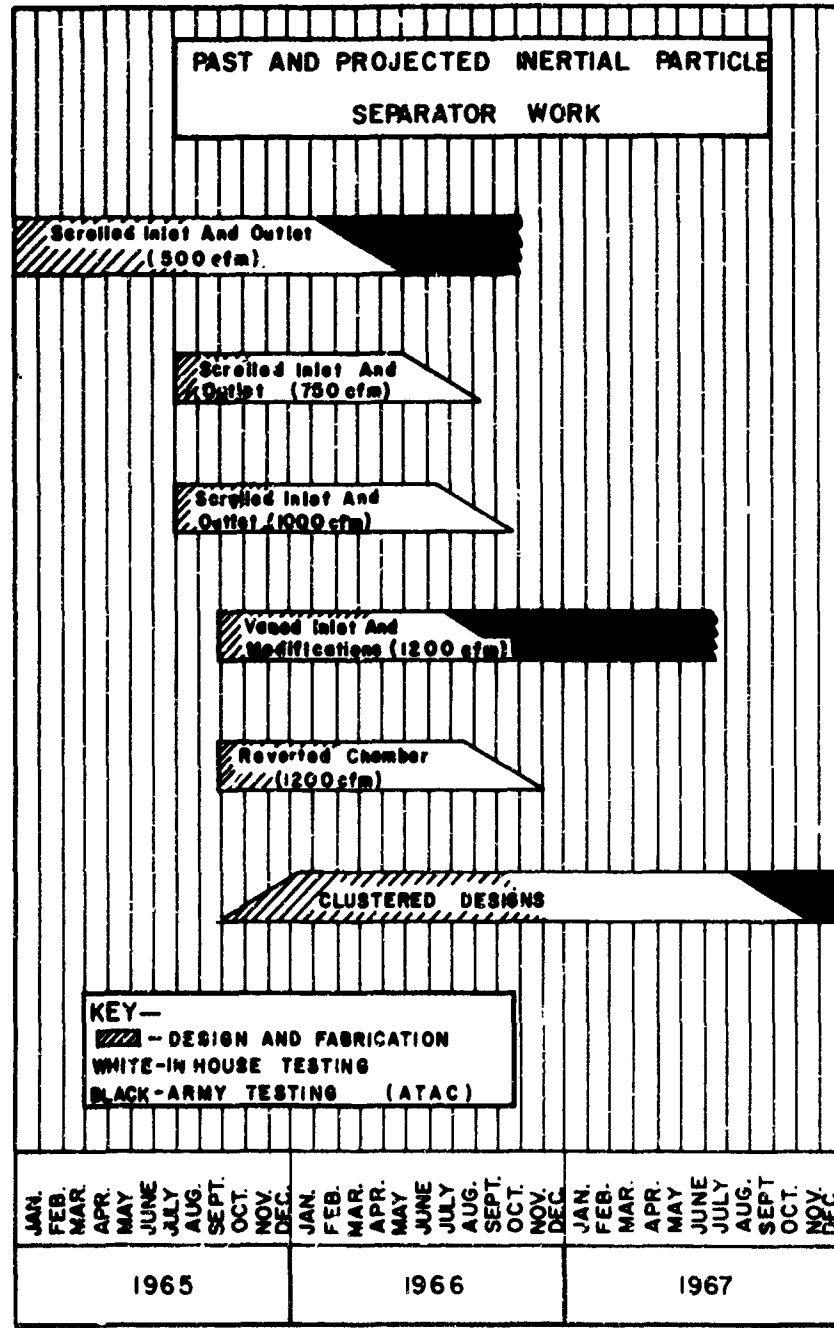
Figure 13. Past and Projected Inertial Particle Separator Work

APPENDIX

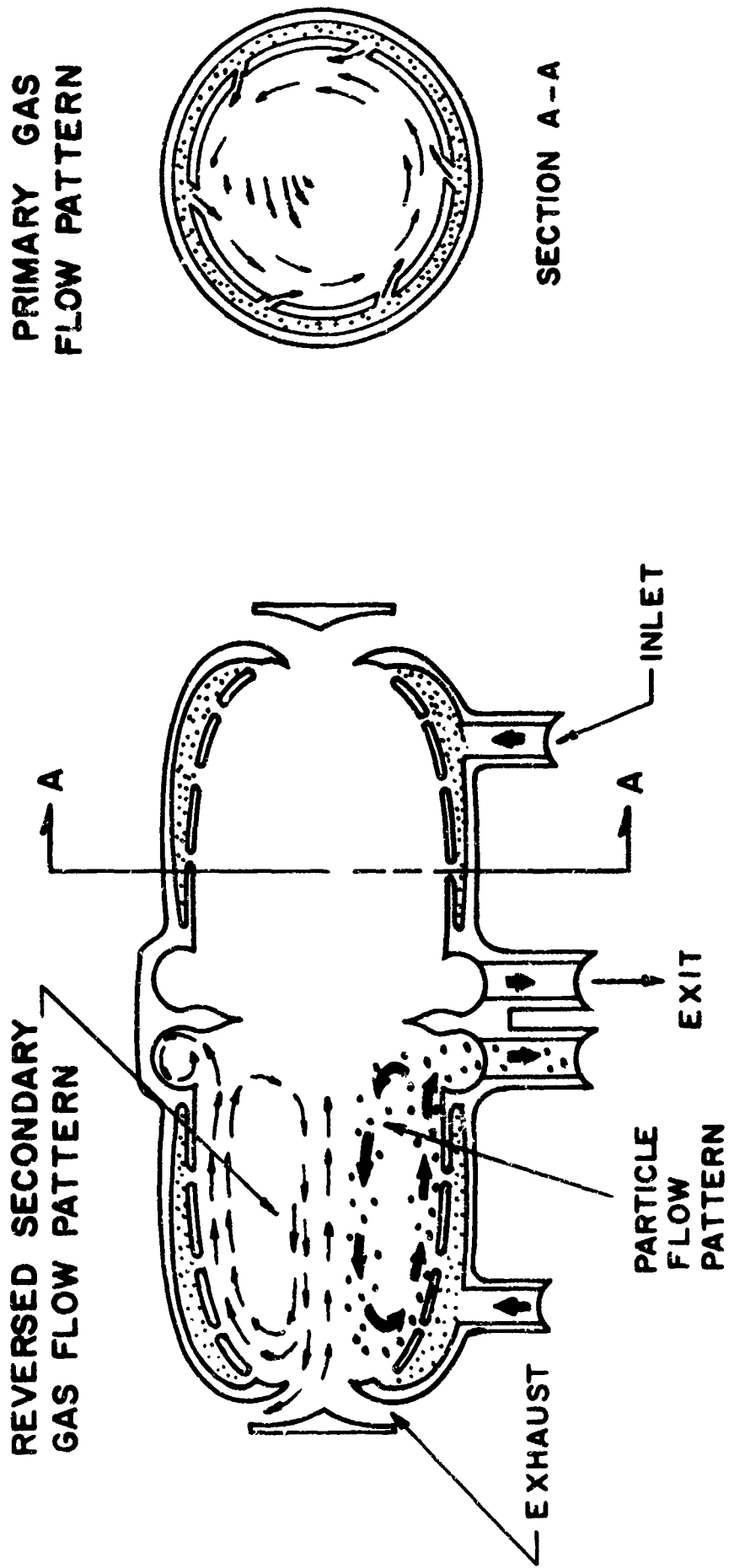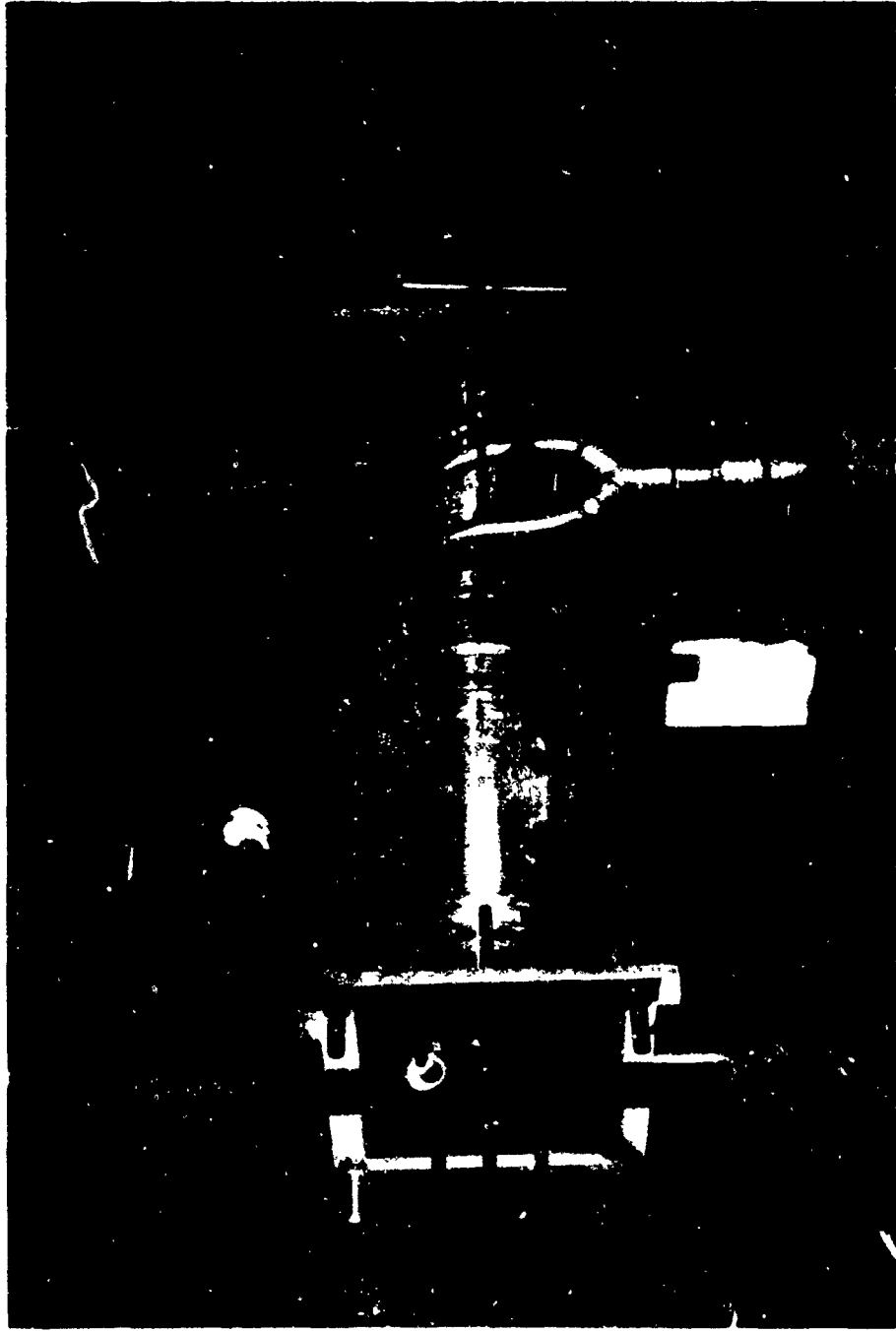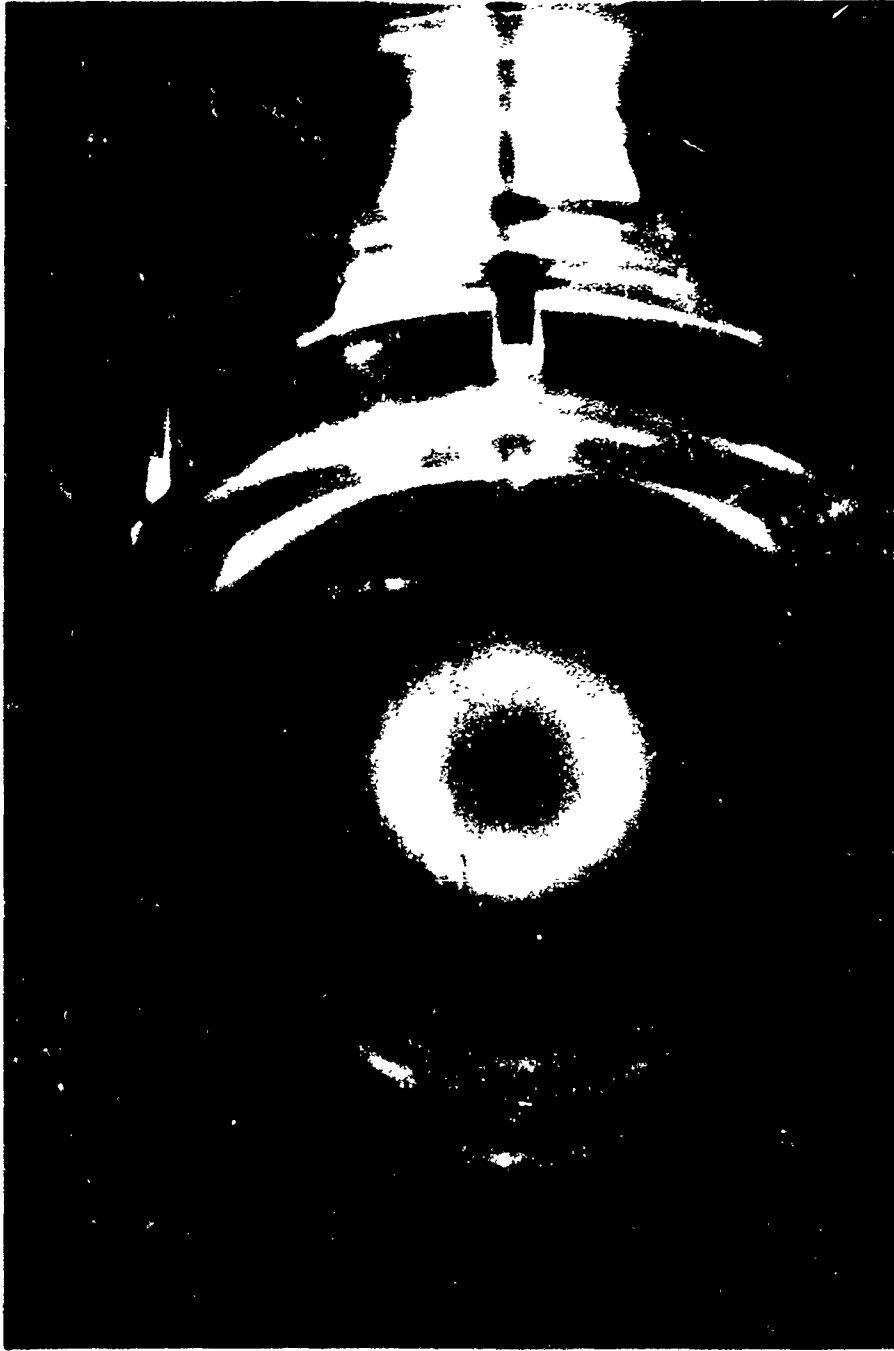## Arizona Road Dust Size Analysis

(by mass)

0-5μ Road Dust

	Percentage less than size	
Particle Size (Microns)	Stated by A-C (percent)	Analysis by ATAC* (percent)
10		100
5	96.3	99.7
4		97.6
3		92.8
2	90.7	79.9
1		46.0
0.8		35.6
0.6		
0.5	11.1	
0.4		13.3
0.3	1.9	
0.2		4.1

0-200μ Road Dust

	Percent of Total	
Particle Size (Microns)	Stated by A-C (percent)	Analysis by ATAC* (percent)
0-5	12 + 2	54.7
5-10	12 + 3	20.1
10-20	14 + 3	8.2
20-40	23 + 3	3.5
40-80	30 + 3	7.1
80-200	9 + 3	6.4

*ATAC - Army Tank Automotive Center, Warren, Michigan
Reports - CRN 15403-RA (Part 4, 1 September 1964)
CRN 51703-RA (Part 2, 24 November 1964)

Mr. Kenneth E. Kissell is a physicist in the General Physics Research Laboratory, ARL. He is currently pursuing research on the applications of photoelectric image devices to astronomical spectroscopy, and to recording and interpreting short-term variations in artificial-satellite brightness. Prior to joining ARL in 1957, Mr. Kissell served as Acting Chief of Data Analysis and Predictions, Space Track Control, AFCRC, and as instrumentation physicist at WADC. In 1954, he was a member of the Labrador solar-eclipse party, and in 1955 of the British Somaliland solar-eclipse party. Mr. Kissell has a B.S. degree in Astronomy and an M.S. degree in Physics from Ohio State University, where he is now a Ph. D. candidate. He has published a number of professional papers.

Photoelectric Photometry -
A New Tool for Satellite Signatures

Kenneth E. Kissell
Aerospace Research Laboratories
Wright-Patterson Air Force Base, Ohio

ABSTRACT

The experience gained since 1962 in the photoelectric measure-
ment of space vehicle brightness is outlined, and the methods used to
collect signature data on vehicles of brightness + 11 stellar magni-
tudes $(1/50 \, m^2$ diffuse scatterer at 1000 km) or greater are described.
Examples of light curves are given, and a model of a tumbling, dif-
fusely scattering cylinder is compared with a USSR rocket body. A
model of a specularly scattering sphere is compared with data collected
from three USSR vehicles whose orbital lifetimes indicated their being
of de-orbiting character. It is shown that these techniques offer a
relatively low-cost method of collecting optical signature data at ranges
much exceeding those at which resolved images could be obtained. The
bistatic and CW character of the technique is demonstrated, which,
combined with its inherent inverse-square law limitation on slant range,
suggests it as a valuable supplement to conventional radar techniques
and long focus imaging for the purpose of identifying the external charac-
teristics of satellites.

Introduction

Examination of a kinescope recording of the carrier rocket of
Sputnik IV, a recording obtained by the USAF Avionics Laboratory in
June 1960, raised several exciting questions about the quasi-periodic
character of the brightness changes exhibited by this spacecraft as
it tumbled across the sky scattering sunlight to the observer. Ques-
tions included the amplitude and rate of the brightness fluctuations
and whether these fluctuations characterized the vehicle shape and
surface characteristics.

Thus in 1961 - 1962 research was begun by the Avionics Laboratory and the Aerospace Research Laboratories on the dynamical brightness fluctuations of orbiting spacecraft and their possible importance on automatic exposure control in long-focus photography of such spacecraft. From the earliest results it was apparent that the integrated light received from a spacecraft contained very detailed information on the surface characteristics, surface finish, and dynamical motions of the target. Analysis of data from selected targets has demonstrated the potentialities of this passive technique to measure spin-axis orientation, vehicle geometry, and vehicle size-albedo product. The classification of vehicles by similarities in overall signature patterns, surface finish (specular, diffuse paint, or glossy paint), and surface protuberances has also been done. In some cases it may be advantageous to utilize radar-determined tumble-axis data as a starting point in the analysis since the analytical methods for optical determination of this parameter are still in their infancy. The optical data are suggested as a strong check, complimentary in character, to radar-determined data.

Optical photometry, with the sun as the nearly invariant source of illumination, is subject only to an inverse-square law limitation in range compared to radar's inverse-fourth power range limitation, is basically bistatic in the nature of the measurement, and is inherently of CW character with wide bandwidth possibilities. These are the advantages which optical photometry provides in the collection of signature information for the ground identification of satellites. The operation at optical wavelengths has the advantage of allowing discrimination of very small surface elements and of metal finish characteristics; this has the consequent disadvantage of alteration in signal strength by use of dark finishes, although even a 99-percent absorbing coating will reduce the signal by only five stellar magnitudes. One of the other factors in favor of optical signature work is the much lower cost per sensor since the technology of optical instrumentation is more advanced and less complex, no illumination energy is required to be provided, and high-performance photomultipliers are modest in price.

This paper is intended to review the exploratory work carried out at the Aerospace Research Laboratories on photoelectric photometry, and to indicate the direction of future work on this very promising signature tool. The application to satellite identification is an outgrowth of the more fundamental research problem undertaken at ARL on the optical properties of orbiting spacecraft.

Attack on the Problem at ARL

Because so little experimental work has been done in the study of the optical properties of orbiting space objects, the author has undertaken a program which includes

1. Development of techniques for collection of brightness data from the unresolved images of orbiting satellites over a diverse sampling of spacecraft..

2. Development of calibration techniques to allow these brightness data to be interpreted on an absolute scale.

3. Collection of a signature library from many different vehicles over a long span of time so as to allow study of secular effects on target brightness due to changes in dynamical motion or in the surface finish (degradation of specular finish or blackening of paint after months or years in orbit).

4. Collection of data on the brightness of unresolved targets while simultaneously resolving the target. This can be done with many spacecraft if the slant range is less than 200 miles and some spacecraft at ranges to 500 miles.

5. Development of analytical methods for interpreting the brightness data in terms of dynamical motions, configuration and size.

6. Extension of the simple broadband photometry to more specialized measurements of polarization and color effects on certain spacecraft which should exhibit such properties.

The first three of the above problems have been solved by a direct, relatively unsophisticated approach using equipment available as castoffs from other R & D programs or by use of standard apparatus. Special problems in precision tracking have been solved by combining the flexibility of a skilled human observer with innovations in a mechanical telescope mount to minimize the tracking problem. The calibration problem has been solved satisfactorily by applying techniques of classical astronomy. Data have been collected from over 80 different spacecraft during the last 48 months.

The present satellite tracker gives promise of providing excellent resolved images for comparison with unresolved brightness data. While the development of analytical techniques has not kept pace with the solution to the experimental problems, selected brightness records have been analyzed using approximate methods.

The results of ARL research in all of these areas is described below. Polarization and narrow-band photometry will be conducted in mid-1966.

Prior Work

Although over eight years have elapsed since the first orbiting of near-earth satellites, observation of satellites by optical means is still restricted to techniques allied closely to astrometry, i.e., the

location and cataloging of satellites by the position in space with only minor concern for the apparent brightness and color of the satellite. No serious attempt has been made outside of ARL in the recording of light curves of orbiting vehicles other than for a few exploratory, and generally very specific, purposes.

These prior efforts include attempts to use visual estimates of brightness to determine the range of fluctuations and times of maximum brightness[1-4] with intention to relate these to orientation to use photo-electric measurements for study of selective[5,6] and broad-band[7,8] absorption of sunlight in the upper atmosphere, and to deduce orientation of satellites specially equipped with mirrors[9-11] to produce specular flashes. More recently work has been directed at the surface properties[15,16] of the vehicles in terms of secular effects on the surface finishes. Several early proposals for the use of optical photometry involve use of specific geometrical forms for attitude determination.[17-19]

From examination of these early papers and from experience, the author observes that, in general, the application of photometric data is limited by the form, quality and quantity of data available. As is well known is variable star photometry, visual estimates require the careful use of nearby photometric standard stars which are chosen to match in color temperature in order to eliminate the personal idiosyncrasies of the observers. The accurate timing of brightness peaks by visual observers is unreliable for similar reasons owing to anticipation and reflex errors in the observer. The light curves of space vehicles can be interpreted usefully only if relatively complete data can be collected by photoelectric methods. The photoelectric photometry of space vehicles requires more precise tracking of the vehicle than that required for astrometric applications. This is necessitated by the small field apertures which must be used to reduce the sky background to levels which are at least as low as the satellite signal at its minimum brightness. The small apertures will also reduce the occurrence of false signals due to chance passage near bright stars.

The ARL Tracker and Photometer System

If one seeks to do photoelectric photometry, it is necessary to place the satellite image within a small entrance aperture at the focal plane of the telescope in order to reduce the sky background to tolerable levels. In the case of stellar photometry, the precise guiding of an equatorial mount allows use of apertures of only a few seconds of arc apparent field; the aperture is chosen to assure capture of the entire diffraction disk of the star while allowing for seeing variations in the image position. The much larger and varying rate of a satellite target requires apertures measured in minutes of arc rather than seconds to assure capture of the vehicle during most of its transit. Experience with the early satellite photometer[1,2] at the ARL Sulphur Grove Site

shewed that apertures of 3-7 minutes of arc were tolerable with a 3-axis tracking system.

The photometer system now in use at the ARL Field Site is attached to a Nunn mount originally built by Boller & Chivens, Inc., for mounting of a satellite tracking camera in a 3-axis system, (given to ARL by Avionics Laboratory when its original test function was completed) now modified to provide a 4th axis of adjustment. The 24-inch optical system is of a conventional Cassegrain design and of 384-inch focal length. This is shown in Figure 1. Apertures of 8, 15, 30, 60, and 120 seconds of arc are available in the simple photometer head to restrict the field of view and consequently the total sky background radiation seen by the photomultiplier. In the present practice only the 120-arc-second aperture is used for vehicle tracking. A highly selected RCA 7029 photomultiplier is used. This tube design is especially suited for use under high ambient light levels. The photomultiplier is energized by a logarithmic feedback power supply which maintains a constant output current from the photocell by regulating the dynode voltage. This gives a roughly linear response in stellar magnitudes (a logarithmic scale use to measure the brightness of stars) over a range of 10-15 magnitudes (dynamic range of 10^4 to 10^6) and effectively prevents overloading of the photomultiplier by accidental overexposure. The dynamic response of the photometer electronics[13] is flat to approximately 5000 cycles. A schematic of the photometer is shown in Figure 2. The data recording system is shown in Figure 3.

The feedback voltage of the photometer circuit, which is the nearly linear signal output, is fed in parallel to a recording oscillograph with 1 KC galvonometers and to an FM tape recorder for more versatile storage. It is expected that the output display will allow timing of satellite brightness events to within 1 millisecond, and that the output light curves would display satellite brightness fluctuations with frequencies of up to 1 KC. The most rapidly-varying satellite yet observed ad a tumble period of 0.46 seconds and exhibited four distinct peaks in this interval. The equivalent input frequency of 8 cps is quite low compared with the system capability. Brief transients occurring in only a few milliseconds have been observed from satellites exhibiting specular behavior. One example is the Alouette top-side scunder satellite which exhibits bright flashes from its 75-foot whip antennas. The most abrupt events yet observed were the xenon lamps on the ANNA and GEOS vehicles which exhibited a rise from magnitude + 9 to -3 in less than 2 milliseconds, a brightness increase of 6.5×10^4. The flash discharge times of both these vehicles are being measured and reported to NASA for their use in studying the performance of the vehicle control system.

In its present configuration the photometer will, on a dark, transparent night, yield measurable records above the system noise for satellites of + 11 stellar magnitudes i.e., 1/100 of the threshold of

Figure 1. ARL 24-inch Aperture, 4-Axis Tracking Telescope

naked eye sensitivity. The limitation is incurred by four factors; first, the light-collecting aperture of the optical system; second, the necessity of using field-defining apertures of two arc minutes for adequate tracking tolerance thus placing the lowest sky background levels at approximately + 12 stellar magnitudes; third, the wide band-width of the photometer system which passes much greater noise power than a conventional stellar photometer and hence imposes a high noise level, and fourth, usage of an uncooled photomultiplier which, while highly suited for high ambient light levels without over-load or fatigue, is not the most sensitive tube which could be employed. Of these restrictions, the field aperture and lack of cooling of the photomultiplier are the most fundamental.

Tracking is by aided manual track using a boresighted guiding telescope of variable power. The operator controls the angular rate of the telescope in the tracking direction and position of the telescope in crosstrack. The operator uses visual position with respect to crosswires and a target-modulated audio tone as cues in maintaining boresight on the vehicle within his 60-arc second tolerance. Track can be maintained about 75 percent of the time for vehicles at 250 km slant range. This is made possible[1,2] by the small-circle fit to the satellite trajectory through use of the unique 4-axis telescope mount-ing, an innovation introduced by the author to allow collection of data from low altitude vehicles. Figure 4 shows the comparison of the adequacy of various mountings to generate a trajectory fit against a satellite in a 1000-km high, near-circular orbit.

A Graham transmission drive allows tracking in either direction at rates continuously variable from zero to 7100 seconds of arc per second in three speed ranges. Cross-track motion is effected by a DC motor for slewing and a selsyn generator-motor pair for fine control. Azimuthal setting is by hand and the azimuth axis is locked prior to the satellite transit. Shaft-position digitizers permit the operator to read the tracking or cross-track angles to ± 0.1 degrees on a Nixie display without moving from the mount.

Acquisition and tracking of the satellite is visual and manual. The mount is positioned to predetermined angles at a favorable point along the predicted trajectory. The acquisition is enabled by 13 x 125 elbow telescope with a 6-degree field of view; the tracker drive is acti-vated when the target reaches the center of the field of view. The active field of the photometer within the guider field is checked by bore sighting on a convenient star. The guiding telescope is main-tained parallel through a unique parallelogram mounting while keeping the eyepiece essentially fixed for the comfort of the observer.
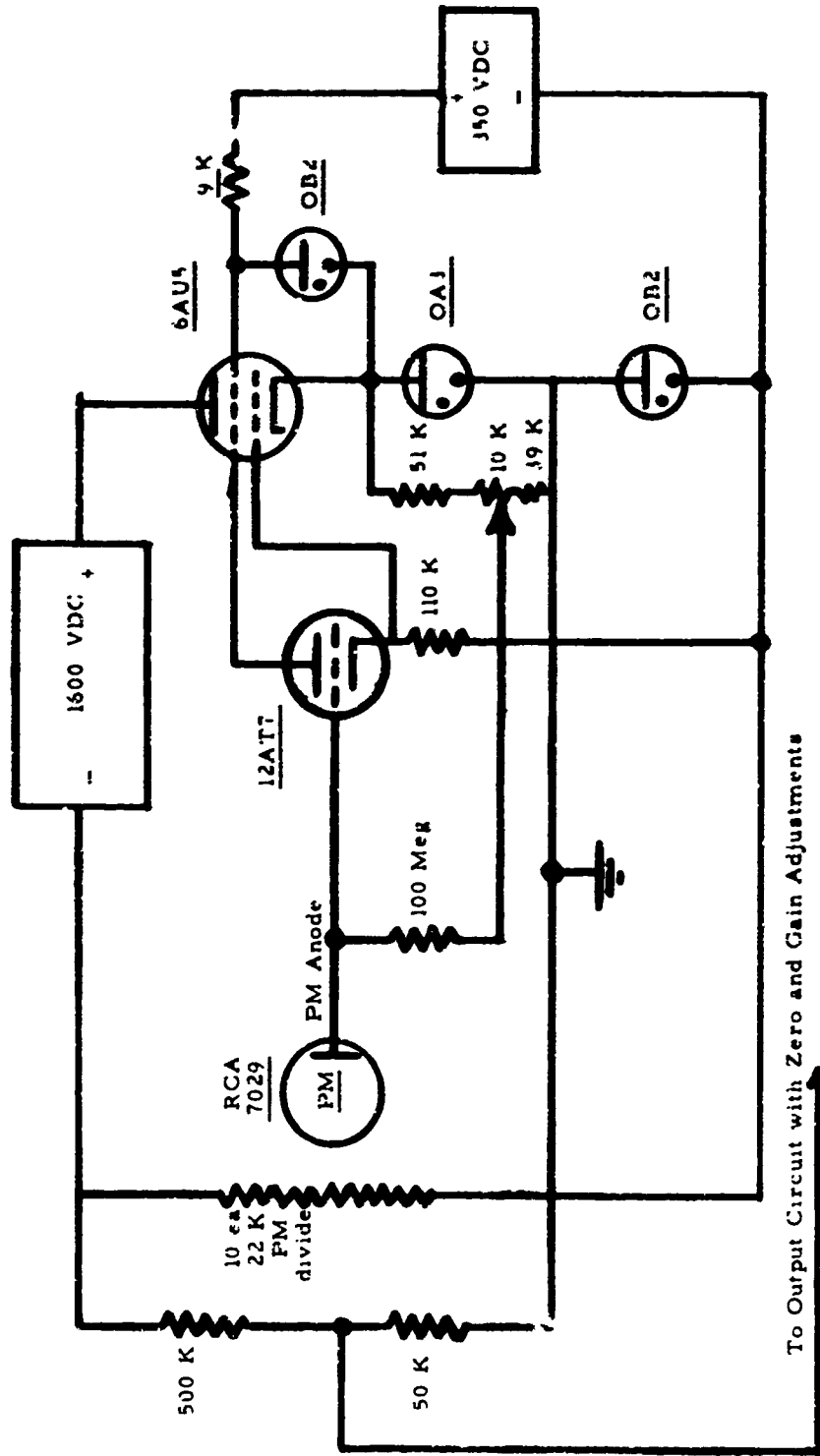
Figure 2. Tyson high-frequency Logarithmic photometer circuit

Calibration Techniques Employed

Examination of the photometric records included in this paper shows that the signal-to-noise ratio of this system is very high except when the target brightness lies near the limiting magnitude of the photometer system, i.e. where the contribution of the sky background through the defining aperture is comparable to the signal from the target. The excellent reproducibility of the periodic light variations, especially of fine detail on complex light curves, suggests that quantitative measurements of the target-scattered luminous flux could lead to inference of target size if it were possible to determine other geometrical parameters such as orientation. Since the source of illumination of the target is essentially constant (the direct sun plus the contribution of earthshine from a changing but narrow crescent of the illuminated earth's surface), the uncertainty in the luminous flux incident on the target is small. The luminous flux leaving the target is then a modulation of the incident flux scattered in the direction of the observer.

The flux received by the observer at any instant from the satellite is dependent upon numerous physical parameters of the target, the atmosphere, and the geometrical relationship of the target, observer, and sun. These include size, geometrical shape, attitude, local optical albedo of the surface elements including its diffuse and/or specular character, atmospheric transmission, slant range, and phase angle of contributing surface elements. Some of these parameters must be known or must be approximated in the case of a specific target in order to estimate the other parameters. Almost any attempt to construct the unknown parameters in a quantitative way relies on quantitative knowledge of the absolute or at least relative power received from the vehicle.

Determination of the luminous flux received from a target outside the atmosphere is most conveniently done by comparison of the unknown flux to that received from stars whose brightness is known to be invariant. This is the method of calibration being used by the author. Several hundred stars whose colors are nearly that of the sun have been selected for use as calibration sources. A few of these are used throughout a given observing session to establish a calibration curve for the instrument.

This measurement of luminous flux received from an unresolved target is a classical problem in astronomy where attempts to characterize the stars by the luminous flux received dates back to Ptolemy, who used naked eye relative estimates to classify 1008 stars into six classes which he called first to sixth magnitude. After elaboration of this visual method in the 19th century by Argelander and Gould and the later use of photographic photometry by many workers at Harvard
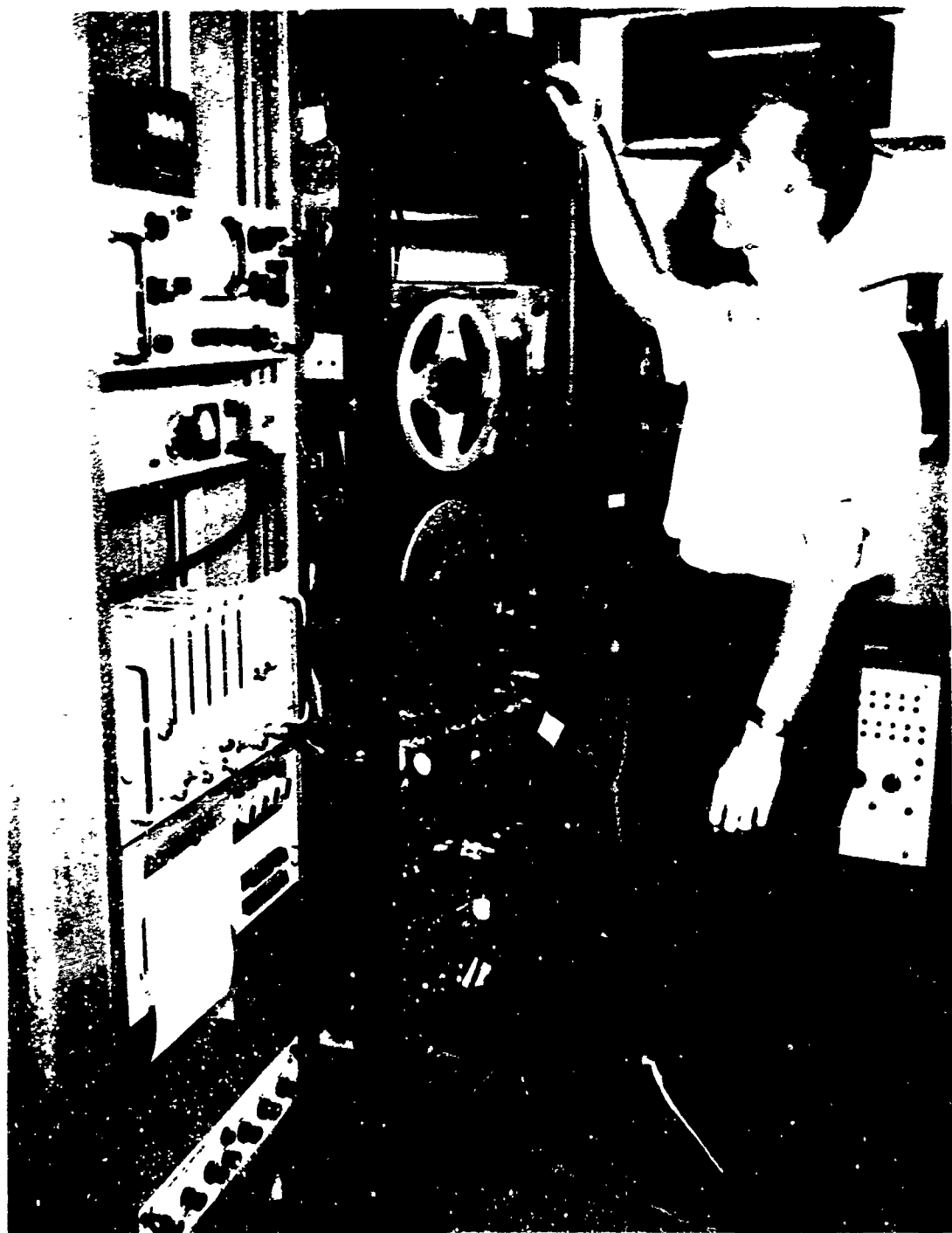
Figure 3. Logarthmic photometer and FM recording system

College Observatory in the early part of this century, the presently-accepted method[20,21] for the determination of stellar brightness is that of measuring the photocurrent which would be produced by the star if the star were observed outside the earth's atmosphere using a standard photocathode and standard filters. The accepted method is referred to as fundamental stellar photometry. Recent papers by Eggen,[22] containing three-color photoelectric photometry of 1066 G-type stars (sun-like in color) ranging from apparent magnitude + 0.34 to + 11.09, i.e. from a brightness comparable to the Echo satellites down to the threshold of the ARL instrument, and by Iriarte, Johnson, et. al.[23] containing five-color photometry of 1325 bright stars of all spectral types from magnitude -1.45 to + 6.75, provide a large number of standardized sources well spread throughout the celestial sphere, sources whose absolute brightnesses have been determined to within better than two percent in most cases. The approach taken by the author is to use some of these 2000-odd stars for calibration of the photoelectric system immediately preceding or following the collection of data from a spacecraft target.

To infer the accuracy with which the target brightness can be determined, one can examine the internal consistency in determining the brightness of any one of the calibration stars from the others. A plot of a mean calibration curve determined from six nights of observation is shown in Figure 5. The points plotted as circles were collected from stars observed near the zenith, i.e. observed through a slant path of only one air-mass; these were used to define the calibration curve. Also plotted are the measured output of stars observed at lower elevation angles whose brightness has been further attenuated by passage through more than one air mass. These demonstrate the importance of determining the atmospheric extinction which is present at the instant of transit of the satellite and along the regions of the sky in which the satellite was observed. Extinction corrections are applied in a manner analogous to the conventional astronomical method.[24]

Preliminary examination of star calibration data has led to the conclusions shown in Table 1, as the accuracy of the present ARL system. The accuracy varies somewhat with brightness range of the target because of the non-linear character of the present logarithmic electronics. It is considered that the absolute brightness of the satellite target can be determined with an accuracy of 10 percent. Effecting certain improvements in the system may allow this to be reduced to 5 percent for especially favorable transits. It is necessary to apply rather large corrections for extinction on transits at low elevation angles, corrections amounting to nearly one magnitude in the extreme. These corrections will themselves be uncertain by perhaps 10 percent. It thus appears that the limiting accuracy of photoelectric photometry will be in the range of $\pm$ 5 to 15 percent. For diffuse targets this amounts to uncertainties of $\pm$ 5 to 15 percent in albedo-surface area product.
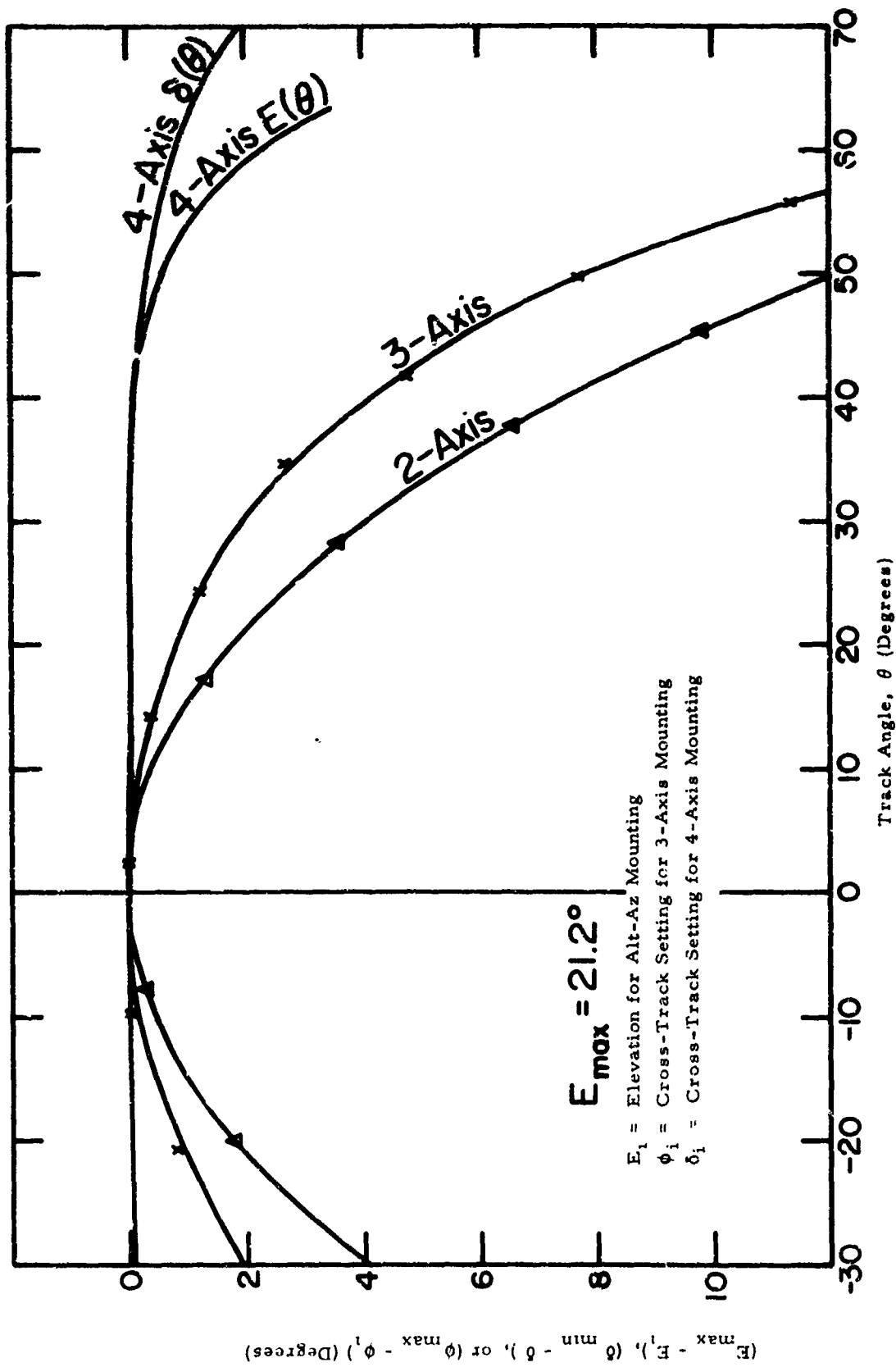
Figure 4. Comparison of Cross-Track Corrections for 2, 3, and 4-Axis Tracking Mounts for Low-Elevation Transit of 1000-km, Near-Circular Satellite

E_1 = Elevation for Alt-Az Mounting
ϕ_1 = Cross-Track Setting for 3-Axis Mounting
δ_1 = Cross-Track Setting for 4-Axis Mounting

$E_{max} = 21.2°$

4-Axis $\delta(\theta)$

4-Axis $E(\theta)$

3-Axis

2-Axis

Track Angle, θ (Degrees)

$(E_{max} - E_1)$, $(\delta_{min} - \delta_1)$, or $(\phi_{max} - \phi_1)$ (Degrees)

Photometric Data Collection at ARL

The earliest experiments in photoelectric photometry were carried out in April-May 1962 by CMSgt. E. T. Tyson and others of the USAF Avionics Laboratory with the author participating. Through mid-1963, E. M. Vallerie III, Capt. USAF, and Kissell continued observation, collecting many records of upper stage rockets. In October-November 1964, active data collection was resumed by Vanderburgh and Kissell. A total of 139 transits of 29 satellites; 18-USSR, 10-US, and 1 Canadian, were obtained from 1962 to 1 December 1964, when the tri-axial mounting was disassembled. In April 1965, a new 4-axis system was put into operation. A total of 90 space vehicles have now been recorded on over 400 transits. Typical light curves for vehicles exhibiting a combined specular and diffuse scattering, 1962 β a-2, and two satellites exhibiting an essentially diffuse reflection 1963-10B and 1962 $\beta \theta$ -2 are shown in Figures 6, 7, and 8. It should be emphasized that the ordinate heights are stellar magnitudes, i.e. log brightness.

Table 1. Calibration Accuracy of the ARL Photometer System

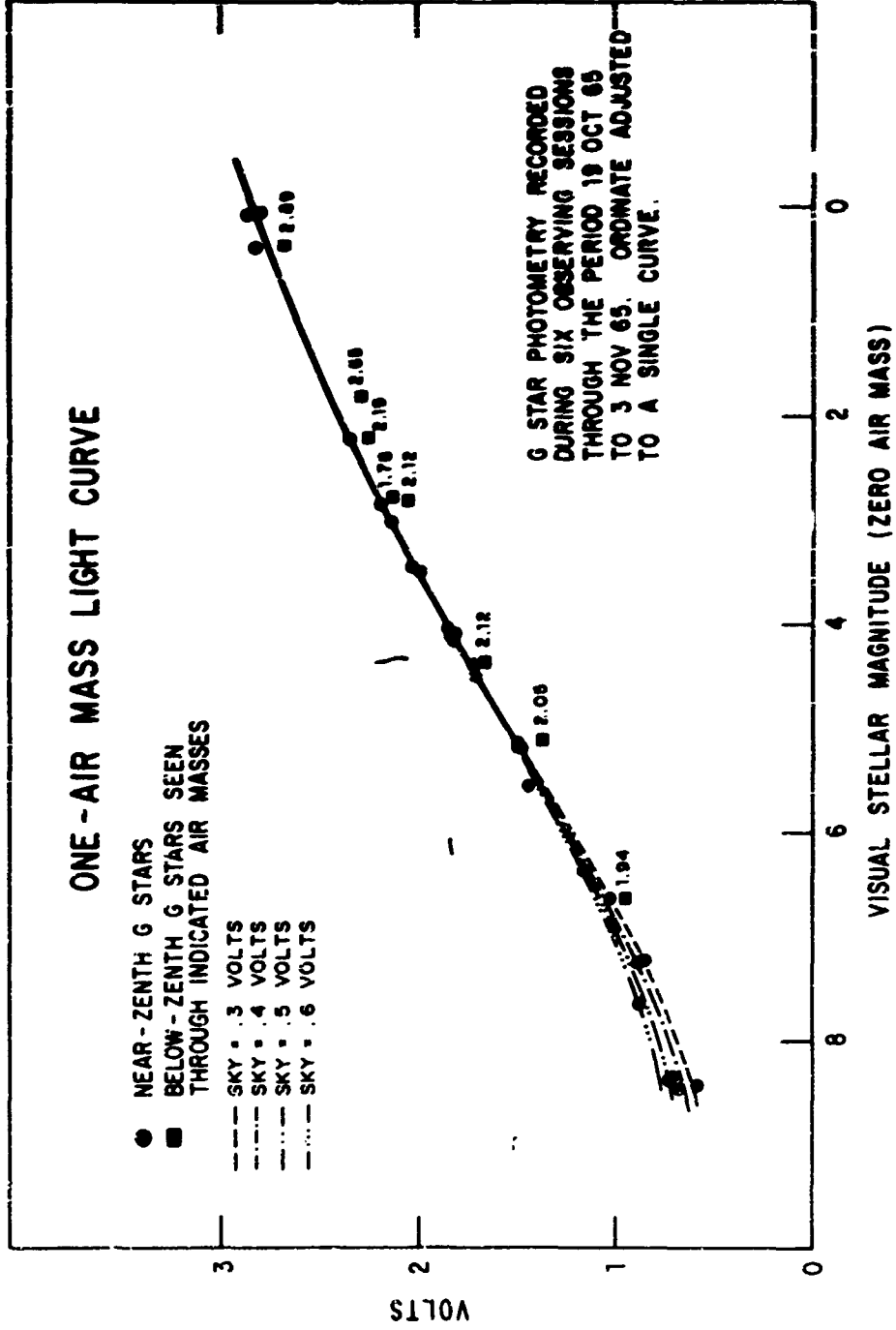| Mag. of	Watts received	Reciprocal Sensitivity	Accuracy	
			magnitude	percent
0 to + 3	10^{-9} to 0.6×10^{-10}	4.1 mag/volt	± 0.08	± 8
+ 3 to + 7	6×10^{-11} to 1.5×10^{-12}	3.4	± 0.07	± 7
+ 7 to + 10 (Dark sky)	1.5×10^{-12} to 10^{-13}	5.9	± 0.18	± 12
+ 7.2 to + 8.4 (Bright sky)	1.2×10^{-12} to 0.4×10^{-12}	7.7	± 0.15	± 15

Figure 5. Calibration Curve Obtained From Several Nights of Observation. Note the Effect of Increasing Twilight Sky Brightness on the Toe of the Curve, Reducing the Sensitivity at High Sky-Background Levels

These sample light curves illustrate several of the properties of photoelectric photometry. The first is the high signal-to-noise ratio of this technique. The second is the CW character where target data can be collected continuously except for accidental loss of target or deliberate drop off from target to sample the background sky or the dark current of the multiplier tube. The third is the inherent bistatic character of the technique most evidenced in Figure 8 but also noticeable in Figure 6. This results from the essentially-fixed direction of the sun-satellite vector in some inertial frame centered at the satellite and the continuous rotation of the observer-satellite vector. This generally results in large samplings of phase angle and results in relatively frequent occurrences of special conditions for the determination of the total angular momentum vector produced by passage of the angular momentum vector through the observer-satellite-sun plane near the condition of bisection of the observer-satellite-sun angle. This occurs in both Figure 6 and Figure 8. The fourth point is the relatively slow fall-off of signal with slant range. Because the illuminator is at a nearly constant distance, the luminous flux received varies with the inverse square of the slant range of the spacecraft rather than inverse fourth-power as in the radar or laser case.

Analysis of Brightness Measurements-Diffuse Cylinder

The fundamental relationships governing the dependence of space vehicle apparent brightness on size, slant range, phase angle, extinction, and albedo have long been established for simple spherical and cylindrical forms.[25,26] One application of these relationships to reduction of our experimental data has been by construction of a simple model for a diffuse cylindrical scatterer, without ends, which is free to nutate as the result of residual angular momentum about its longitudinal axis. The model, due to Ronald Dawson, Sqd. Ldr. RAF who worked on this problem while a guest investigator at ARL in 1963, is derived in detail in Reference 27. It establishes an expression for the luminous flux scattered in a particular direction from a diffuse cylinder whose longitudinal axis may be specified as a function of time t or an angular coordinate ψ while undergoing precession at a constant rate $\dot{\psi}$ about the total angular momentum vector. The longitudinal axis is presumed to be inclined at a constant angle ϵ_0 with the total angular momentum vector. Evidence is strong[28,29] that ϵ_0 must lie in the range of $\pi/2$ for freely-rotating, cylindrical bodies in orbit for a few days even if they initially were imparted a large angular momentum about the longitudinal axis. This model is illustrated in Figure 9 where OC represents the cylinder axis, $\overline{H}$ is the total angular momentum vector, and $\psi(t) = \dot{\psi} t$ is the precession coordinate.

To test this model, the data shown in Figure 8 were used. In the time interval near from 09:00:20^S to 09:01:25 UT the vehicle became increasingly backlit. Data at 09:00:41 UT was compared to the bright-
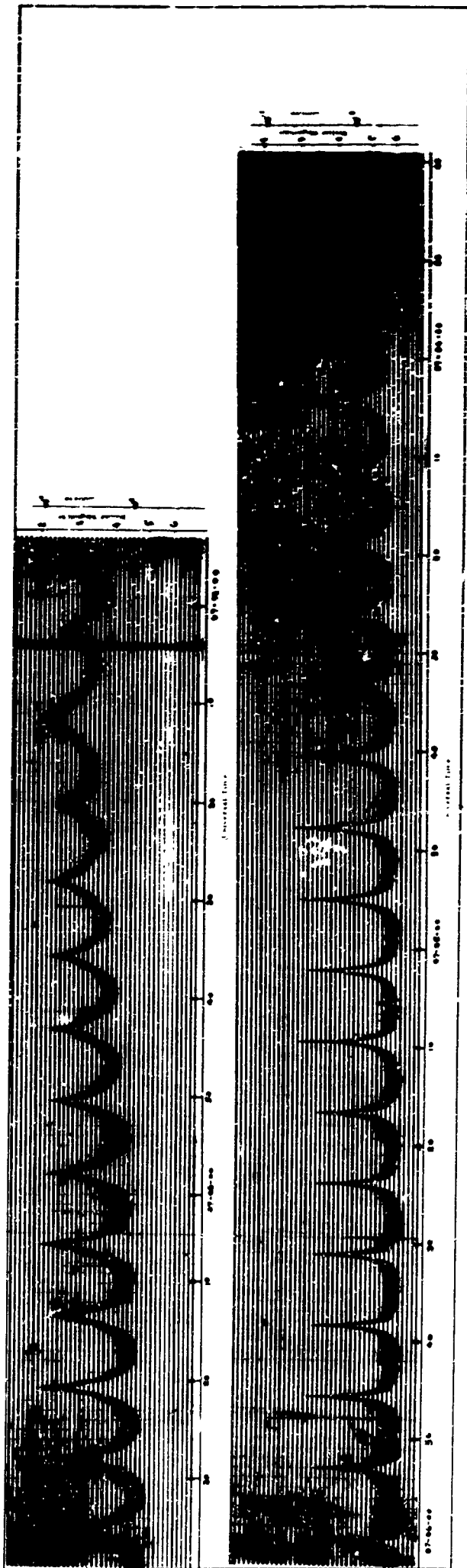
Figure 6. Light Curve of an Agena B Rocket Body, Space Object 426, 1962 Beta Alpha 2, on 15 June 1963, Revolution 3537. Ordinates in Stellar Magnitudes (1 Magnitude Equals Factor of 2.512 in Brightness) and in Photometric Units. Note the dc Component in the Interval From 07^h02^m and of 07^h03^m. The Specular Flash Brightness Falls off With the Inverse Square of the Distance and is Insensitive to Phase Angle (Reference 14)
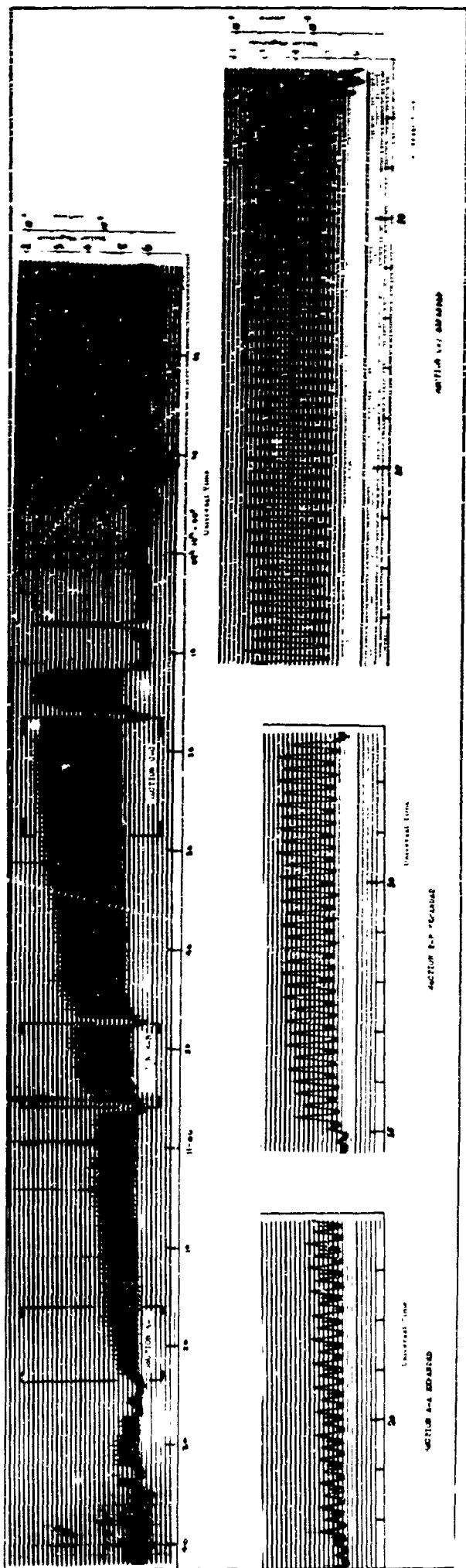
Figure 7. Light Curve of Cosmos 14 Rocket Body, Space Object 568, 1963-10B, on 28 April 1963. Note the smooth, regular variation at $09^h10^m20^s$ UT and the increasing specular contribution from the vehicle end surfaces at $09^h11^m20^s$ UT

ness variation predicted from the diffuse cylinder model for coning angles of 82 to 90 degrees. These data are plotted in Figure 10. The model seems reasonably satisfactory for this target if ϵ_0 is assigned a value of 89 degrees, i.e. almost a flat spin.

In order to carry out the above calculation, it was necessary to deduce the orientation of the precession axis. In this case, it was approximated by using the observed near-constancy of brightness at 08:59:15 UT. The precession axis was chosen to be the bisector of the solar phase angle.

For other light curves this precession axis could be derived from radar data or from the use of light curves taken on two or more successive transits or transits on successive days. The use of such data involves determining the instants of maximum dynamical variation in the brightness on different transits. This method has been discussed in detail in References 2 and 14 but has not yet been put to a test by the author. It requires careful calibration for extinction, the methods for which we have only recently devised.

With the rather satisfactory check of the diffuse-scattering cylinder model shown in Figure 10, it was considered worthwhile to deduce the product of the albedo and surface area[27] for this target. The results are given in the table below. The vehicle was found to have a brightness equivalent to that of a perfectly scattering, diffuse, white cylinder of cross section, i.e. the product of its length and diameter, of 109 square feet. Assuming different values of the albedo yield cross sections:

Albedo (percent)	Cross section
100	109
80	135
50	220
20	440

Analysis of Brightness Data - Specular Spheres

In contrast with the tumbling vehicles in the class of upper stage rocket bodies which exhibit light curves with strongly periodic variations, other targets, notably USSR payloads of the presumably recoverable type (they decay prematurely into the atmosphere after 120-130 orbits) exhibit no periodic changes in brightness. They, in fact, exhibit little brightness fluctuation at all. Good data were obtained on three such targets, Space Objects 1382, 1404, and 1421, Cosmos 67, 68, and 69 respectively. Data on one transit of 1382 (in a 51° inclination orbit), four transits of 1404 and two transits of 1421 (in 65° inclination orbits) have been examined on a simple spherical model based on
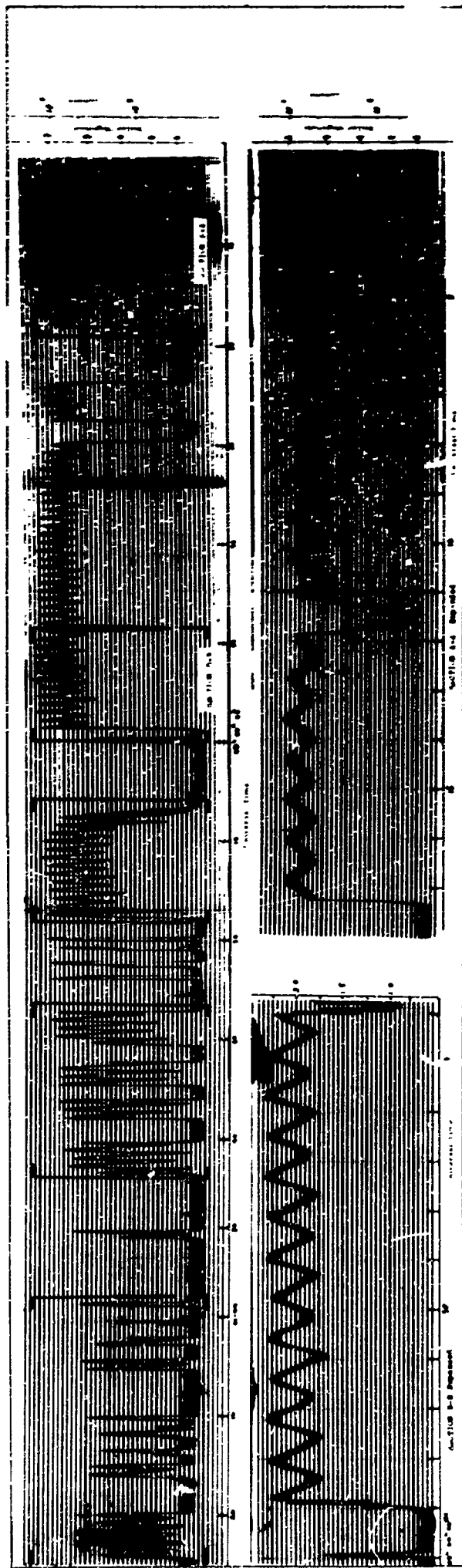
Figure 8. Light Curve of Cosmos 11 Rocket Body, Space Object 442, 1962 Beta-Theta 2, on Revolution 3051, 7 May 1963. Note the quasi-steady character at $08^h59^m10^s$ UT and the large assymetric variation under backlit conditions at $09^h00^m40^s$

an analogy with the Vostok capsules displayed at the 1965 Paris Air Show.[30]

If the vehicle shape were spherical, one can compute the variation of vehicle brightness with the phase angle of solar illumination for two limiting cases, the diffuse sphere and the specular sphere, independent of the orientation of the presumably stabilized body.

Individual calibration curves of photometer output voltage versus stellar magnitude were developed for each transit taking into account, as much as possible, the extinction existing on each of the seven nights. A sample computation is given in Table II, indicating the manner in which selected points on the light curve were treated to obtain first the apparent magnitude corrected for extinction and then an absolute magnitude (corrected for phase angle in the case of the diffuse sphere), i.e. the magnitude which the vehicle would have had at a standard 1000 km slant range.

A composite plot of the data collected on 1382, 1404, and 1421 is given in Figure 11 where the comparison of data for a specular sphere model is shown in Figure 11a and for a diffuse sphere model is shown in Figure 11b. These figures represent the intrinsic brightness as a function of time which the vehicles would have exhibited 1.) if they adhered to the models, 2.) if they had been observed at 1000 km slant range, and 3.) if they had been observed with a constant phase angle of 90 degrees. It is observed that the specular sphere model leads to data of greater internal consistency on a given transit and of greater external consistency compared between transits of the same vehicle and between transits of different vehicles.

It is credible that the brightness of all these payloads is due to scattering of sunlight from a specular ball-like configuration with modulations due to surface detail. From the mean absolute magnitude of + 4.7 + 0.3 we can arrive at the radius of the ball from the relationship[31]

$$M = + 4.96 - 5.0 \log b$$

where b is the radius of the spherical surface in meters, and M is the absolute magnitude determined at 1000 km standard distance for a sphere of one meter radius and a reflectivity of 0.8. We thus obtain

$$b = 10^{-0.2 (M - 4.96)}$$

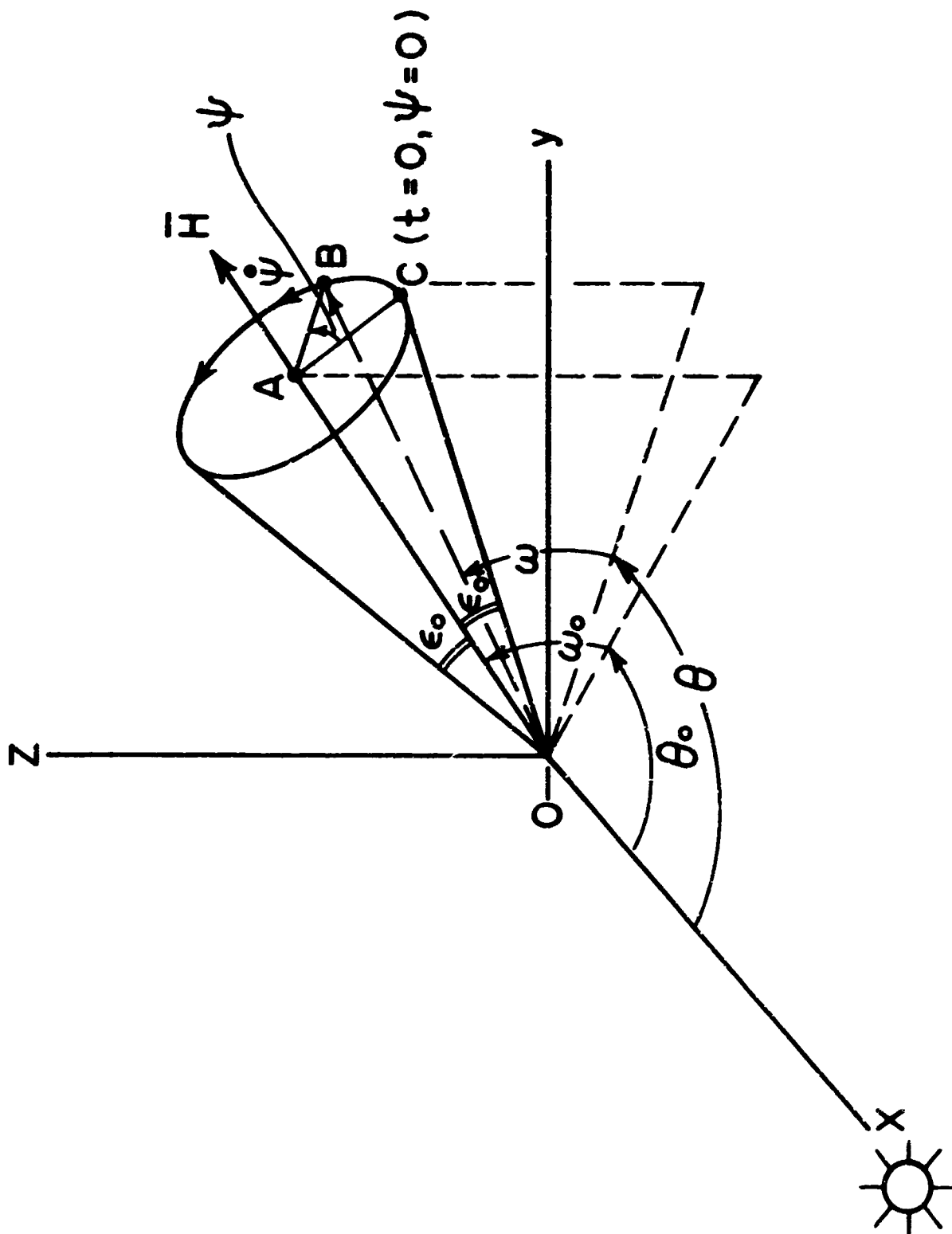For Cosmos 67, 68, and 69

Figure 9.   Time-Dependent Coordinates of a Diffusely-Scattering Cylinder

Table II. Reduction of Photometric Data to Absolute Magnitude (1000-km slant range) for Space Object 1382, Cosmos 67, on 28 May 1965.

| Point	UT	dark .20v sky .93v Volts	Alt	Az	Slant Range (Km)	Phase Angle	Apparent Mag - Zero Airmass	Specular Sphere Abs Mag (1000 Km)	Diffuse Sphere Abs Mag 90° Phase
1	0205:08	1.45	15.2	258.0	811	119	5.08	5.54	4.24
2	:17.5	1.45	16.2	253.2	776	117	5.16	5.71	4.51
3	:28	1.70	17.4	247.7	748	115	4.28	4.91	3.96
4	:34.5	1.70	17.8	244.2	733	113	4.30	4.98	3.97
5	:40.5	1.77	18.2	240.7	722	111	4.05	4.76	3.83
6	:48	1.80	18.6	236.0	710	108	3.97	4.71	3.88
7	:56.5	1.95	18.9	230.7	703	105	3.46	4.22	3.52
8	0206:06.5	1.80	19.1	224.0	702	101	3.98	4.74	4.1?
9	:15.5	1.80	18.9	218.2	706	98	3.98	4.73	4.26
10	:22.5	1.95	18.7	214.2	714	96	3.46	4.19	3.81
11	:26.5	1.93	18.5	211.7	720	94	3.52	4.23	3.92
12	:33	1.85	18.1	207.5	733	92	3.78	4.46	4.21
13	:51	1.68	16.5	197.5	784	86	4.30	4.83	4.75
14	:59	1.60	15.7	193.7	812	84	4.54	4.99	4.97
15	0207:07.5	1.58	14.9	190.2	840	82	4.55	4.93	4.95
16	:14	1.53	14.1	187.3	870	81	4.67	4.97	5.05
17	:21	1.28	13.4	184.5	900	79	Begin shadow entry		
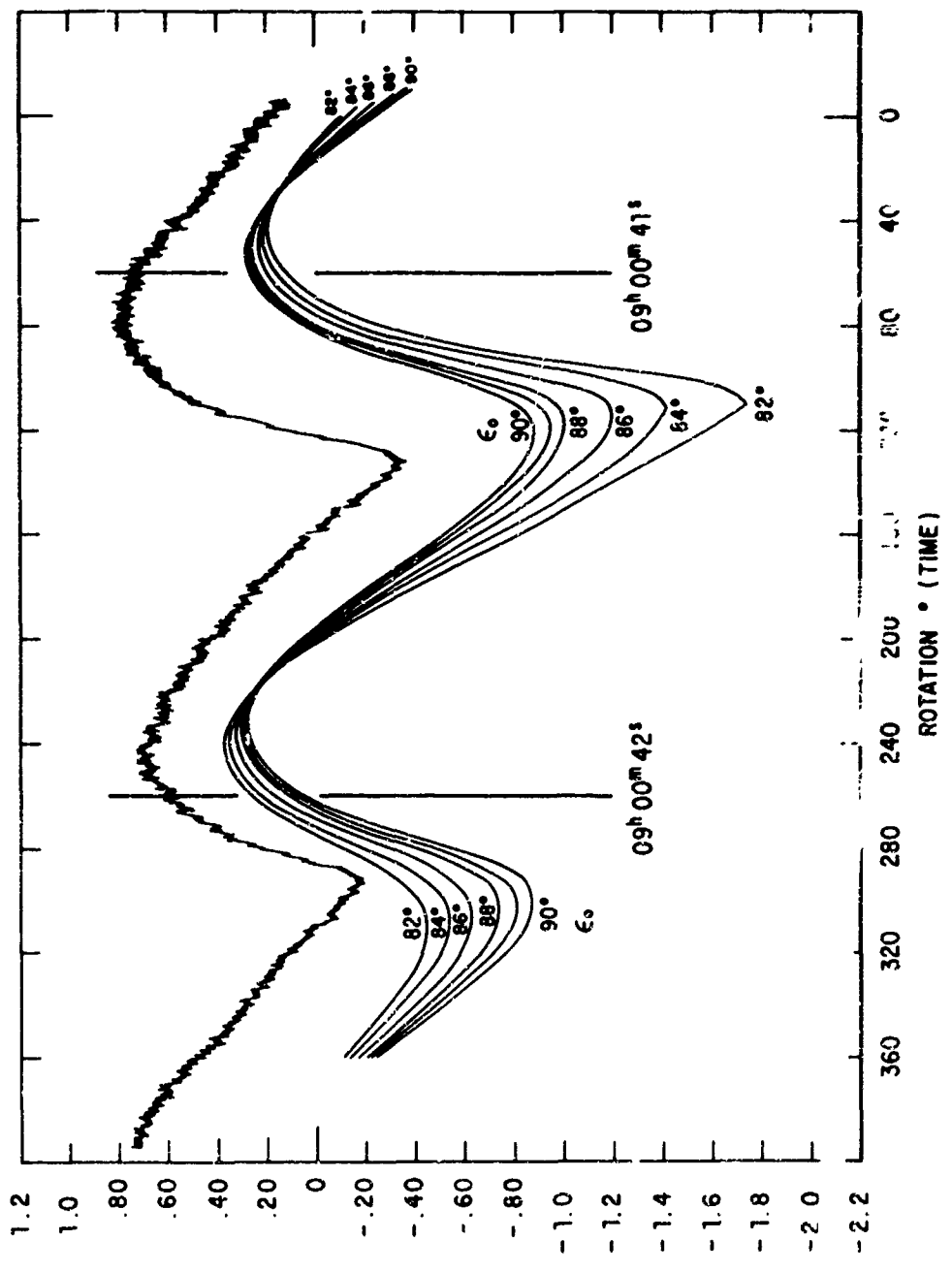
Figure 10. Ordinates are Log of Brightness for the Predicted Curve and direct Visacorder Output (uncorrected for non-linearity) for the Actual Photometric Record. Precession axis orientation assumed to be determined by a nearly invariant brightness at 08ʰ 00ᵐ 58 UT. Longitudinal axis of cylinder assumed to lie at angles of 82, 84, 86, 88, 89, and 90 degrees to precession axis

$$b = 1.1 \text{ meters} \pm 0.1$$

This is in accord with the one-meter radius given for Vostok in Reference 30.

Conclusions and Potential Future Applications

A fertile and unexploited source of signature data on orbiting space-craft exists in optical photometry. The use of telescopes of modest aperture (12-36 inches) established on special multi-axis mountings with hand control or simple servo control will allow collection of bi-static CW signature data of high quality with a minimum of expenditure. Based on field experience with a 24-inch system costing $40K, a 36-inch instrument could be established at a cost of $100-150K at any location in the world, operated by a 3-4 man crew, and provide signatures on targets out to 35,000 km on a routine basis. If the optics are of high quality, the instrument can be used for simultaneous collection of resolved images on many targets out to 500 km slant range

The initial work at ARL has shown that careful calibration of the photometric system will allow not only the distinction between surface finishes of targets, and the dynamical motions of targets but also estimates of the dimensions of targets based on the optical model selected. While much detailed work remains to be done to determine both the full power of this technique and its limitations, it is believed that the program at ARL has firmly established the feasibility of the optical photometric approach to ground identification of satellites. The greatest effectiveness of this signature source will be its combination with radar and/ or with direct imaging so that the advantages of each can be exploited.

No application of this research has yet been made in terms of its regular usage or its adoption in an operational system. However several USAF elements are studying the results of this work and its possible impact on problems now being approached by other techniques. ARL has provided several agencies with special data for their exploitation. These include Electronic System Division for whom selected satellites have been calibrated in brightness at ranges of 2000 to 5500 km, Air Defense Command for whom the tumble rates are being measured for all observed bodies having a recognizable periodicity in the light curves, and NASA for whom the received times are being measured of light flashes from the xenon discharge lamps on board the geodetic satellites. An attempt is being made to relate the amplitude of these beacon flashes to the stability of the GEOS vehicle which employs gravity gradient stabilization, but whose attitude
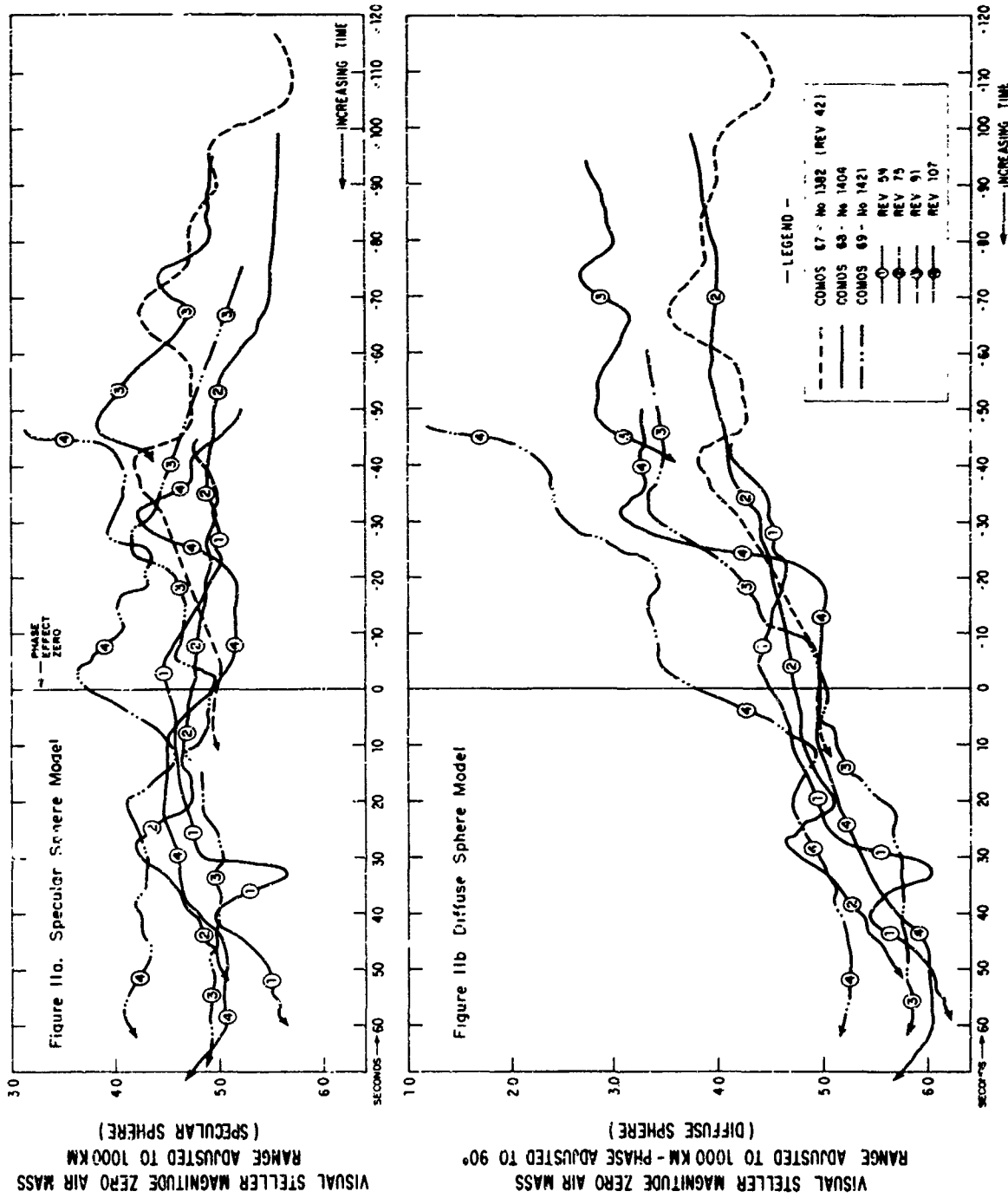
Figure 11. Comparison of Photometric Data from Cosmos 67, 68, and 69 at Slant Range of 1000 km and Constant Phase Angle of 90 Degrees for Diffuse and Specular Sphere Models

sensors have malfunctioned.

At the request of the RCA Defense Systems Division, a cooperative program has been carried out in the simultaneous observation of spacecraft by optical photometry from Ohio and by radar scattering from Moorestown, N. J. Calibrated light curves have been provided to various AFSC elements and to MITRE Corporation for their analysis in terms of the properties of vehicles.

References

1. V. P. Tsesevich, "On Brightness Variations of Artificial Satellites," Trans. of IAU, X, (1958), p. 722.

2. V. M. Grigorevskij and U. Gyunttsel-Ligner, "Optical Observation of Artificial Earth Satellites," NASA Technical Translation F-11, February 1961, pp. 1-18.

3. M. Melin, "The Tumbling of 1958 $\delta 1$," Sky & Telescope XVIII, No. 2, (Dec 1958), pp. 82-3.

4. M. Melin, "More About Project Rotor," Sky & Telescope XVIII, No. 3, (Jan 1959), pp. 145-6.

5. J. G. Moore, "Photometric Observations of Satellite 1958 $\delta 1$," Sky & Telescope XVIII, No. 2, p. 83.

6. S. V. Venkateswaren, J. G. Moore, and A. J. Krueger, "Determination of the Vertical Distribution of Ozone by Satellite Photometry," J. Geo. Res., 66, (June 1961), pp. 1751-71.

7. F. Link, "Sur les problemes de l'optique atmospherique a bord des satellites artificiels," Paper 6.11, COSPAR Symposium of Florence, May 1964.

8. F. Link, L. Neuzil and I. Zacharov, "Photometric Photoelectrique des Eclipses de l'Echo 2," Space Research V, North-Holland Publ. Co., Amsterdam (1965) pp. 826-827.

9. "Telstar Spin Axis Studies," Sky & Telescope XXV, No. 3 (March 1963), p. 143.

10. J. S. Courtney-Pratt, D. W. Hill, J. W. McLaughlin, and J. H. Hett, "Optical Measurements on Telstar," A. J., 68, No. 2, (March 1963), p. 70.

11. W. C. Jakes, Jr., "Participation of the Holmdale Station in the Telstar Project," NASA SPL 32, Vol. 2, (June 1963).

12. K. E. Kissell, "Requirements for a 4-Axis Tracking Mount for Space Vehicle Photometry," Paper WG 1.7, COSPAR Symposium of Florence, May 1964. ARL TR 65-260.

13. K. E. Kissell and E. T. Tyson, "Rapid-Response Photometry of Satellites," A. J., 69, No. 8, p. 547.

14. E. M. Vallerie III, "Investigation of Photometric Data Received from an Artificial Earth Satellite," Thesis, AFIT, August 1963.

15. R. H. Emmons, "Indicated Specular Degredation Rate for Alumnized Mylar Surfaces in Near-Earth Orbit from Recent Photometric Observations of the Echo I Satellite," A. J. 69, No. 8, p. 540.

16. "Program Definition Study for Evaluating Satellite Materials by Ground-Based Photometry," Goodyear Aerospace Corp. Rpt GER 12204, August 1965.

17. R. J. Davis, R. C. Wells, and F. L. Whipple, "On Determining the Orientation of a Cylindrical Artificial Earth Satellite," Astronomica Acta, 3, (1957), p. 231.

18. R. H. Giese, "Altitude Determination from Specular and Diffuse Reflection by Artificial Satellites," SAO Research in Space Science Report No. 127, (1963).

19. R. H. Wilson, Jr., "Optical & Electronic Tracking," Geophysical Monograph No. 4, A. G. U. (1959), pp. 67-78.

20. L. Binnendijk, "Properties of Double Stars," Univ. of Penn. Press, Philadelphia (1960), pp. 198-257.

21. H. L. Johnson and W. W. Morgan, "Fundamental Stellar Photometry for Standards of Spectral Type on the Revised System of the Yerkes Spectral Atlas," Ap. J. 117, 3, pp. 313-331 (1953).

22. O. J. Eggen, "Colors, Luminosities, and Motions of the Nearer G-Type Stars," Astron. J. 69, 8, pp. 570-609, (1964).

23. B. Iriarte, H. L. Johnson, R. I. Mitchell, and W. K. Wisniewski, "Five-Color Photometry of Bright Stars," Sky & Telescope XXX, No. 1, pp. 21-31.

24. L. Binnendijk, p. 239.

25. J. B. Zirker, F. L. Whipple and R. J. Davis, "Time Available for the Optical Observation of an Earth Satellite," Scientific Uses of Earth Satellites, Univ. of Mich. Press, Ann Arbor, (1956), pp. 23-28.

26. G. J. Stiles, "Prediction of the Apparent Magnitude of Distant Missiles in Sunlight," Ballistic Research Labs. MR-1008, Aberdeen Proving Ground, Md., June 1956.

27. K. E. Kissell and R. C. Vanderburgh, "Photoelectric Photo-
metry - A Potential Source for Satellite Signatures," First
Symposium on Ground Identification of Satellites (1965).

28. R. J. Naumann, "Directional Dependence of Counting Rates from
Explorer IV," NASA TR R-168, December, 1963.

29. R. J. Naumann, "Observed Torque-Producing Forces Acting on
Satellites," NASA TR R-183, December 1963.

30. "A Close Look at Vostok," Flight International, 22 July 1965,
pp. 127-129.

31. J. W. Slowey, "A Chart for Finding a Satellite's Distance and
Elevation," SAO Bulletin for Visual Observers of Satellites, No. 8,
March, 1958, p. 7.

Dr. Morris E. Fine is a Walter P. Murphy Professor of Materials Science at Northwestern University, where he was instrumental in setting up the ARPA-Interdisciplinary Laboratory Materials Research Center Program. He was chairman of this program until June 1964. During World War II, Dr. Fine was with the Manhattan Project at the University of Chicago and Los Alamos. Prior to coming to Northwestern University, he worked at the Bell Telephone Laboratories. Dr. Fine received his Ph. D. in Physical metallurgy from the University of Minnesota in 1942. He is author or co-author of over 60 technical papers, has recently completed a book on phase transformations in condensed systems, and holds two patents.

Precipitation in Ceramics

By
Morris E. Fine
Department of Materials Science
Northwestern University

In heat treated hardened steels discovered some 3000 years ago by the Hittites, the excellent mechanical properties are due to very fine iron carbide particles dispersed in a matrix of almost pure iron. Such hardened steels are a cornerstone of our modern technology being used in such parts as plowshares and Minuteman rocket motor cases.

Precipitation hardening in aluminum-base copper alloy was discovered in 1905 by A. Wilm in Germany. Like the Hittites, Wilm did not know why his alloy was hard. The heat treatment consisted of an anneal at 925°F followed by quenching into water. The alloy was then soft but it became strong on aging at room temperature. After Merica, in 1919, correctly attributed the age hardening to precipitation or formation of copper-rich particles in the aluminum base matrix, hundreds of commercial alloys based on precipitation hardening were developed. Merica's contribution was one of the most important in the annals of metallurgy. Besides the aluminum alloys such alloys as Rene 41, Maraging steels, and precipitation hardened stainless steels, all used extensively in aerospace applications, are hardened by dispersed solid precipitate particles.

Bones in vertabrate animals are dispersion hardened. Hard small calcium phosphate crystals are dispersed in a soft protein matrix. The evolutionary success of vertabrates is attributed in part to their strong bones.

Strangely, the possibilities of precipitation hardening has hardly been exploited in crystalline ceramics. To my knowledge only one example exists. During World War II, in Germany, jewel bearings were made of the mineral spinel ($MgAl_2O_4$) dispersion hardened by alumina (Al_2O_3) rich precipitates[1]. For these bearings, synthetic spinel crystals were made with excess Al_2O_3 and rapidly cooled from the growing temperature maintaining the alumina in solution. Such crystals were easily ground to form jewel bearings. When heated to and aged at 1000°C, the Al_2O_3 rich precipitates formed. These hardened the bearings to roughly the abrasion resistant qualities of sapphire (Al_2O_3). The advantage of the spinel bearings over sapphire is that less diamond bort is required in the grinding operation because they are ground in the soft condition.

At Northwestern we had been engaged for a number of years in a fundamental study to understand better the important factors involved in precipitation hardening in metals. The currently accepted theory of the strengthening mechanism derives significantly from work done at

Northwestern. We also helped elucidate the course of the precipitate reactions. This knowledge, I am sure, is proving helpful to people engaged in development of new alloys and improving old alloys.

Several years ago it was decided to undertake a study of precipitation in ceramics because it appeared to be a good field for exploitation from the fundamental and from the applications point of view. Alloying and heat treatment of ceramic oxides is an area whose technological importance is bound to increase over the ensuing years. The purpose of my talk is to convince you that this will be true.

Our first work was with NaCl, ordinary table salt, hardened by KCl rich precipitates[2]. We were able to increase the fracture strength of ordinary table salt by a factor of 10. In pure table salt, fracture takes place by cleavage leaving very smooth and splendant cleavage faces. In the hardened crystals, the cleavage surface is very rough as shown in Fig. 1. The precipitates interfere with the cleavage process and resist propagation of cracks thereby increasing the fracture strength. While strong table salt may have little use - we selected the system because we thought the samples would be easy to prepare - this research was important for establishing a basic principle.

The next research was with magnesium oxide (MgO) alloyed or doped with iron[3]. MgO has the same crystal structure as NaCl and its melting point is $5100°F$ ($2800°C$). The iron was diffused into MgO at elevated temperatures, $1400°C$.

In heat treating oxide ceramics, in contrast to metals, one must control the oxygen pressure as well as the temperature. This gives another variable which may be used to manipulate the material to give a desired structure. Iron exists in two valence states, di-valent iron Fe^{++}, as in FeO (wüstite) and tri-valent iron, Fe^{+++}, as in Fe_2O_3 (hematite). With Fe^{++} present, MgO and FeO form a complete solid solution called magnesiowüstite; the two substances are completely soluble in each other like water and alcohol. On the other hand, Fe^{+++} is only partially soluble in MgO. In a Mg-Fe-O mixture, the ratio of Fe^{+++} to Fe^{++} depends on the pressure of oxygen. In air, where the pressure of oxygen is roughly $1/4$ of an atmosphere, at $1400°C$ about 30% of the iron is Fe^{++} and 70% Fe^{+++}.

As shown in Fig. 2, at $1400°C$ in air MgO will dissolve Fe up to Fe/(Fe + Mg) equal to 20%. By rapidly cooling to room temperature from $1400°C$ the Fe is maintained in solution. As previously mentioned, 70% of the Fe is in the Fe^{+++} state. This solution is supersaturated, and if the (Mg, Fe)O is heated to some temperature such as $800°C$, the Fe^{+++} precipitates as magnesioferrite ($MgFe_2O_4$). Fig. 3 is an electron microscope picture of magnesioferrite precipitates in MgO. In this sample, the ratio of Fe to (Fe + Mg) was one percent. It was heated

for 4 hrs. at 800°C. The magnification in the figure is 60,000 times. The precipitates appear as squares but in three dimensions they are octahedra. Their size in Fig. 3 is on the average 1.5×10^{-6} cm. or a half millionth of an inch across the diagonal. There are 1×10^{17} particles per cubic inch; that is, a hundred thousand trillion particles per cubic inch.

On continued aging, the precipitate particles coarsen by competitive growth; the bigger particles grow at the expense of the smaller particles. Fig. 4 shows the structure of 4.25% Fe/(Fe + Mg) aged for 27 hrs. at 1000°C. In this figure taken with an ordinary light microscope, the magnification is only 750 times and the average precipitate diagonal is 1.2×10^{-4} cm. or 80 times bigger than in Fig. 4. In this material there are 10^{12} particles per cubic inch; that is, a trillion particles per cubic inch.

The $MgFe_2O_4$ precipitates impart two important properties to the ceramic. First, they make MgO stronger and second they make the ceramic ferrimagnetic. We have studied and are studying both the strength and the magnetic properties. Both have important possibilities with respect to applications. The strength properties will be discussed first.

One of the ways in which metals are strengthened is by putting a second metal into solution in the first metal. This is widely used. For example, zinc is dissolved into copper to form brass; brass is much stronger than either copper or zinc. As shown in Fig. 5, MgO may be strengthened by dissolving Fe^{+++} into it. The strength of a pure MgO single crystal is 11,000 lbs./in.^{2} (8 Kg/mm^2). Adding 3% Fe^{+++} at 1400°C and rapidly cooling to room temperature to maintain the Fe^{+++} in solution increases the strength by a factor of 6 to 66,000 lbs./in.^{2} (47 Kg/mm^2). Adding Fe^{++}, Fig. 5, does not increase the strength. In ionic crystals to increase strength the alloying element must have a different valence from that of the ion for which it substitutes, Mg^{++} in this case.

Further strengthening is obtained if the quenched or solution treated Mg-Fe-O ceramic is aged at 800 or 900°C, Fig. 6. A strength of 42,000 lbs./in.^{2} (30 Kg/mm^2) is obtained in the 1.35% Fe magnesia ceramic with a short time aging at 800°C. The Fe^{+++} has now precipitated as $MgFe_2O_4$ and the strengthening over pure MgO is entirely due to this precipitate. The strength decreases with further aging due to coarsening of the precipitate particles.

The mechanical property study of this system is being extended to fracture studies. From our work with NaCl-KCl[2], we suspect that the best enhancement of fracture strength will occur with a rather coarse precipitate size and not at the maximum yield stress in single crystals.

Referring back to Fig. 4, there are cracks observed around a hardness indentation. These cracks appear to avoid the pre pitate particles. The $MgFe_2O_4$ precipitates have a different cleavage lane (octahedral) than MgO (cubic) and thus if the particles are lar enough and closely enough spaced, the brittle cleavage behavior of Mg y be changed.

This same principle, interference of the fract u process by precipitates, is being tested in another ceramic syste , sapphire (Al_2O_3) alloyed with titanium. This is the basic system by wl ch star sapphire gems are formed. Figure 7 shows needle shaped prec ni ates in a sapphire crystal doped with 1/4% Ti. This crystal own in our laboratory was aged at 1550°C. The precipitates are repo d to he a solid solution of Al_2O_3 and Ti_2O_3[6]. In some samples with ripitates, we have qualitatively measured a fracture stress about that in ure sapphire crystals.

Many possible defense and commercial applicatior f r stronger ceramics come to mind. While one would like to use a oxide as a structural material at elevated temperatures in an ox lizing atmosphere where metals rapidly corrode, the ease with which cera nics fracture mitigates against this use. Defense systems as well as power generating equipment are continuously being designed to oper te at increasingly higher temperatures. It is certain that ceramics will lay a much more important role in such systems in the future. What e ave learned here is important with respect to use of these materials, bu the principles are even more important because they show a way to impr e the mechanical properties of ceramics.

Finally, the magnetic properties of Mg-Fe-O alloy c amics will be discussed.

The magnesioferrite precipitate which forms in Mg-Fe i is a ferrimagnetic oxide belonging to the important class of materia s known as ferrites. They are widely used commercially for their rag tic properties. Applications include high frequency transforr.ers memory cores for computers, and coatings on magnetic tape.

A study of the static magnetic properties of the magne ferrite precipitates has just been completed[6]. Some of the result ll be given here. The magnetic properties are an excellent way studying the precipitation process in this system.

Curves of magnetization versus applied field are pres nt in Fig. 8 for 4 hrs. of aging at 800°C. Data are shown for three tempera-tures, ambient (25°C), liquid nitrogen (-196°C), and liquid he am (-269°C). None of the curves show the usual hysteresis seen in magnetic materials. This is because of the small particle size for this eat-

ment; the particles are superparamagnetic. The alignment of the particles by the applied magnetic field is opposed by thermal disordering. Note that the saturation magnetization increases on cooling. The particles precipitated at 800°C are not ferrimagnetic above 220°C, their Curie temperature. The Curie temperature here depends on the aging temperature; it is 250°C for 700°C aging. The slope of the magnetization curve at -269°C at high fields is due to Fe^{++} dissolved in the MgO matrix. Measuring the slope is an excellent way to determine dissolved iron. For 1% Fe reacted at 1400°C, 0.3% Fe as Fe^{++} will stays in solution after precipitation.

Referring to Fig. 9 the saturation magnetization, determined from curves like that in Fig. 8 for -196°C, quickly reaches its maximum value after a few minutes of aging and then remains constant. The Fe^{+++} completely precipitates as $MgFe_2O_4$ very quickly. During the subsequent aging some particles coarsen by competitive growth, some disappear. Thus the number of particles per unit volume, Fig. 10, decreases with aging time.

Note that the number and size of particles may be controlled beautifully by controlling the Fe^{+++} content, the aging time and aging temperature.

Thus, by the precipitation technique one can obtain extremely copious fine magnetic ferrite particles distributed in an insulating matrix. This is an interesting and new type of magnetic material. One possible application which comes to mind is as a memory for a computer. If one could couple to the particles so that each particle stores by the direction of its magnetic moment a bit of information, then one could store something like 10^{12} bits of information per in.^{3} in the sample in Fig. 4. The 10^{15} bits of information in the Library of Congress could then be stored in a thousand in.^{3} of material or a cube 10 in. on a side. Another application is radar absorption. A body coated with the material is made less visible to radar. This application is being actively pursued in another laboratory.

In conclusion, the results to date reinforce the original idea that precipitation studies in ceramics, that is, studies of alloying and heat treatment of ceramics, are important from both the points of view of basic research and applications.

106

List of References

1. W. F. Eppeler, FLAT Rept. No. 1038, 1947, ASTIA ATI 13 284.

2. R. G. Wolfson, Ph.D. Thesis, Northwestern University, 1965. Thesis Advisor, M. E. Fine.

   R. G. Wolfson, W Kobes, and M. E. Fine, Jour. Appl. Phys. $\underline{37}$, Feb. (1966).

3. G. W. Groves and M. E. Fine, Jour. Appl. Phys. $\underline{35}$, 3587 (1964).

4. B. Phillips, S. Somiya, and A. Muan, Jour. Am. Ceram. Soc. $\underline{44}$, 167 (1961).

5. E. W. White, Ph.D. Thesis, Pennsylvania State University, 1965. Thesis Advisor, R. Roy.

6. G. Wirtz, Ph.D. Thesis, Northwestern University, 1966. Thesis Advisor, M. E. Fine.
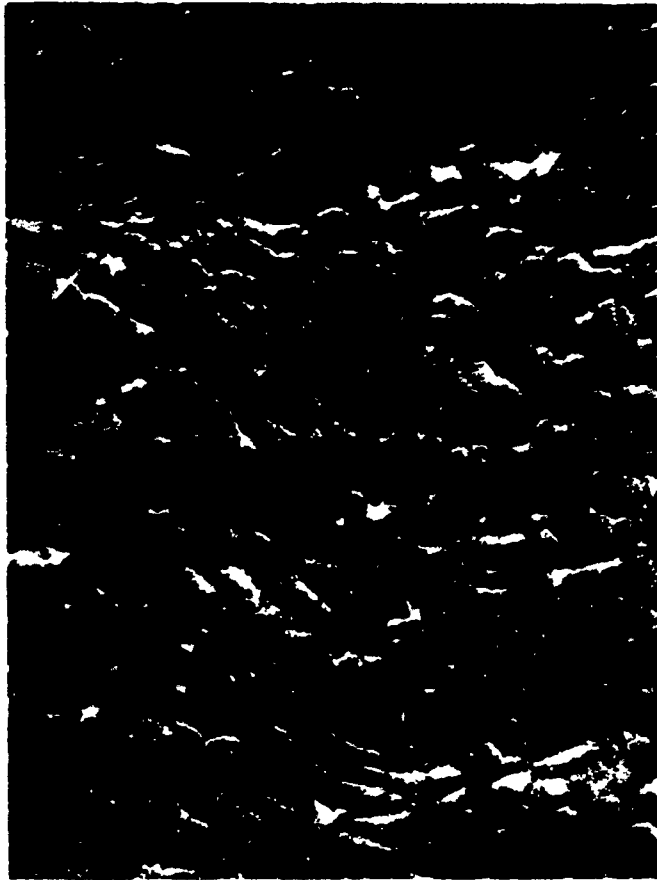
Figure 1. Replica of Fracture Surface of Equimolar
NaCl-KCl Crystal Aged at 350°C. The surface is
quite rough with elongated features roughly $0.1 \times 1\mu$
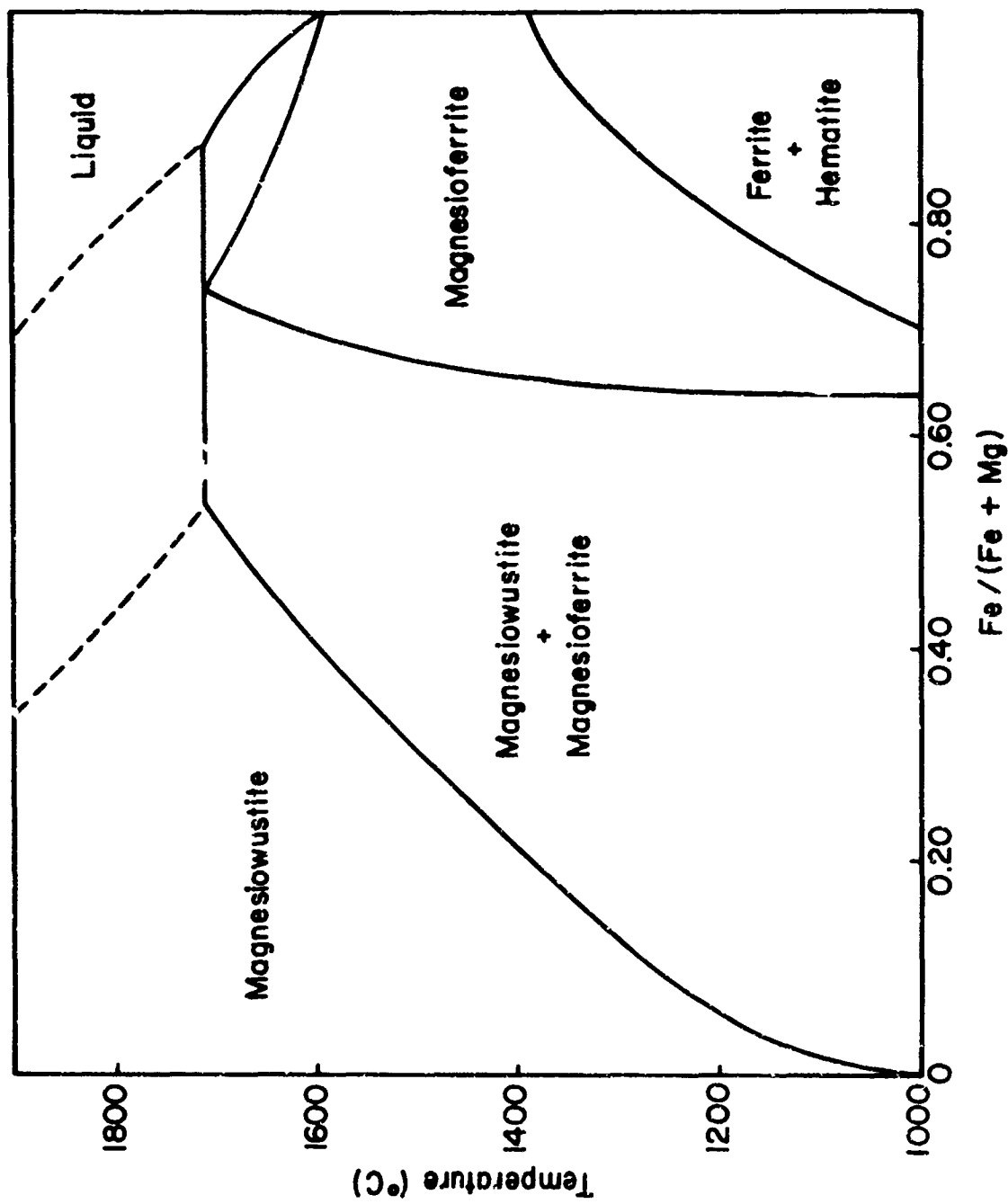
Figure 2. Phase Boundaries in the System Mg-Fe-0 in Air After Phillips et al
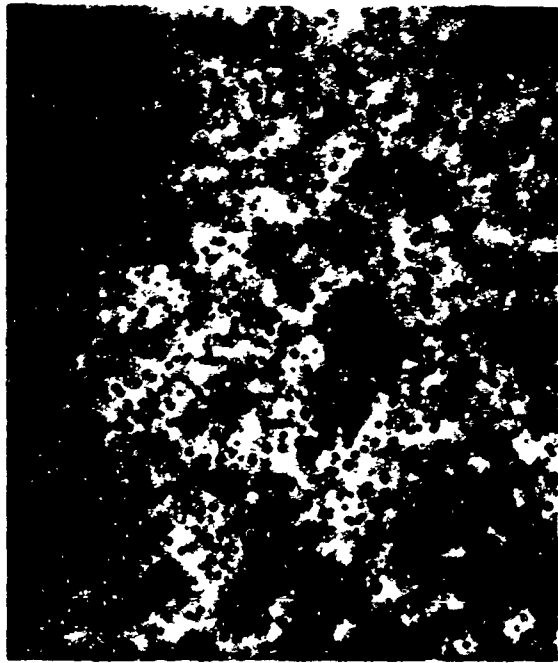
Figure 3. Magnesioferrite Precipitates in an Mg-Fe-0 Alloy Crystal
Containing Fe/Fe + Mg) = 1%. This was homogenized in air at 1400°C,
cooled in air to room temperature, then aged 4 hrs at 800°C. The
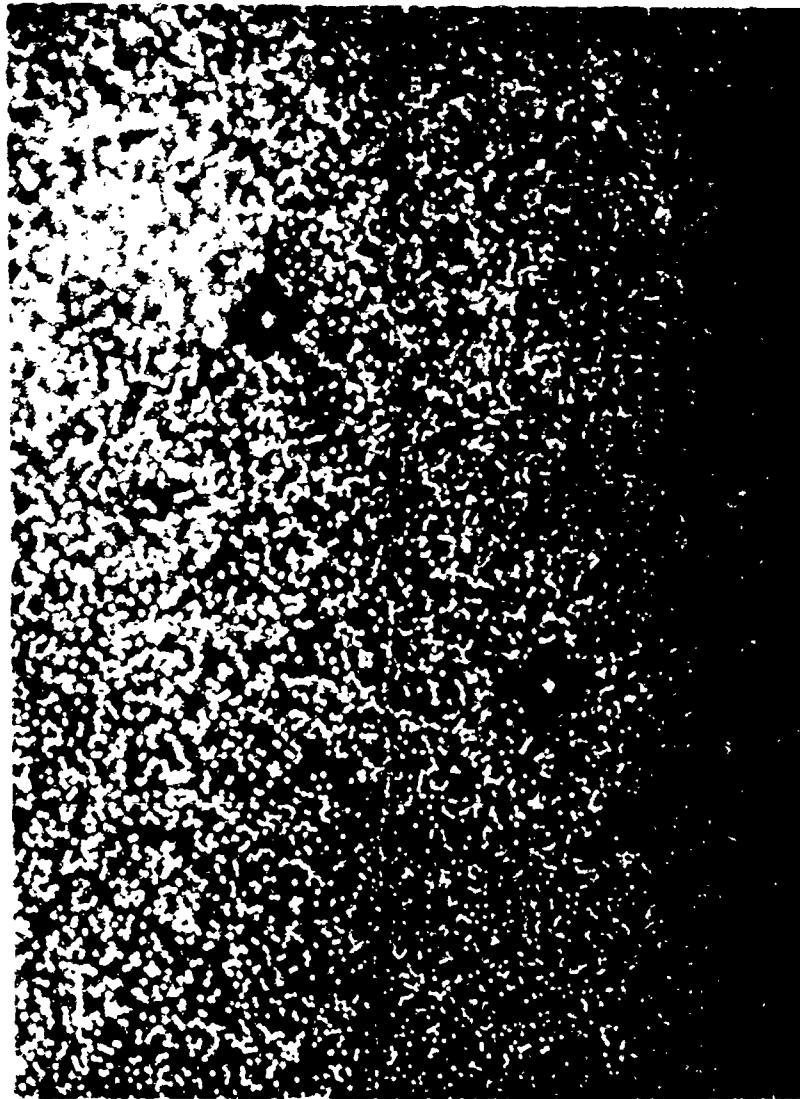matrix phase is magnesiowüstite. Magnification = 60,000 times

Figure 4. Magnesioferrite 1 ·ecipitates in 4.25% Fe/(Fe + Mg) Crystal Aged 27 hrs at 1000°C in Air. Magnification = 750 times. As in Figure 3, the sample was homogenized in air at 1400°C and air cooled. Note hardness indent and cracks around hardness indent
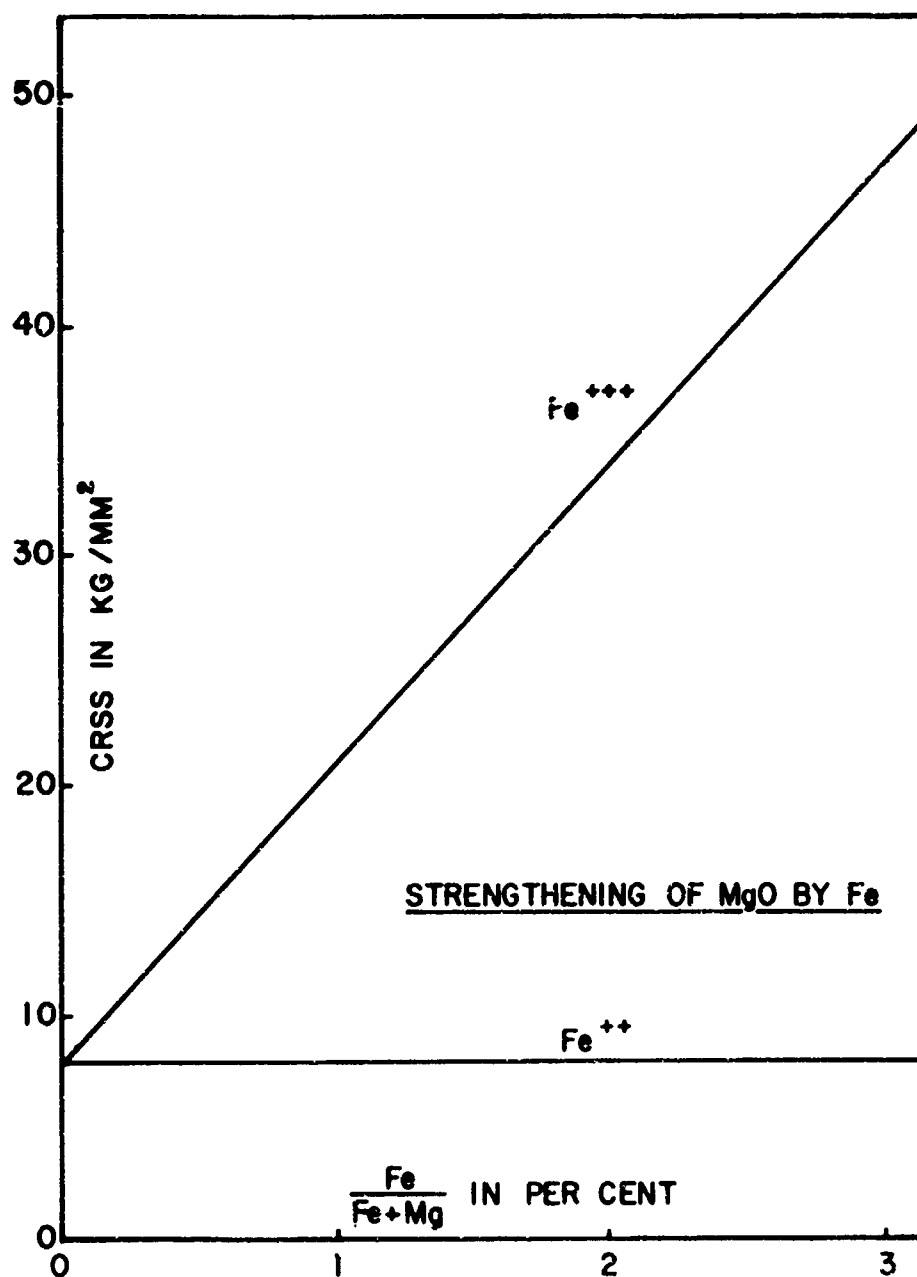
Figure 5. Effect of Dissolved Iron on Critical Resolved Shear Strength of MgO Crystals. Iron was diffused into MgO at $1400^{\circ}C$ and quickly cooled to room temperature, keeping it dissolved. Note that Fe^{+++} strengthens MgO but Fe^{++} does not. The shear strength was measured in bending and also from the inverse slip band lengths around hardness indents from a 136° diamond pyramid
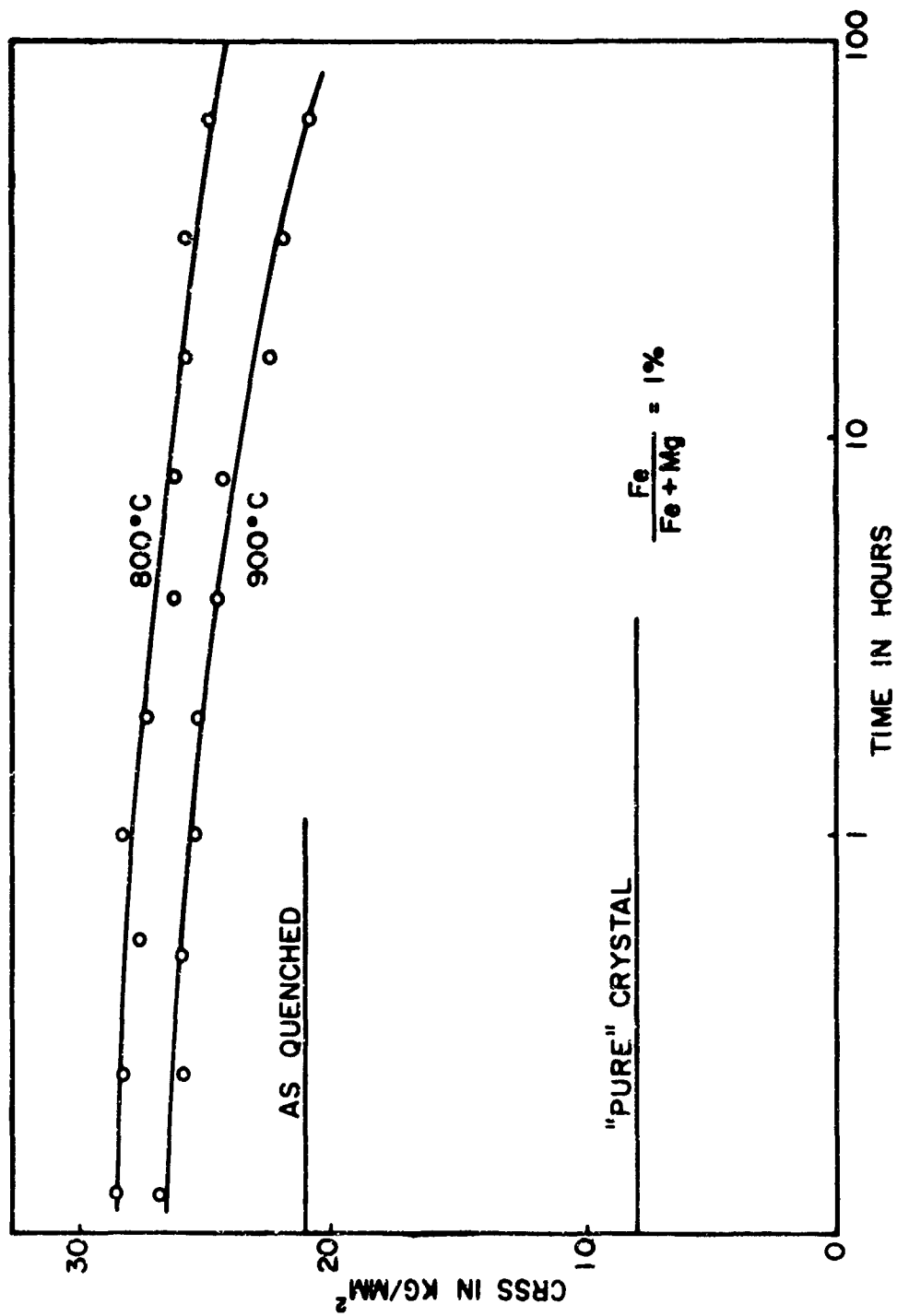
Figure 6. Effect of Precipitation Anneal on Critical Resolved Shear Stress of MgO Alloyed With 1.35% Fe/(Fe + Mg) in Air at 1400°C. The samples were air cooled to room temperature before aging
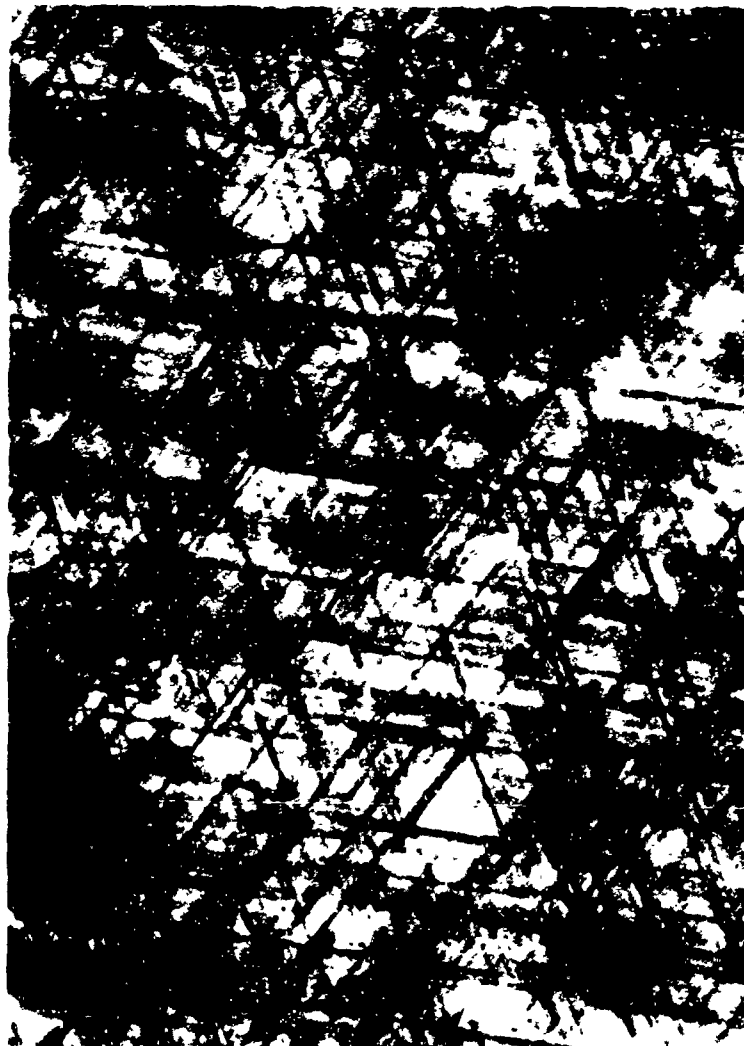
Figure 7. Precipitates in Al_2O_3-1/4% TiO_2. Crystals were grown by the flame fusion technique, annealed 2 hrs at 1850°C in air, furnace cooled, then aged for 4 hrs at 1550°C. The matrix is corumdum (α-Al_2O_3) and the precipitate is reported to be a solid solution of Al_2O_3 and Ti_2O_3. Magnification = 250 times
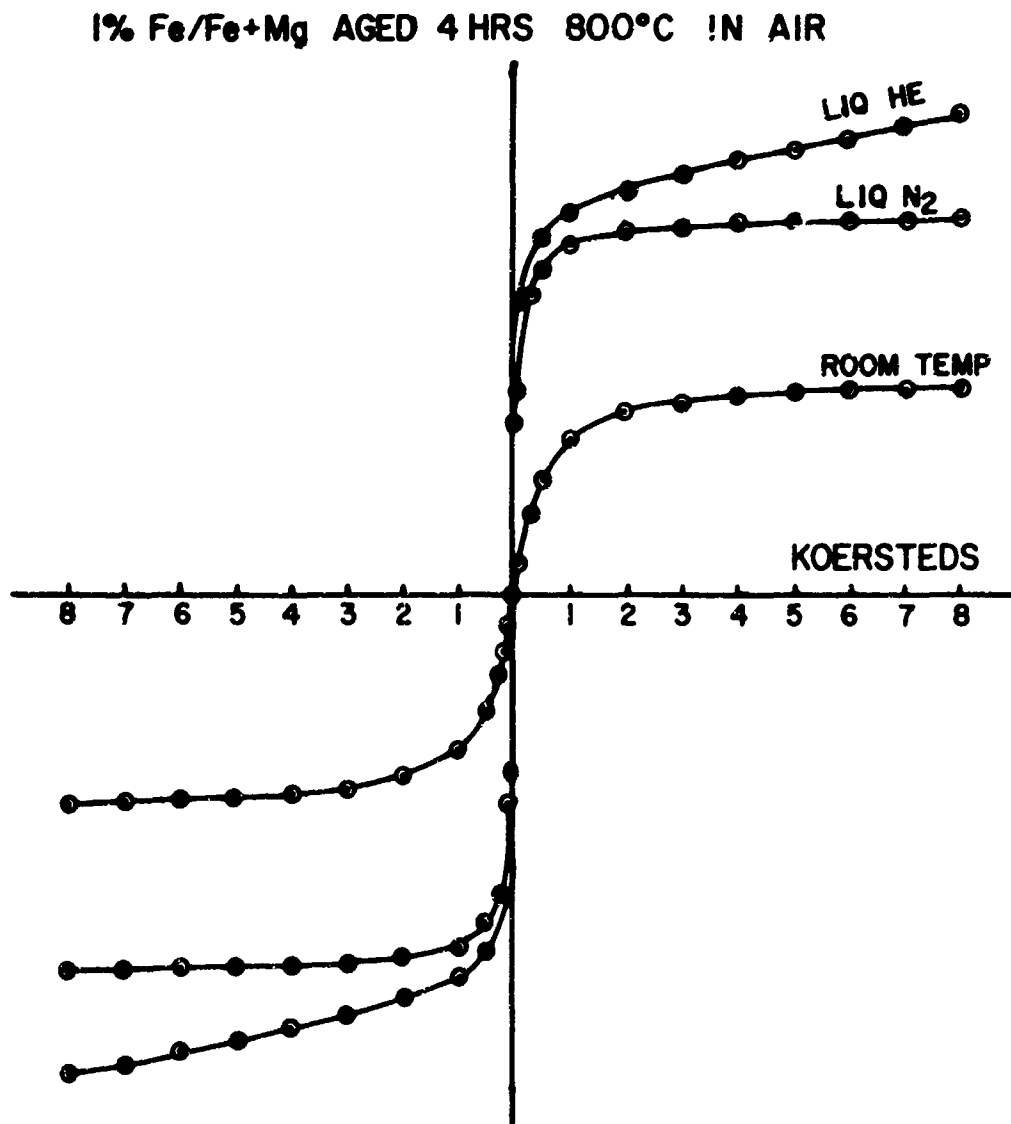
1% Fe/Fe+Mg AGED 4 HRS 800°C IN AIR

Figure 8. Magnetization Curves for 1% Fe/(Fe + Mg) Aged 4 hrs at 800°C (after air cooling from 1400°C)
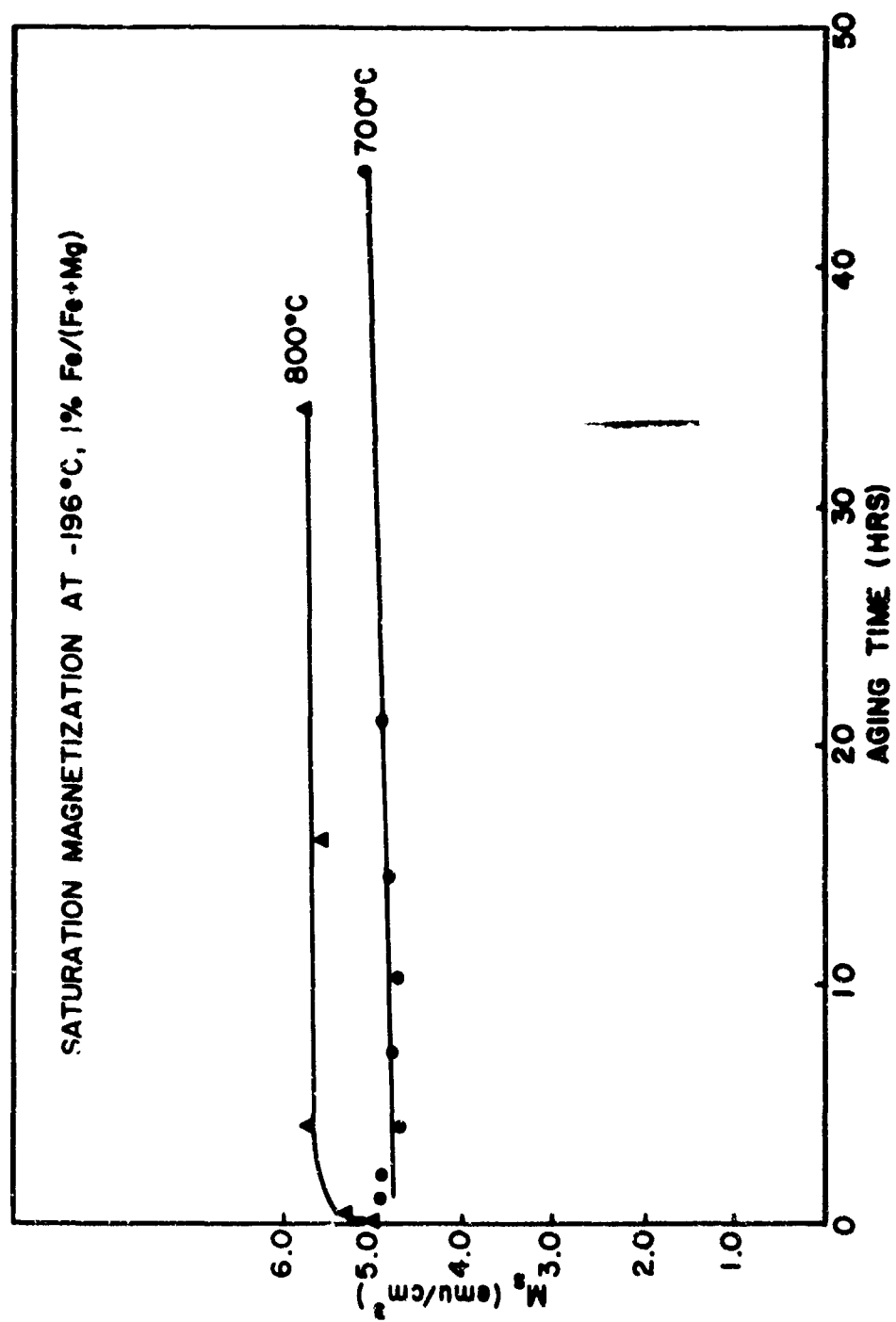
F gure 9. Saturation Magnetization at $-196^\circ C$ of 1% Fe/(Fe + Mg) Air Cooled from $1400^\circ C$ and Aged at 700 or $800^\circ C$. The unaged value of saturation magnetization is zero
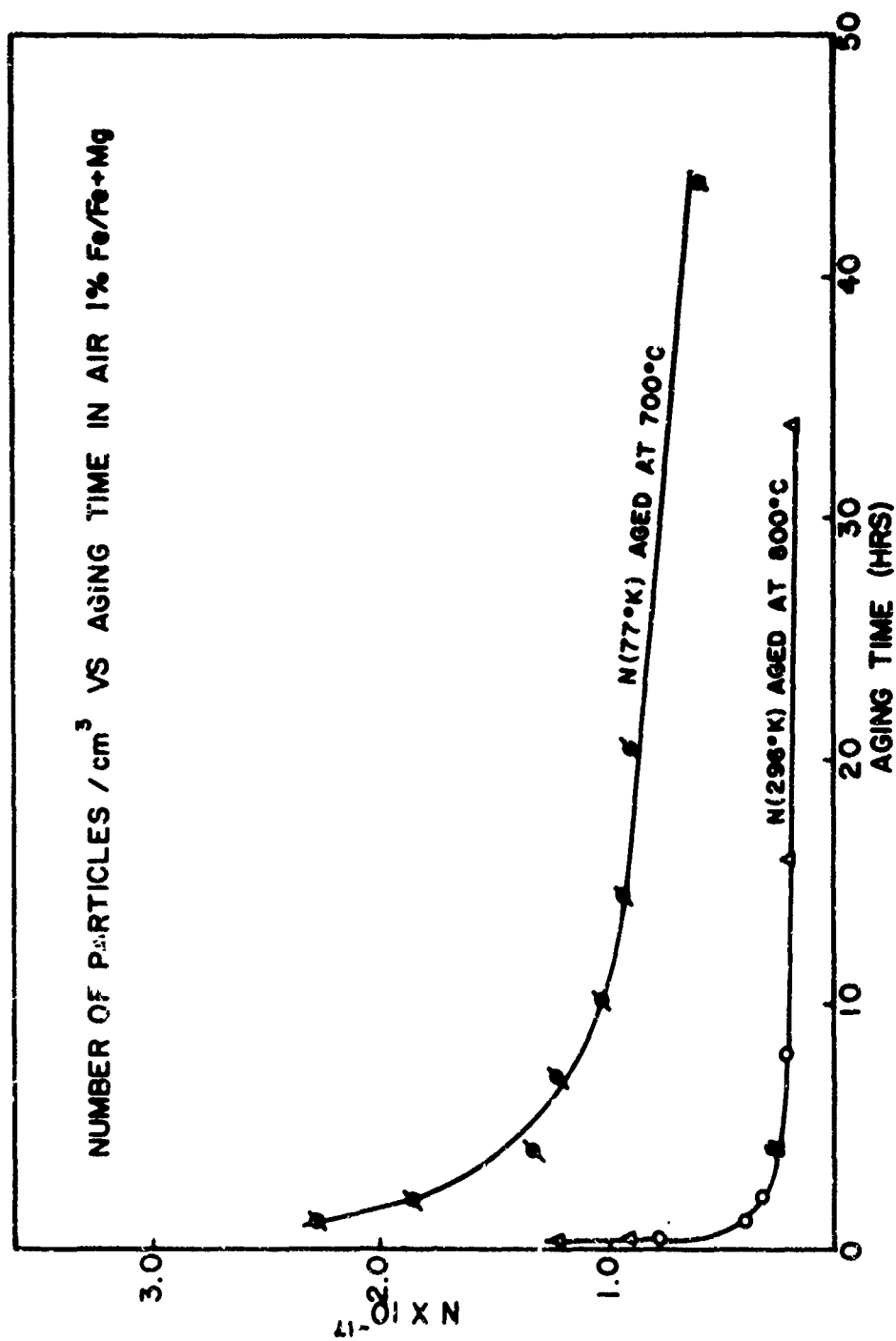
Figure 10. Number of Particles per cm^3 of Magnesioferrite Versus Aging Time in 1% Fe/(Fe + Mg). This was determined from the relation $M_S - M = nkT/H$. H is the applied field, M_g is the saturation magnetization, M is the value of magnetization a: H, T is the absolute temperature, n is the number of particles per unit volume, and k is Boltzman's constant

Dr. A. T. Stair, Jr. is a physicist with the Radiation Effects Branch, Optical Physics Laboratory, AFCRL. He is project officer of a research program on nonequilibrium radiative phenomena resulting from inelastic collisions and gas kinetic reactions. Dr. Stair participated in the 1959 meeting with the British on nuclear weapons, and is a member of the Thermal Panel of the DASA Weapons Effects Requirements Board. He holds a Ph.D. in physics from the University of Oklahoma and is a member of the Optical Society of America, the Faraday Society and the American Institute of Physics.

MOLECULAR BEAMS

by

A. T. Stair, Jr.
Optical Physics Laboratory
Air Force Cambridge Research Laboratories (OAR)
Laurence G. Hanscom Field
Bedford, Massachusetts

Molecular beams are destined to play a major role in the solution of many of the most pressing Air Force problems. The term molecular beam is defined ideally as a stream of molecules (or atoms) all travelling in the same direction and all with the same velocity; of course, this further implies a good vacuum so that the stream is not disturbed until one performs an experiment. Historically, the first molecular beam was devised in 1911 and through 1940 played a very fundamental role in physics, resulting in Nobel prizes with names like Rabi, Stern, Krusch and many others being closely associated with these techniques. These devices used ovens and collimating slits with good vacuums to permit the study of individual particles without perturbing collisions. Even so, the most exciting prospects of using collision-free streams of molecules have not yet been realized because the achievable velocity was limited by the highest temperatures at which ovens could operate, about 3000° K, which produces molecular velocities of the order of 1 km/sec. A temperature of 3000° K is also equivalent to 1/4 electron volts. You are familiar with the Mev (million electron volts) and Bev (billion electron volts) from the world of high energy accelerators such as the cyclotron. Figure 1 shows the direct relationship between the units of velocity, temperature, and electron volts; energy $= 1/2\ mv^2 = 3/2\ kT = e\phi$.

The importance of this regime of velocities to the Air Force can be seen in the next figure. Figure 2 represents our so-called "Flight Corridor." The velocities and altitudes represent the physical regime where missiles, satellites, and all aircraft must operate. These vehicles have collisions with the ambient atmosphere at such high velocities and low densities that we have been unable to reproduce them in the laboratory. These velocities also produce high temperature gases as can be seen schematically in Figure 3. Temperatures and conditions vary dramatically with vehicle design and velocity, but
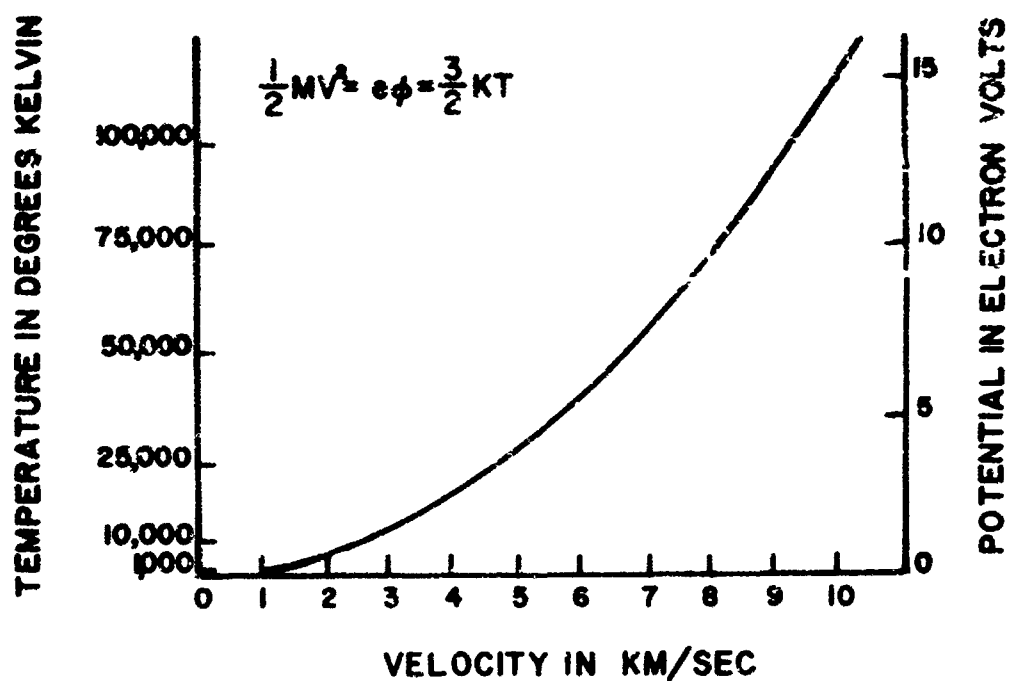
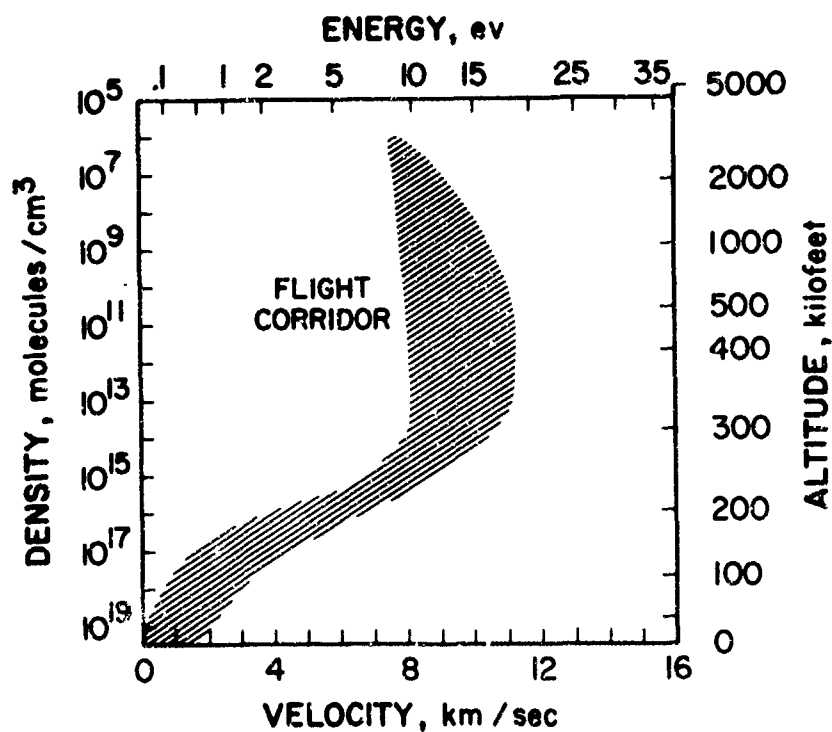Figure 1. Temperature or Potential Energy versus Velocity (N_2)

Figure 2. Flight Corridor

major problems such as heat conductivity, optical and radar character-
istics and others are often unknown without actual flight-testing various
concepts — a very expensive way to learn. Figure 4 illustrates some
of the high temperatures and high velocities also encountered during the
missile launch phase.

Current techniques to study such phenomena in the laboratory in-
volve primarily shock tubes and huge wind tunnels. Both approaches
have severe limitations and are often very poor approximations to the
conditions of interest. Shock tubes can reach high gas temperatures
but observation times are typically in the microsecond (10^{-6} sec) to
millisecond range (10^{-3} sec). In addition, there are always questions
about the true kinetic state of the gas under study. Supersonic and
hypersonic wind tunnels can reach the lower velocity range of interest
but cannot simulate high velocity flight with the actual densities and
temperatures; furthermore, there are even more serious scientific
objections about the initial state of the expanded gas (non-equilibrium
effects). Nevertheless, despite the expense of such techniques (hun-
dreds of millions of dollars) their value to the Air Force is inestimable.
I am not proposing that molecular beams will replace such facilities
but rather will permit measurements beyond the capability of these
techniques and, in fact, will contribute significantly to our understand-
ing of these devices themselves (shock tubes and wind tunnels). To
summarize, Table 1 lists various Air Force operational interests
which involve high temperatures and velocities. From a scientific
point of view the energy regime of 1 to 20 electron volts also encom-
passes the binding energy of molecules and, consequently, the activa-
tion energy of chemical reactions. This is the regime of everyday life;
for example, most solar energy arrives with 1 to 4-ev photons, chemi-
cal reactions run our automobiles, etc. With the notable exception of
the nuclear bomb, man's technical progress has been measured in the
units of low energy, the electron volt; yet, because we have been able
to build synchrotrons but not molecular accelerators we probably know
more about the nucleus than we do about the molecular bond.

Now, turn to the two important questions: (1) How do molecular
beams allow us to make such measurements? (2) What is new at
AFCRL that has been or will be of significance in this area? A molecu-
lar beam is the low energy analogue of the high energy accelerator.
The real key to scientific understanding is to be able to observe an
individual event such as an elastic scattering collision or a reaction.
There is so much energy in a nuclear event that a single collision can
be observed directly. With molecular beams we must observe instead
the statistical average of many identical events. The experiment is
conceptually the same, however, as long as each collision contributing
to the average is identical. It is pertinent to inquire as to why the
observation of an individual event is so important. By varying the
energy of the event (i. e., velocity of the beam) one obtains a micro-
scopic description as opposed to macroscopic where the phenomena
observed are the result of many collisions with various interaction
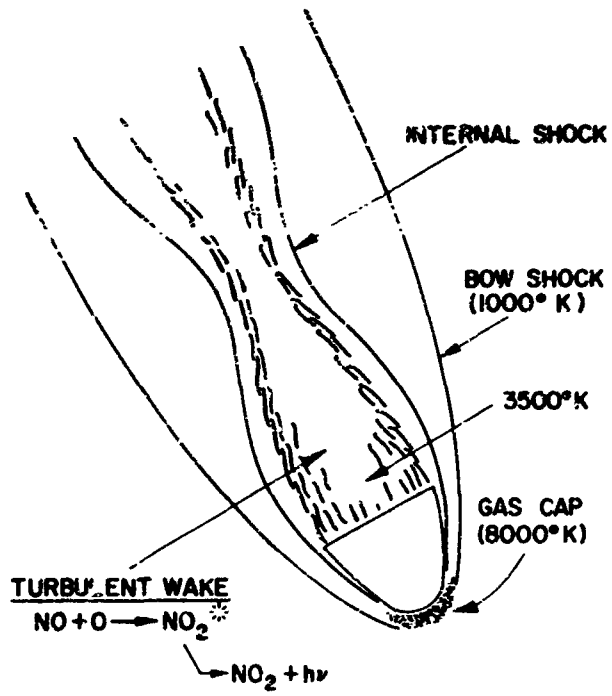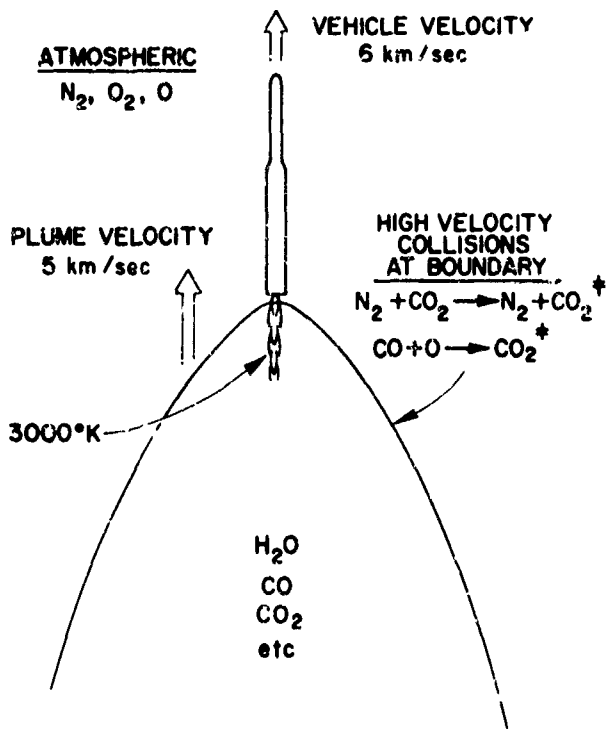
Figure 3. Re-Entry

Figure 4. Launch

TABLE 1: Air Force Areas Involving High Temperatures and/or High Velocities

EARTH ORBIT RE-ENTRY 6.7 KM/SEC (22,000 fps)

gas cap 7000 - 10,000°K

shock layer 1000°K

wake region:

blunt body neck - 3500°K

mixing region 1000 - 2500°K

slender body neck - 5400°K

SUPER ORBITAL RE-ENTRY 8 KM/SEC (27,000 fps)

gas cap - 12,000°K

HYPERSONIC FLIGHT

X-15 Mach 6 (2 KM/SEC) 1000°K

hypersonic aircraft Mach 6 1000 - 1500°K

Mach 12 5000°K

SUPERSONIC COMBUSTION

combustion temperature 1000 - 3000°K

NUCLEAR FIREBALLS

detonation - 100,000°K

long time - 5000°K to ambient

energies (such as a very hot gas at some density). The vital difference is that with a <u>microscopic</u> understanding one is able to predict aggregate phenomena that cannot be reproduced in the laboratory, whereas from a <u>macroscopic</u> measurement one is unable to unscramble and identify the contributions of the important parameters.

At high velocities the molecules actually come closer together and the close-in repulsive forces (sometimes called chemical forces) control the phenomena. In a soft collision (low temperatures) the dominant interactions result from the long range attractive forces. These forces are best understood in terms of the intermolecular potential ϕ. All of the important processes of interest such as optical and electrical observables, satellite aerodynamics, gaseous heat conductivity, and reaction rates of chemical process (i. e., supersonic combustion) are the <u>macroscopic</u> results of the intermolecular law of force ($\nabla \phi$) acting during a collision. The <u>most</u> <u>fundamental</u> <u>problem</u> <u>in low</u> <u>energy</u> <u>physics</u> is to understand <u>in detail</u> the mechanisms of a <u>collision</u> between two molecules (atoms, ions) with relative energy of 1/2 to 20 electron volts. For example, to obtain the thermodynamic properties of a gas, one must use the real equation of state,

$$PV = RT \left[1 + \frac{B(T)}{V} + \frac{C(T)}{V^2} + \ldots \right] ,$$

instead of the ideal gas law $PV = RT$, where P is pressure, V is volume, R is the molar gas constant, and T is the temperature. The coefficients are called the virial (force) coefficients and B(T) accounts for the interaction ("collision") of two particles, C(T) accounts for the interaction of three particles, etc. Statistical mechanics provides an <u>exact</u> derivation of B(T) in terms of the intermolecular potential $\phi (r)$;

$$B(T) = 2 N_0 \int_0^\infty (1 - e^{-\phi/kT}) r^2 \, dr.$$

A recent measurement of ϕ for a rare gas interaction showed extrapolated data from low temperature measurements to be in error by 700 percent.

That molecular beams will help in predicting satellite aerodynamics results from the fact that the gas-surface collisions at high velocities are the primary lift and drag forces acting. This is illustrated in Figure 5. The unknowns in drag and lift calculations are the coefficients C_D and C_L which are defined in terms of energy and momentum accommodation coefficients. These are expressions of how the energy and momentum exchange occurs at the surface, as defined in Figure 6. Again in reference to Figure 5, notice that the forces acting are a product of the relative velocity u (squared) which is usually known, the density ρ which may not be so well known, the normal area A intercepted and C_D or C_L. Without <u>a priori</u> knowledge of C of ρ, they cannot be separated. However, if the coefficients, C,
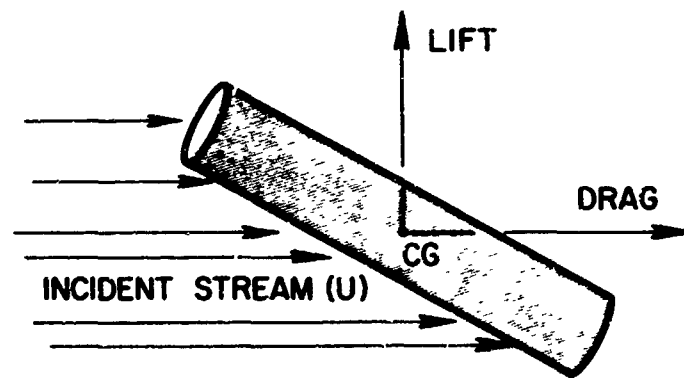
$$\text{DRAG} = C_D \frac{1}{2} \rho U^2 A$$

$$\text{LIFT} = C_L \frac{1}{2} \rho U^2 A$$

Figure 5. Aerodynamic Forces
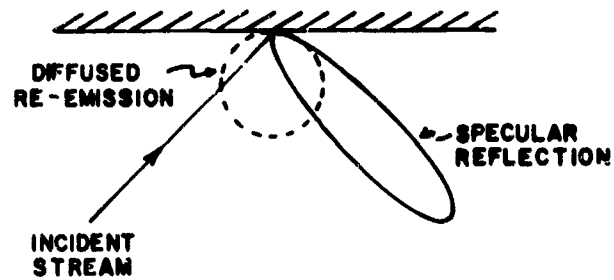
$$\alpha = \frac{E_i - E_R}{E_i - E_s} \qquad \text{ENERGY}$$

$$\sigma' = \frac{P_i - P_R}{P_i - P_s} \qquad \text{NORMAL MOMENTUM}$$

$$\sigma = \frac{T_i - T_R}{T_i} \qquad \text{TANGENTIAL MOMENTUM}$$

Figure 6.   Definition of Accommodation Coefficients

can be determined in the laboratory, ρ can be accurately measured from satellite orbit decay. Subsequently, from observations of the aerodynamics, one can determine A; therein lies one of the keys to discrimination of light-weight decoys from a nuclear warhead.

Finally, we turn to the pertinent question of what's new. From 1940 to 1952 there was no advance in techniques to produce beams with 1 to 10 km/sec velocity. Then the first molecular "accelerator" which showed promise for the 1 to 10 ev region was the supersonic nozzle (SSN) suggested by Kantrowitz and Grey. This technique has been under development primarily by Prof. E.W. Becker et al. in Germany and a group at Princeton University under the direction of Prof. J.B. Fenn. This device makes use of the properties of a gas during expansion through a nozzle to convert the thermal internal energy of the gas into directed motion. A schematic representation of a system using this nozzle beam is shown in Figure 7. The availability of large dynamic pumping systems has advanced the development of this source. Unfortunately, to reach the desired energies will require a hot light carrier gas such as H_2 "seeded" with the heavy molecule of interest. A great deal of effort has defined, reasonably well, the properties of the expanded gas and one can now anticipate the beginning of many useful experiments using this technique. Figure 8 is a schematic diagram of an experiment under way in the Optical Physics Laboratory utilizing SSN for the investigation of important excitation processes. The principal area of interest is the question of mechanisms creating infrared missile trails. The objective of the experiment, as depicted, is to measure the excitation cross section for an energetic collision between an exhaust gas such as CO_2 with the ambient atmosphere (i.e., N_2).

Two other new techniques which offer much more potential in beam flux, energy range and selection are only a year old in concept but well under way in development at the Optical Physics Laboratory of the Air Force Cambridge Research Laboratories. The first involves an important new idea in the use of a charge exchange system. A discharge produces ions in the species of interest and for the first time an axial magnetic field guides the neutral plasma to the electrostatic acceleration region. A schematic diagram of this CEX system is shown in Figure 9. The electrons have 25 to 40-ev velocities and the ions are thermal; consequently, there is no space charge expansion from the discharge region to the acceleration region and even accelerating the ions to 10 volts does not separate all of the electrons. Thus, there is maintained a large flux up to the region where charge exchange takes place. This process neutralizes about 50 percent of the accelerated beam with little attenuation since the resonant electron exchange process is typically two orders of magnitude larger than elastic scattering. This system promises at least four orders of magnitude improvement (c.a. 10^{14} molecules cm^2 sec) over other charge exchange beams at 10 electron volts.
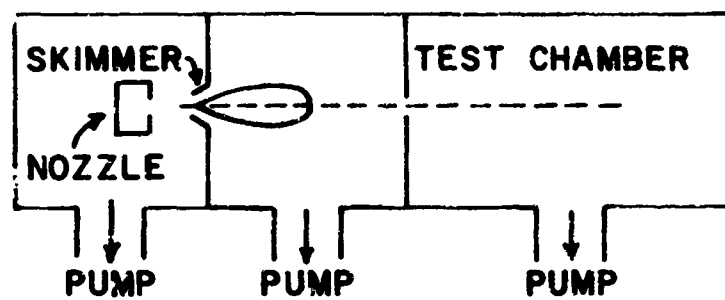
$$\text{BEAM} \qquad 10^{17} \, (\text{CM}^2\text{-SEC})^{-1}$$

ENERGY   2 - 10 ELECTRON VOLTS

VELOCITY   3 - 8 KM/SEC

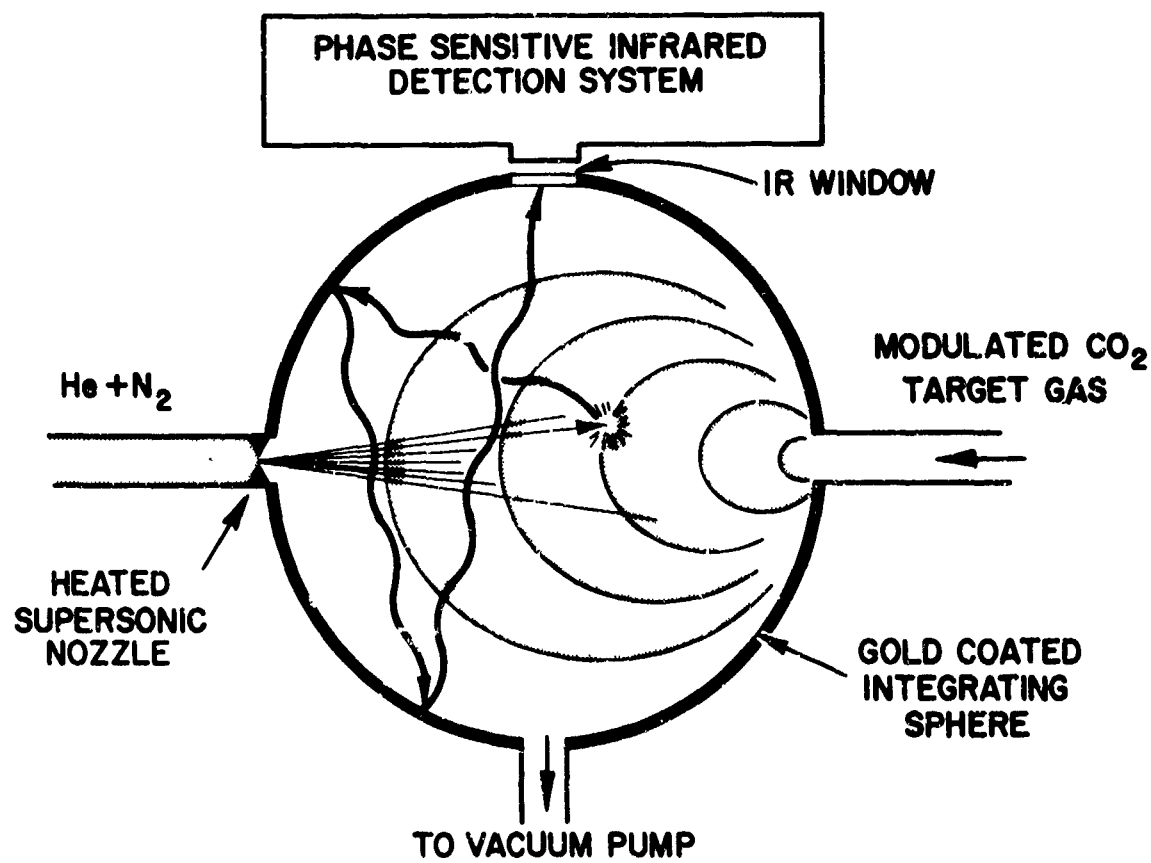Figure 7. Supersonic Nozzle Beam

Figure 8. Infrared Collision Cross-Section Measurement Apparatus
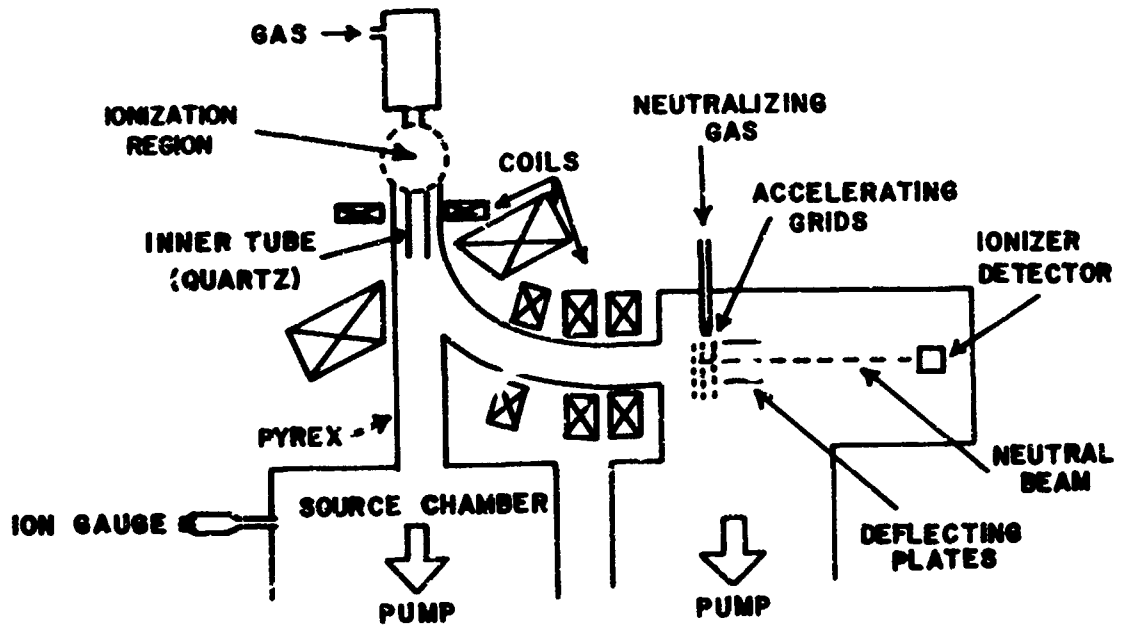
Figure 9.   Charge Exchange Molecular Beam Apparatus
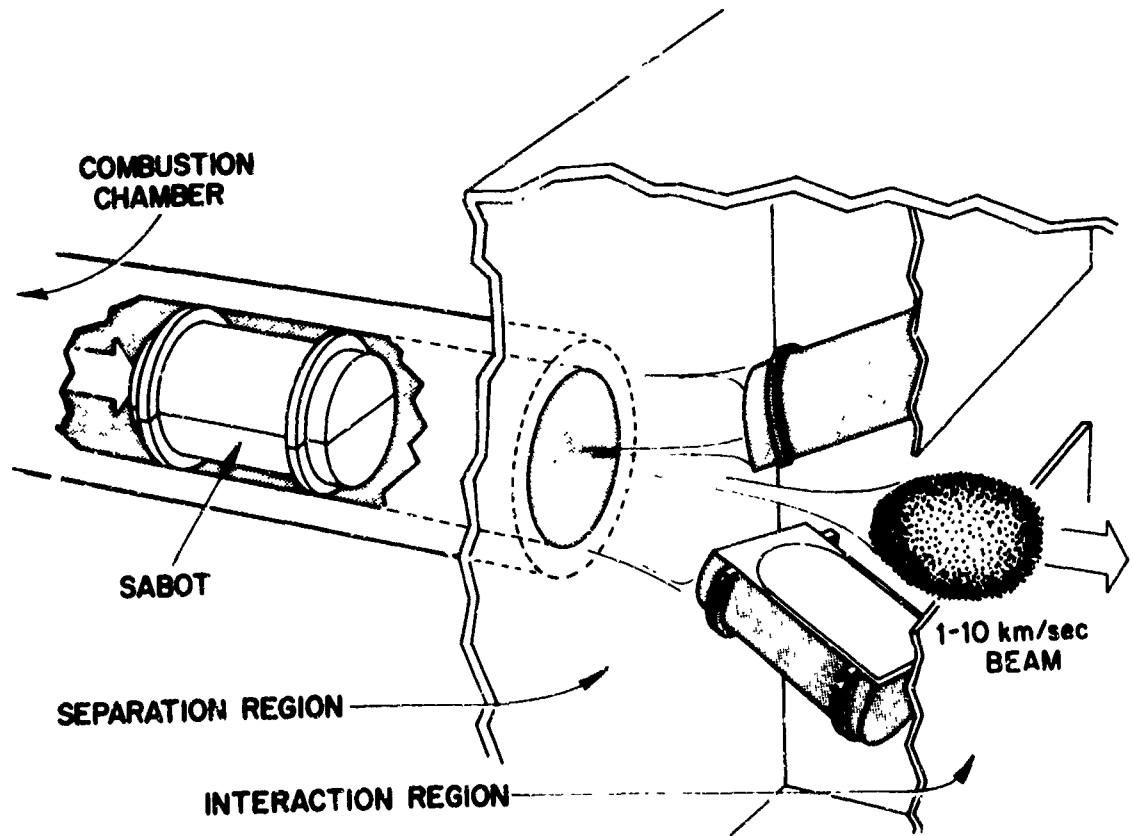

Figure 10.   Mass Molecular Beam System

The second breakthrough is an extremely simple concept. One takes a rifle bullet, hollows it out, fills with a gas of interest, seals with a membrane, fires into a vacuum and stops the bullet while simultaneously rupturing the membrane (there are many variations, of course). A schematic representation of this system is shown in Figure 10. This single shot of gas can have a very large flux and even a .22 calibre rifle will attain 3 km/sec (energy is dependent, of course, on the mass of the species). Light gas guns in hypervelocity ranges can accelerate sabots to 10 km/sec and a design study shows a flux of 10^{25} particles/cm^2 to be feasible. This system has been named the MASS beam, a coined word that signifies Mechanically Accelerated Single Shot. By controlling the time of acceleration one can also control the state of the gas in the beam.

Because of the many areas of applicability, the development of new techniques for producing high intensity beams can be considered more important than any of the scientific fields considered separately. As has often been said, it is really all a matter of intensity, but, more, it is a question of signal-to-noise. A better detector, capable of sensing fewer molecules, is just as valuable.

This probe is so basic to low energy physics (or high energy chemistry) that one can foresee the pendulum of scientific inquiry swinging back from high energy nuclear physics. Furthermore, the technical offshoots of such things as understanding chemical reactions for "controlled chemistry" and propulsion, even life processes, are so promising that strong efforts in the field of molecular beams may be more productive to mankind than NASA's flight to space, and far less expensive.

Captain John F. Schaefer is assigned to the Aerospace Mechanics Division of the Frank J. Seiler Research Laboratory. Prior to coming to FJSRL he worked at Wright-Patterson AFB as a maintenance officer for flight test radar and as a flight test engineer for radar, navigation and electronic counter-measures equipment. Capt. Schaefer graduated from West Point in 1958 and holds a M.S. and Ph.D. in electrical engineering from Stanford. He is a member of Sigma Xi and the Institute of Electrical and Electronic Engineers.

THE CONTROL OF UNSTABLE MECHANICAL SYSTEMS

John F. Schaefer, Captain, USAF
FJSRL, OAR, USAF Academy, Colo 80840

Unstable mechanical systems constitute a class of dynamical systems which have been of increasing interest to control theory engineers the past decade. The most noteworthy example of such a system is a steerable rocket vehicle during its launch phase. Aerodynamically unstable at low speeds, such a vehicle requires a sophisticated control mechanism to insure that it follows the desired trajectory. The present tempo of successful launches and missions indicates that sufficiently sophisticated controllers have been designated for today's vehicles, but it is not clear that contemporary techniques will suffice for the future. This possibility alone justifies an investigation into the control and controllability of unstable systems in general.

The research discussed in this paper is directed to a particular type of unstable mechanical system, one whose dynamic behavior is similar to that of a rocket booster at liftoff. The subject device, shown in Figure 1, consists of a thin, flexible beam hinged at its lower end to a motorized cart. Like the rocket booster, the beam tends to fall over unless corrective lateral thrusts are applied to the cart. Unlike today's rocket vehicles, the beam is highly flexible; but with the continuing stress on maximizing the payload-to-vehicle structure

Figure 1

Limber Beam Controlled Experimentally

mass ratio it would appear likely that future missile bodies may become increasingly structurally flexible -- particularly so if control systems able to cope with the complex body motions are available.

To a significant degree it was concern for this eventuality which motivated the work discussed below. Primarily, however, it was felt that an investigation of the properties and problems of a specific mechanical system such as that of Figure 1 would lead to results generalizable to a broader class of unstable systems. To a reasonable extent this course has proven fruitful. The major results, to be summarized in the body of this paper, yield some unexpected conclusions.

Goal and Approach

The problem initially posed in this investigation was to design, build, and operate a control system, utilizing a bounded (limited output) controller, for the device of Figure 1. As has been pointed out, it was expected that in the pursuit of this fundamental goal other questions would be answered, such as:

1. How flexible may the beam be before the overall system is uncontrollable?

2. What similarities does this assembly have to a flexible booster vehicle?

3. How serious a constraint does the <u>bounded</u> control thrust impose on controllability?

The initial step in the analysis was to obtain the equations of motion of the system. Because the beam is a distributed-parameter system capable of an infinite number of degrees of freedom, it was decided to approximate the actual device with a lumped-parameter model yielding ordinary differential equations of motion. Figure 2 shows this discrete mathematical model. The cart, of mass M_o , supports N identical massless rods of length ℓ. (This will be referred to as an N-lumped model.) The rods are hinged to each other in frictionless joints at either end. Point masses m_i corresponding to the mass of a segment of length ℓ in the actual beam are located at the joints. To account for the elastic stiffness of the beam, springs proportional to the EI (modulus of elasticity -- cross-sectional moment of inertia) product are also assumed at each of the joints. The coordinates used to specify the inertial orientation of the assembly are ϕ_o, the displacement of the cart from some reference, and ϕ_i, i = 1, 2, ... N, the angular displacements of each of the N rods from the vertical. The resulting equations of motion then represent a discrete dynamical system of order (2N+2), with N, the numbered rods, taken large enough to satisfy the desired degree of accuracy in the approximation. Two

Figure 2

Mathematical Model of Limber Beam
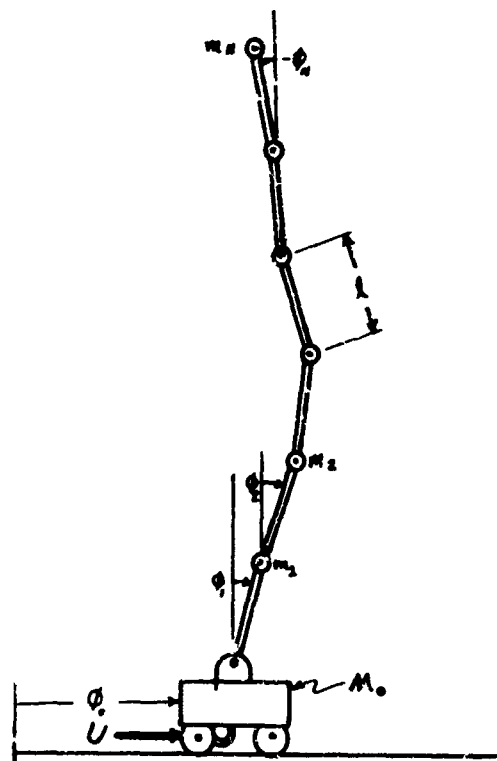
further idealizations are then made: structural damping in the beam is assumed to be negligible (which was quite reasonable for the actual beam employed), and small motions were assumed, enabling linearization of the equations. With these simplifications and a change in coordinates (this change merely results in measurement of the displacements of the rods from a different reference) the equations of motion can be uncoupled and be written as

$$\ddot{\theta}_i + \omega_i\, \theta_i = b_i\, U\ , \qquad i = 0, 1, 2, \ldots N \qquad (1)$$

where U is the accelerating force furnished by the d.c. motor on the cart, each θ_i represents the instantaneous value of the ith normal mode with each ω_i its natural frequency, and each b_i determines the influence of the control on that mode. Because of the change in coordinates each ϕ_i is now a linear combination of the $\theta's$. This creates no mathematical difficulty and is done to simplify the mathematics and the physical understanding of the problem. The mathematical details for what is developed in the subsequent sections can be found in reference [1].

Control Techniques for a Stiff Beam

The physical significance of the $(N+1)$ second-order differential equation in (1) can now be discussed. If the beam is sufficiently

134

"stiff" (such that, when released from a near vertical position it does not collapse upon itself as would a strand of wet spaghetti) one finds that ω_0^2 is zero, ω_1^2 is negative, and the remaining $(N-1)$ ω_i^2's are positive. This means that there is one mode (θ_0) which does not decay (the cart, if $U \equiv 0$, does not seek out a zero position); one mode (θ_1) which grows unbounded as time progresses (the beam falls over if $U \equiv 0$); and $(N-1)$ modes $(\theta_2$ through $\theta_N)$ which are oscillatory or vibratory (the so-called "bending modes" of the beam). The initial goal is to determine a control U which is a function of the displacements of the rods and which will force the system described by (1) to the equilibrium $(\theta_i \equiv 0)$ and thus, since the ϕ's are linear combinations of the θ's, the beam will be vertical and the cart will be at the (arbitrary) reference ϕ_0.

Initially it is worthwhile to note what can be accomplished if it is assumed that the control U is unbounded (the d.c. motor powering the cart can furnish as much thrust as desired, without limit) and a conventional linear position-and-rate feedback controller synthesized. Most U.S. boosters in use today use such a <u>linear</u> control scheme. Using such a scheme one can show that only <u>rate</u> feedback need be employed on the oscillatory modes. It is important to note that the result holds for any number of rods and that all modes are actively controlled, up to and including the highest-frequency bending mode. Since the number of rods will normally be large, to insure that the mathematical model closely approximates the actual device, it is important that the feedback control law be useable for an arbitrary large number of rods, N. On the other hand, it should be pointed out that all $(N+1)$ modes do not <u>need</u> to be controlled. Normally one would wish to control just the first two modes $(\theta_0$ and $\theta_1)$, and those bending modes θ_2 through θ_j, $j < N$ (it is assumed that $\omega_i < \omega_j$, $i < j$), for which the assumption of negligible natural damping is particularly valid (that assumption becomes poorer as the bending mode frequency increases). Those modes which are not controlled actively are allowed to decay naturally by the mechanism of the mathematically negligible structural damping. Again, the stable equilibrium of the closed-loop system is that at which all the displacements, the θ_i's, are zero.

When one removes the impossible-to-achieve relaxation of an unbounded U, then the question of controllability of the device as a function of initial conditions becomes paramount. Assume the absolute value of U has an upper bound, U_{max}. Then, without regard for a control <u>law</u>, the range of initial states which can be stabilized becomes limited. This region in $(\theta_i - \dot{\theta}_i)$ space can be determined by examining the second of the $(N+1)$ equations in (1), which describes the time behavior of the unstable mode. The region appears as a "sandwich" in the state space, and the analysis shows that its thickness increases linearly with U_{max}. For a given U_{max}, controllability of the assembly can be expressed as a simple inequality involving U_{max}

and the amplitude and rate of the mode θ_1; this in turn is directly expressible in terms of the original coordinates ϕ_i and their velocities [again, Reference 1 describes this more fully].

a   b
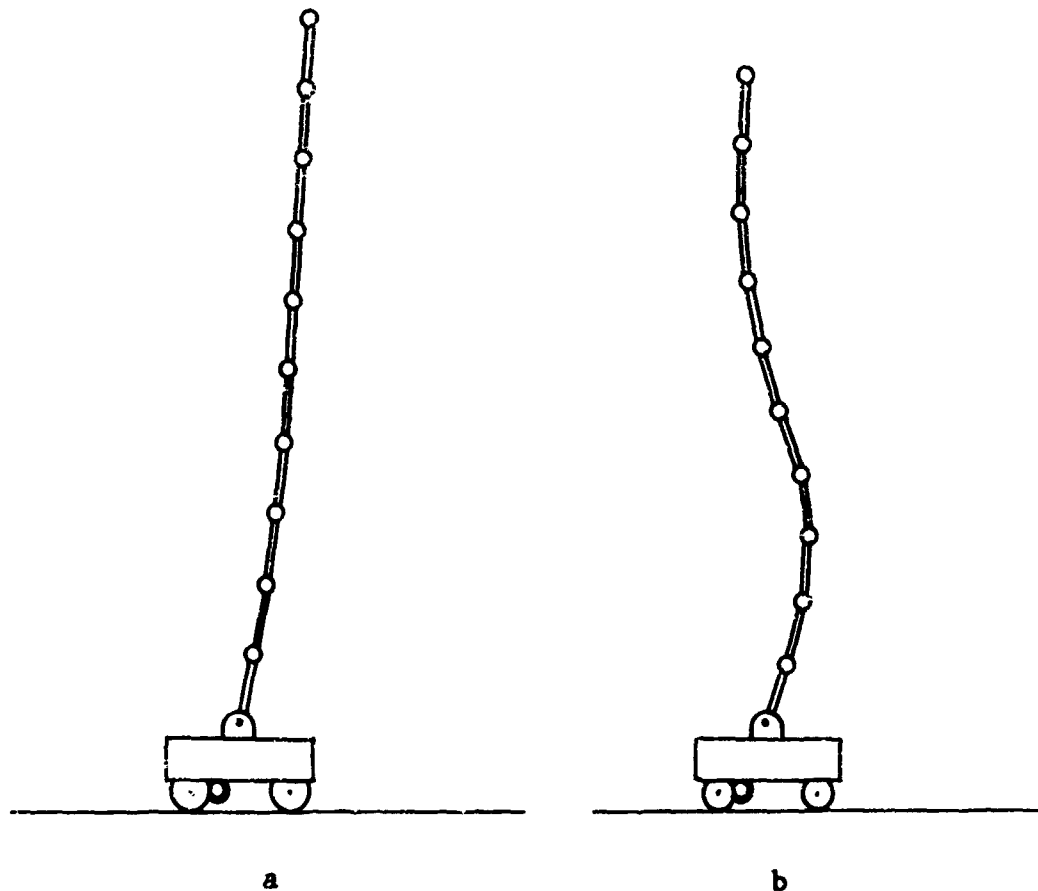
Figure 3   Ten-Lump Model in   a)   Uncontrollable Configuration
                                      b)   Controllable Configuration

A possible application of the above is depicted in Figures 3. It is assumed that all velocities $\dot{\phi}_i$ are zero in both configurations, and that U_{max} is identical in either figure. Then the inequality mentioned above divulges that the 10-lump model in Figure 3a is outside the controllable region, while in Figure 3b it is interior to the "sandwich" and is thus controllable.

Reference 1 contains a detailed dicussion of two "bang-bang" control laws useable with a bounded control thrust (bang-bang implies that in operation the cart motor is always full on in either the forward or reverse direction, and reverses between these two states

instantaneously). One law, a linear input to the motor relay, is simple to implement and can yield stable operation for small initial conditions. The second, more complex, can stabilize the system (to include any number of bending modes) from throughout the region of controllability (the sandwich discussed above).

All of the control laws investigated require that all of the model's physical coordinates and their velocities be available for measurement if all (assumed) modes are to be controlled. In practice this is difficult and expensive. With regard to the physical device, this theory requires that, if an N-lump model has been assumed and one wishes to control actively all normal modes of the system, then (N+1) position and velocity sensors must be employed. However, this is not necessary merely to stabilize the physical device, and in practice was not done. Normally one would wish to control the non-decaying mode (associated with cart position), certainly the unstable one, and, say, the first M of the bending modes. This would require at minimum (M+2) position sensors and one filter designed to approximate the first (time) derivative of a sum of outputs of the position sensors.

The model shown in Figure 1 was operated extensively, utilizing a linear input to the relay switching the d.c. drive motor (i.e., a bang-bang control law). The beam was six feet long and very flexible, as indicated by the 0.516 cps natural frequency of its first bending mode. All analysis used to determine feedback coefficients, sensor locations, etc., was based on a nine-lump approximation. Four position sensors were employed: one potentiometer measured cart position Φ_0; one the beam angle Φ_1 at the hinge; and two strain gages furnished signals proportional to the difference in slopes of two adjacent beam segments [these were $(\Phi_4 - \Phi_3)$ and $(\Phi_7 - \Phi_6)$]. The device was operated for periods of up to three minutes.

Controllability of a Uniform Beam as a Function of Structural Stiffness

This section attempts to answer the second of the questions posed above, i.e., how does the EI product influence the controllability of the experimental assembly? It has been stated that if the beam is stiff enough, then any control force, however small, can stabilize the system in some region near the equilibrium. The question now is: "As the elastic stiffness of the structure is decreased, does the same result hold? Can transverse forces, properly applied to the cart, return the system to the equilibrium from non-zero initial conditions?"

Some answers to this question, applicable at least to the mathematical model of the physical system (with a uniform beam implicit), are:

1. As the EI product of the beam is decreased from the nominal value assumed in the previous section, it can be shown that the N-lump

model undergoes (N-1) discrete stages of non-controllability. This means that no transverse force, whatever its magnitude, can correct an arbitrarily small (non-zero) initial condition when applied to the cart as shown. In between the discrete critical EI values causing this phenomenon the system remains controllable.

2. In the limit EI = 0 (no structural stiffness whatsoever) the N-lump model can be controlled in the manner prescribed, even by a bounded control force of arbitrarily small magnitude (again, of course, the size of the region of controllable initial conditions decreases with decreasing available maximum thrust).

As these results are valid for arbitrarily large numbers of rods, the implication is that the uniform beam could be balanced even though, if the control were turned off and the beam slightly disturbed, it would tend to collapse upon itself. Yet, at a slightly larger EI product, it could not be balanced at all! To suggest, as Result (2) above would seem to imply, that a limp rope could be mounted on the cart and balanced vertically, would intuitively be carrying the analogy too far. Nevertheless, Result (2) does indicate that an arbitrarily large number of light rods, pinned to each other with heavy pins as in Figure 2, could be balanced vertically by the cart -- or perhaps by a juggler moving his palm only horizontally.

Figure 4

Two-Rod Model Controlled Experimentally
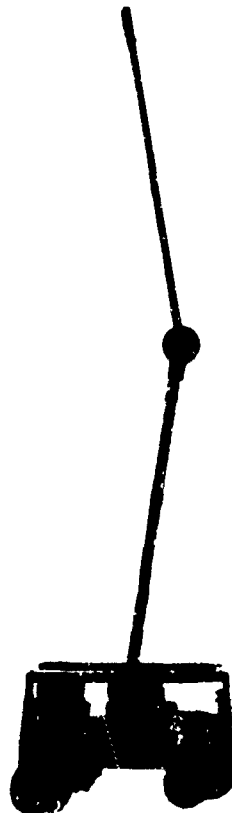
To lend some credence to the foregoing, the model shown in Figure 4 was constructed and operated for extended periods. It consists of two slender, rigid rods pinned to each other; the lower rod pinned to the cart. As before, the goal is to force the cart motor to drive the cart horizontally so as to balance the rods vertically. There is no spring at either of the hinges, and very little friction exists, thus this device is quite similar to the model of Figure 2. It constitutes a sixth-order system with two modes of instability, and represents a challenging control problem. The control employed was again a linear combination of positions and rates fed to the relay switching the cart motor. Such bang-bang control synthesis techniques for systems exhibiting multiple unstable modes are discussed in reference 2.

Areas of Potential Application

If the conjecture of increasingly flexible missiles in the future is valid, then these developments appear to have some potential in the field of steerable booster vehicle design. The equations of motion for a vehicle being accelerated by a longitudinal thrust and whose path is controlled by variable lateral thrust would be quite similar to those describing the experimental model of Figure 1, with additional terms due to the accelerating longitudinal thrust entering as do those due to gravitational forces. If, in addition, the vehicle has negligible cross products of inertia about its longitudinal and transverse body axes, it is anticipated that control in the third (transverse) dimension could be similarly implemented with little additional complication. A typical approach in booster attitude control system design is to assume a model capable of at most two bending modes, synthesize a stable control law for that model, and by means of electronic filters on the sensor(s) prohibit all bending mode information of higher frequency content from being fed to the control loop. The approach evolved above enables one to actively control any number of bending modes, granted sufficient sensors.

From the discussion of controllability of the beam versus elasticity one can extrapolate the possibility that a sufficiently flexible missile, being accelerated by a large longitudinal thrust, may become uncontrollable and buckle at critical thrust levels; yet at somewhat larger thrust levels again be controllable. It should be noted that in a similar investigation [3] Beal has concluded that longitudinal thrust levels on today's boosters are lower, by a factor of approximately five, than that required for contemporary structures to buckle due to critical inertial loading.

It has been suggested* that this theory might be applied in the development of a highly mobile, quickly erectible, communications antenna.

---

* by Brig. General O.G. Haywood (USAF/Res), member of the OAR Scientific Advisory Group and President of the Huyck Corporation.

Figure 5

Ungyved Mobile Communications Antenna
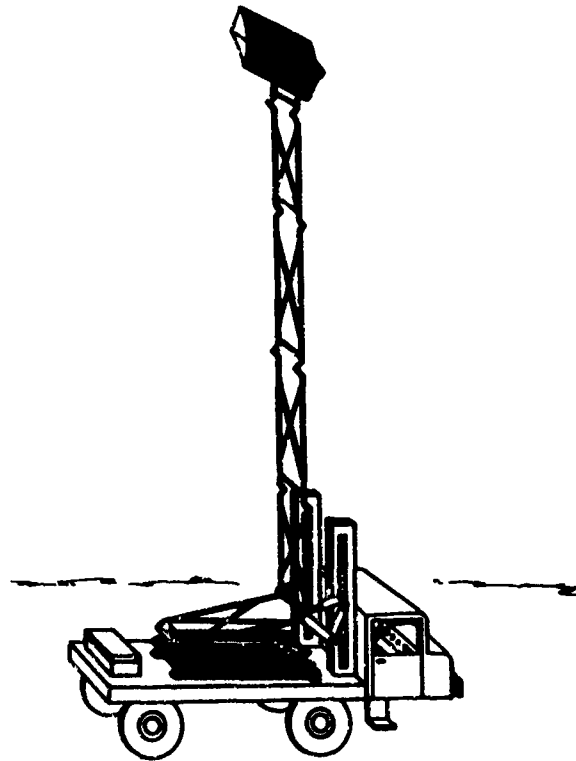
The proponent has envisioned a configuration similar to that shown in Figure 5. It consists of many rigid segments, folding upon one another, on a mobile base. The segments, or links, would be erected one at a time by the erection mechanism while the mobile base moves horizontally so as to keep those links already raised vertical.

References

1. Schaefer, J.F. and Cannon, R.H., Jr., "On the Control of Unstable Mechanical Systems", to be presented at the 1966 meeting of the International Federation of Automatic Control, London, England, June 1966.

2. Higdon, D.T., "Automatic Control of Inherently Unstable Systems with Bounded Control Inputs". Ph.D. Dissertation, SUDAER Report No. 176, Department of Aeronautics and Astronautics, Stanford University, Stanford, California, December 1963.

3. Beal, T.R., "Dynamic Stability of a Uniform Free-Free Beam Under a Gimballed Thrust of Periodically Varying Magnitude", Ph.D. Dissertation, SUDAER Report No. 161, Department of Aeronautics and Astronautics, Stanford University, Stanford, California, June 1963.

Dr. Harry A. Lipsitt is Supervisor, Metallurgy Research, Metallurgy and Ceramics Research Laboratory, Aerospace Research Laboratories. Currently he is conducting research on the mechanisms of metal fatigue in class-packed hexagonal metal titanium with interstitial elements and alloys of Ti, and cooperating in studies of fatigue limits in pure iron, the anomalous elastic behavior of chromium near the Neel temperature, and the metallography of crack propogation in cumulative damage fatigue tests. Dr. Lipsitt holds the B.S. Degree from Michigan State University and a M.S. and Ph.D. in Metallurgy from Carnegie Institute of Technology. He holds membership in Tau Beta Pi, Sigma Pi Sigma, Sigma Xi, The American Institute of Metallurgy and the American Institute of Metallurgical Engineers. He has published fifteen articles, seven of which deal with metal fatigue.

The Determination of the Structure of Boron

in "Amorphous" Boron Filaments

by

Harry A. Lipsitt*

Abstract

An X-ray and electron microscopic study of boron filaments has shown that the boron is not "amorphous" as suggested by others. We have shown the boron to be a layered crystalline structure with extensive faulting in the layer stacking. The influence of structure on boron filament potential will be discussed.

Introduction

"Amorphous" boron filaments have recently been the subject of considerable interest. However, the main interest in these filaments has been because they are available today in quantity and with reasonable quality control. Thus, they have been an ideal filamentary material to use in studies designed primarily to learn more about the science and technology of composite structures.

It is also important, however, to learn as much as possible about the very nature of these filaments. Considerable knowledge about their structure would help immensely in understanding their porperties. And once having discerned the relationship between properties and microstructure, one can predict the influence of many variables on the resulting mechanical properties of the filaments.

Such an approach was recommended by the USAF Scientific Advisory Board in the report of their Ad Hoc Committee on Boron Research in July 1964. In October 1964 the present author began just such a study at the request of and with the full cooperation of Dr. A. M. Lovelace, Chief Scientist of the Air Force Materials Laboratory. The first results of that program were presented in an unpublished report (1) to Dr. Lovelace and interested members of the AFML in April 1965.

---

*Dr. Harry A. Lipsitt is Supervisor, Metallurgy Research, Metallurgy and Ceramics Research Laboratory, Aerospace Research Laboratories, an element of the Air Force Office of Aerospace Research located at Wright-Patterson Air Force Base, Ohio.

That research report indicated clearly that the boron was an imperfect layer structure - although the nature of the imperfections remained an uncertainty at that time. Later in 1965 the present author described some of his results to Dr. Henry Otte, Manager, Metals Research Laboratory, Martin-Orlando. Dr. Otte was doing some similar research with silicon carbide filaments and was very interested in our results on boron. We began a cooperative investigation of boron in July 1965 and completed that investigation with the submission for publication of a joint paper in November 1965 (2). The conclusion of that paper is clear; such boron is not amorphous, but is a layered crystalline structure with extensive faulting in the stacking sequence of the layers.

The present paper is a brief summary of the more pertinent results described in the two previous references (1, 2). The information was obtained by examination of boron, vapor deposited on tungsten filaments using current deposition practices. The boron was studied with the electron microscope as well as by X-ray diffraction.

Experimental Techniques

The boron examined here was prepared by Texaco Experiment, Inc., using a vapor thermal decomposition process in which the pure element was deposited onto a 12μ diameter tungsten filament. Samples for X-ray and electron microscope study were prepared by crushing the filaments with a mortar and pestle, and also by rolling between two glass plates. This procedure is satisfactory, since the boron is brittle and cleaves or fractures without any significant amount of plastic deformation.

The crushed material was placed on grids (with or without a substrate of vacuum evaporated carbon 50 to 100 Å thick) and examined in the electron microscope. For the X-ray diffraction studies a 114.6 mm diameter Debye-Scherrer (film) camera was used and filtered copper K_α radiation.

X-Ray Diffraction Observations

The boron from the crushed filaments showed (in addition to the expected boride lines) only 4 very diffuse maxima (or halos) at d-spacings of approximately 4.4, 2.5, 1.75, and 1.4 Å (Table 1). Diffraction patterns were recorded at elevated temperatures (900, 1000, 1100 and 1200°C) by heating (for 2 hours) a bundle of filaments in an evacuated Unicam high temperature X-ray camera. The results indicated that the "amorphous" structure was stable up to 1000°C, began to transform at

1100°C, and transformed quickly at 1200°C to the β-rhomobohedral form. Several filaments were also encapsuled in an evacuated quartz capillary and heated for 50 hours at 1000°C, after which they were powdered and X-rayed. The three stronger halos were observable as well as lines attributable to WB_2 and W_2B_5. Thus the as deposited structure of the boron is thermally stable at 1000°C over extended periods.

Electron Microscope Observations

Samples obtained from the crushed filaments generally showed 3 to 4 diffuse rings in the electron diffraction pattern; these rings corresponded to d-spacings of 3.75, 2.22, and 1.20 Å; or 4.37, 2.19, 1.72, and 1.42 Å; or 4.51, 2.62, 1.76, and 1.45 Å (Table 1). Spot patterns could also be observed. In many cases these could be attributed to tungsten borides. In other cases a hexagonal array of diffraction spots was obtained, as shown in Fig. 1. When a sample, yielding such a pattern, was tilted over ± 30°, using the goiometer stage in the electron microscope, the hexagonal array of diffraction spots remained. In one particular case a sequence of such patterns, with the specimen at different tilts, was photographed. Enlargements were made from the plates on low distortion paper and the three angles between the principal directions (containing the closest spaced spots) were measured on the photographic paper. The results are presented graphically in Fig. 2. A simple indexing in terms of the known structures for boron could not be made (2). Furthermore, the fact that the hexagonal pattern persisted over the full range of tilting indicated a continuous intensity distribution in a certain direction, corresponding to relrods (reciprocal lattice rods) in reciprocal space along what may be identified as the c* direction of a layer-type structure.

The regions showing diffuse rings transformed on heating sufficiently in the electron microscope by removing the condenser apertures. The extent of heating could be varied using the emission current control and the second condenser. When the beam intensity was slowly increased, thereby heating the sample, the diffuse rings faded and streaked spot patterns formed. The spacing between the streaks corresponded to a spacing of 4.9 Å and so did the spacing between the spots along the streaks. This pattern could be indexed as hexagonal with $a_0 = 9.8$ Å and $c_0 = 24.5$ Å. The streaks in the diffraction pattern were perpendicular to the striations in the image as would be expected if the two effects were associated with a faulty stacking of the atomic layers. The structure thus formed has cell dimensions which are close to published values. The c_0 cell dimension falls precisely between the two values given in the literature (3, 4).

Table I

Comparison of observed d-spacings of "amorphous" boron
with calculated spacings for possible f.c.c. or b.c.c. structures

f.c.c.		b.c.c.		Observed for "amorphous" boron	References
h k l ($h^2 + k^2 + l^2$)	d(Å) calculated for $a_0 = 7.5$ Å	h k l ($h^2 + k^2 + l^2$)	d(Å) calculated for $a_0 = 6.2$ Å		
111 (3)	4.33	110 (2)	4.38	4.20-4.50	8(X), 9(X), 10(X), pw(ED, X)
200 (4)	3.75	---	---	3.75-3.81	pw(ED, X)
---	---	200 (4)	3.10		
220 (8)	2.65	---	---		
---	---	211 (6)	2.53	2.50-2.62	8(X), 9(X), 10(X), pw(ED, X)
311 (11)	2.26	---	---	2.17-2.22	pw(ED, X)
222 (12)	2.16	220 (8)	2.19		
---	---	310 (10)	1.96		
400 (16)	1.90	---	---	1.90	pw (X)
---	---	222 (12)	1.79		
431 (19)	1.72	---	---	1.70-1.76	9(X), 10(X), pw(ED, X)
420 (20)	1.68	321 (14)	1.66		
422 (24)	1.53	400 (16)	1.55		
333, 511 (27)	1.44	330; 411 (18)	1.46	1.38-1.45	9(X), 10(X), pw(ED, X)
---	---	420 (20)	1.39		
440 (32)	1.32	332 (22)	1.32		
531 (35)	1.268	422 (24)	1.266		
600, 422 (36)	1.250	---	---		
620 (40)	1.186	510; 431 (26)	1.216	1.20	pw (ED)
533 (43)	1.144	521 (30)	1.132		
622 (44)	1.131	440 (32)	1.096	1.1	10 (X)
444 (48)	1.083	530; 433 (34)	1.063		
711; 551 (51)	1.050	*	----		
*	----	631 (46)	0.914	0.91	10 (X)
733 (67)	0.916	---	---		
820; 644 (68)	0.9095	---	---		

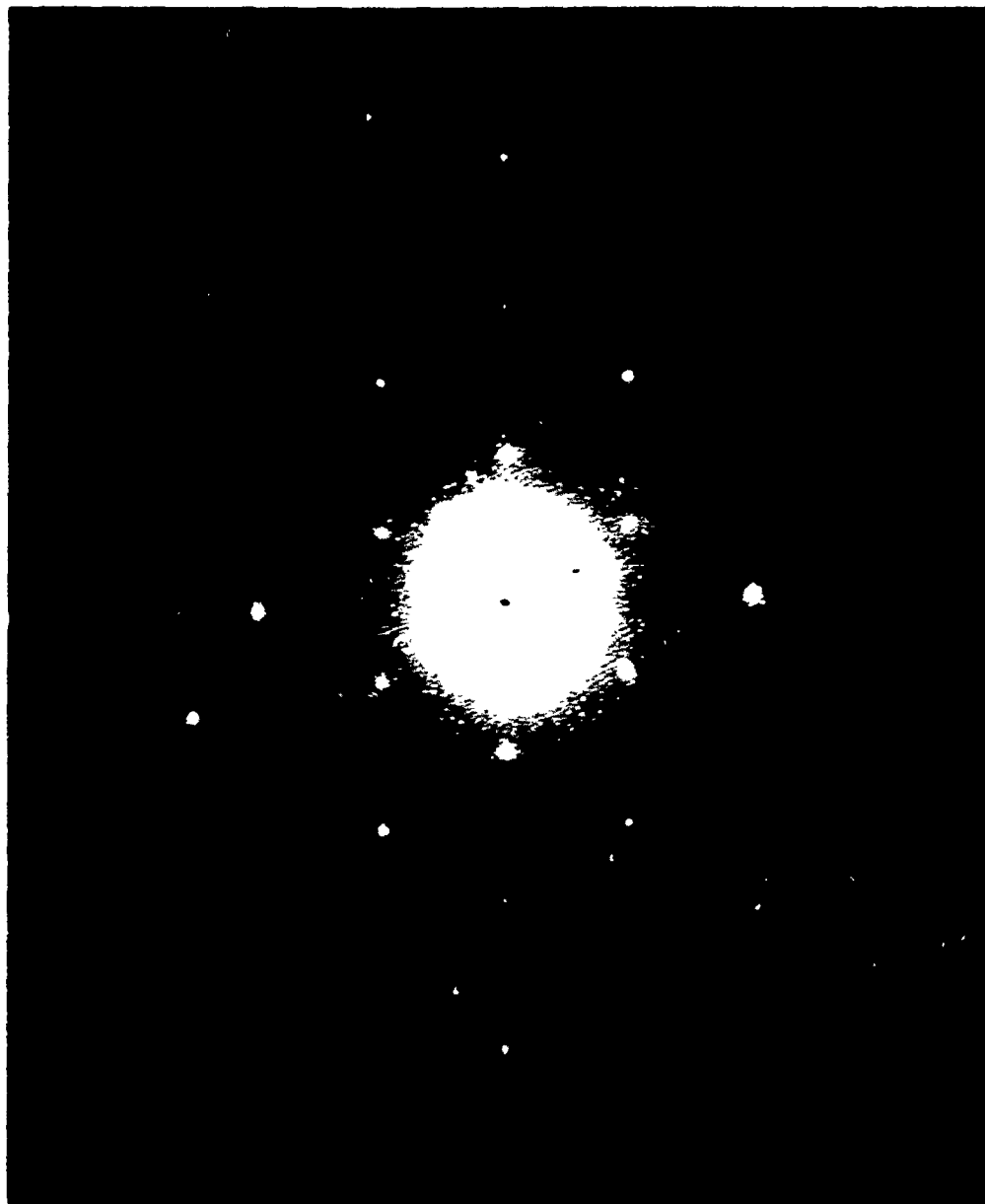pw = present work; ED = electron diffraction; X = X-ray diffraction

Figure 1. Electron Diffraction Pattern of Boron Sample Removed From Deposit Formed by Vapor Thermal Decomposition on Tungsten Filament. Hexagonal array of spots remains on tilting sample
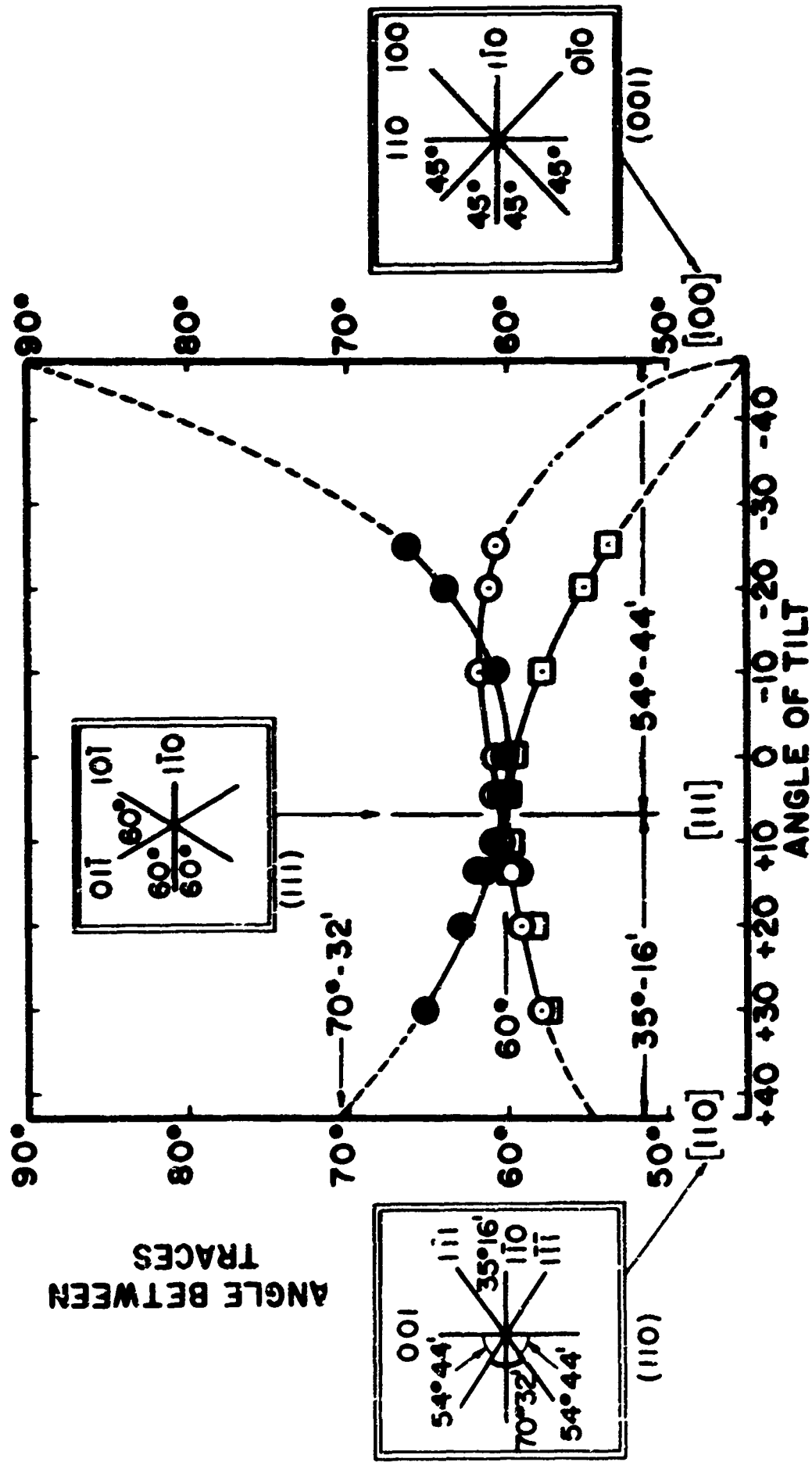
Figure 2. Variation of the Angles Between the Three Principal Direction in Spot Patterns Such as Figure 1, When a Boron Specimen Giving Such Patterns is Tilted in the Electron Beam

Discussion

The results of the tilting experiment in the electron microscope have demonstrated clearly that the boron investigated here tends to have a layer-type structure and that profuse faulting of the layers occurs. However, because of the large unit cells associated with the various boron structures, the complete analysis of the results is fairly difficult and can only be performed in part at this time.

It is possible that the few, extremely broad, diffraction lines of the "amorphous" boron could be interpreted in terms of the effects from a very heavily faulted layer structure (5). The excessive line broadening could not be explained in terms of lattice strains and particle size effects alone: the strains would be unreasonably large and the particle size unacceptably small. In view of the lack of detailed accurate measurements we will only consider here the simple possibilities of indexing the pattern as arising from an f.c.c. or a b.c.c. structure. If we index the broad lines as f.c.c. we can assign a lattice parameter $a_F = 7.5 \text{ Å}$ to the size of the cell to fit the data as shown in Table 1. The almost complete absence of 200 (and 400) would be expected for heavy faulting. High angle lines would be weak, except for cases such as 333 + 511. Qualitatively this interpretation is tenable, and the f.c.c. cell size of 7.5 Å appears to fit in well with the currently known structures of certain borides (6), in which B_{12} polyhedral groups behave like large (metal) atoms, 5.1 to 5.4 Å in diameter.

As Table 1 shows, indexing the patterns in terms of a b.c.c. would also be possible, except that the line corresponding to $d = 3.75 \text{ Å}$ would be left unaccounted for, in contrast to the f.c.c. indexing, which is therefore to be preferred. Further support for this is obtained by a consideration of Fig. 1, which can be indexed as b.c.c., f.c.c, or h.c.p. However, only an h.c.p. indexing gives cell dimensions compatible with those of the f.c.c. structure (Table 1) and therefore consistent with the supposition that we are dealing with a faulted layer structure (2).

The present observations suggest that the "amorphous" boron is in fact a heavily faulted layered crystalline structure and that upon heating (above 1000°C) "recrystallization" occurs by the annealing out of the faults. Since essentially all the faults are growth faults formed during deposition of the material from the vapor, the partial dislocations bounding the faults are grown-in, and therefore likely to be predominantly sessile in nature. Consequently, upon heating, elimination of the faults will not occur extensively by the conservation movement of the partials bounding the fault. These partials can move non-conservatively, however,

by climb and since this is a diffusion controlled process it will be temperature dependent. The faults could also be removed by the nucleation of partial dislocations which would sweep out the faulted areas. The nucleation is necessarily also temperature dependent. The structural changes on heating the deposited boron can thus be understood in terms of such mechanisms. A more quantitative evaluation would require the determination of the appropriate activation and motion energies, as well as a more detailed description of the mechanisms in terms of the crystal structures. The situation encountered most commonly in metals and alloys is one in which the octahedral, or {111}, plane of the f.c.c. structure becomes the basal, or (0001), plane of a hexagonal structure, when appropriate faulting of the octahedral planes occurs in the f.c.c. structure. The latter can be regarded as the regular stacking of layers in ABC sequence, i.e. with a repeat distance of three interlayer spacings (7). When extensive faulting occurs, this sequence is destroyed, but a new one may be established if the faulting is not entirely random.

It is important to consider the limited potential of boron filaments with a microstructure such has been defined above. An ideal material for elevated temperature use should possess a stable microstructure and derive its usefulness from these stable structural characteristics. Boron filaments on the other hand possess an unstable microstructure, which changes rapidly above about 1000°C. Further, several attempts to treat the filaments in vacuum and inert atmosphere in the temperature range 9-1300°C have resulted in the filaments losing all of their strength: after such treatment filaments are friable and powder upon handling. It is not known whether this is due to loss of boron, formation of boron oxide, or diffusion of tungsten, but it is a problem which must be studied before boron filaments are considered for an elevated temperature application. Further, boron is chemically active and being a small atom would be expected to diffuse easily and rapidly. It would appear, therefore, that the usefulness of boron filaments in metal matrixes would be limited to composites to be used at room temperature or mildly elevated temperature, and especially where the matrix is a close packed metal, and as noble as possible.

Conclusions

Boron clearly exhibits features characteristic of layer-type structures, and many of the electron and X-ray diffraction effects can be explained, at least semi-quantitatively, on the basis of extensive faulting in the stacking of the layers. The as deposited "amorphous" boron can actually

be regarded as a heavily faulted f. c. c. structure. When heated the struc-
ture "recrystallizes" to the rhomobohedral form by a mechanism proposed here to involve predominantly the elimination, or annealing out, of
the stacking faults. In addition, the basic information reported here provides considerable insight into the potential usefulness of metal matrix
boron filament composites; it is suggested that elevated temperature
applications be approached with considerable caution.

Acknowledgements

References

1. Harry A. Lipsitt, "A Study of Boron Filaments", Unpublished Report Submitted to A. M. Lovelace, Chief Scientist, AFML, 9 April 1965.

2. H. M. Otte and H. A. Lipsitt, "On the Interpretation of Electron Diffraction Patterns from 'Amorphous' Boron", to be published 1 Feb 1966, Phys. Stat. Sol. (1966), 13.

3. B. F. Decker and J. S. Kasper, Acta cryst. 12, 503 (1959).

4. D. E. Sands and J. L. Hoard, J. Amer. Chem. Soc. 79, 5582 (1957); ASTM card file No. 11-618.

5. C. N. J. Wagner, A. S. Tetelman and H. M. Otte, J. Appl. Phys. (1962), 33, p. 3080.

6. V. I. Matkovich, R. F. Giese Jr., and J. Economy, Interstitial Compounds of Boron and Transition Metals, ONR-TR3 (Contract Nonr-4075(00), Task NR056-449), Carborundum Co., Niagara Falls, N. Y., 1964.

7. S. Amelinckx, The Direct Observation of Dislocations, Academic Press, New York, 1964.

8. C. P. Talley, L. E. Line and Q. D. Overman, Boron, Synthesis Structure and Properties, Plenum Press, New York 1960 (p. 94).

9. AFSC Ad Hoc Task Force, Report of Boron Working Group; Technical Exposition on Boron Filaments and Composites, Vol. 1 Oct. 1964 (p. III-4).

10. F. Wawner, private communication, 1965.

Dr. William M. Fairbank is Professor of Physics at Stanford University, where he teaches and directs research in low-temperature physics. He has been an AFOSR grantee since 1961, and has made extensive contributions to cryogenics, particularly to the knowledge of the properties of matter near the absolute-zero temperature. After graduation from Whitman College, Dr. Fairbank participated in radar development programs at the M.I.T. Radiation Laboratory. Prior to going to Stanford in 1958, he was an Assistant Professor of Physics at Amherst College and a Professor of Physics at Duke University. He holds a Ph. D. in Physics from Yale University. In 1963, Dr. Fairbank received the American Physical Society's Buckley Prize in Solid State Physics.

FROM QUANTIZED FLUX TO A FRI PRECESSION NUCLEAR GYRO

William M. Fairbank, William O. Hamilton and C.W.F. Everitt
Department of Physics, Stanford University

This paper describes research which has led to a new understanding of one of the fundamental problems of physics and at the same time has made possible in principle a more sensitive magnetometer, a truly zero magnetic field region inside a perfect magnetic shield, a gyroscope capable of checking Einstein's general theory of relativity in a satellite experiment, and a completely new kind of guidance instrument, a free precession nuclear gyro. This gyro in turn makes possible a test of time reversal invariance, one of the fundamental symmetry laws of physics now under question.

The research to be described is part of a basic research program at Stanford in low temperature physics supported in part by the Air Force Office of Scientific Research, the National Science Foundation, the Army Research Office Durham, the Office of Naval Research and the National Aeronautics and Space Administration. In addition the development of a He^3 gyro has been supported in part by the Air Force Aeronautical Research Laboratory and the Air Force Avionics Laboratory.

One of the aims of the research at Stanford is to understand the peculiar behavior of certain kinds of matter near the absolute zero of temperature, particularly the properties of metals known as superconductors. It is well known that some metals, including at least a thousand alloys, lose all of their electrical resistance when their temperature is lowered near to the absolute zero. Physicists have struggled for years to devise a theory which would explain the peculiar properties of these superconducting metals. In 1947 F. London [1], in his book "Superfluids, Vol. I", suggested that perhaps the electrons in a superconductor were locked together in a strange state of long range order in their motion such that all of the superconducting electrons collectively behaved much as a single electron in an atom, that they were in a single macroscopic quantum state.

London suggested that as a result of this long range order in the momentum of the electrons, flux in a superconducting ring might be quantized, that is, in a ring of a certain size only certain magnetic

fields could be trapped. The size of the flux quantum, 4×10^{-7} gauss cm^2, was long felt to be impossibly small so measurements were not attempted until the late 1950s. In 1961 Deaver and Fairbank [2] at Stanford and independently Doll and Näbauer [3] in Germany, discovered experimentally that the flux that could be trapped in a superconducting ring was indeed quantized. However, there was a very important exception to the London prediction. Whereas London had predicted that the size of the flux quantum would be 4×10^{-7} gauss cm^2 the measured value was 2×10^{-7} gauss cm^2. This factor of 2, which is due to the pairing of electrons in a superconducting material, provided a very substantial verification of the 1957 theory of Bardeen, Cooper and Schrieffer [4], which is a microscopic theory of superconductivity.

A particularly striking demonstration of flux quantization in a superconducting cylinder is shown by the data in Fig. 1 taken by Deaver and Kwiram at Stanford [5]. The experiment was performed on a superconducting cylinder of tin, 40μ o. d. with 1.5μ walls. The cylinder was arranged such that it could be periodically heated and cooled through its transition temperatures at a frequency of 20,000 cycles per second. When the cylinder is cooled from the normal into the superconducting state, one would expect the flux to be excluded from the walls of the cylinder by the Meissner effect, and the flux in the hole to assume the value of the nearest quantum of flux. That this happened at a frequency of 20 kilocycles is very dramatically shown in the data on Fig. 1. The ordinate shows the output voltage across the terminals of a coil wrapped around the superconducting cylinder. The abscissa shows the axial magnetic field which was gradually increased as the cylinder was periodically cooled and heated at 20 kilo - cycles through the transition temperature. The gradual increase in signal as the magnetic field is increased is caused by the Meissner effect in the walls of the cylinder, that is, all the flux is excluded from the wall of the cylinder. The periodic fluctuations in the signal reflect the periodic trapping of increasing integral units of quantized flux in the central hole of the cylinder. From the cross section of the cylinder and the strength of the magnetic field the flux quantum is measured and agrees to within 1 percent with half the London value. This suggests a new kind of a magnetometer. The Meissner effect in the walls of the cylinder gives the total value of the flux. The periodic variation in the quantum of flux gives an absolute sensitive calibration of the change in the magnetic field. We have modified this circuit into a magnetometer theoretically capable of measuring 10^{-11} gauss and plan to use this detector to detect the orientation of a superconducting gyroscope in space and the orientation of He^3 nuclei in a He^3 nuclear gyro which will be discussed later.

The discovery of quantized flux has led to a whole new set of experimental and theoretical investigations and has given a deeper understanding of the nature of the superconducting state. In addition, from a practical standpoint it has made possible, for the first time,

the attaining of a truly zero magnetic field. When a solid perfect type I superconductor is cooled through the transition temperature into the superconducting state it excludes all the magnetic flux; this is known as the Meissner effect. However, all actual solid superconductors tend to trap some flux and all superconductors which contain a hole, such as a hollow cylinder or sphere trap approximately the flux originally contained in the hole. After the superconductor is in the superconducting state the amount of trapped flux remains constant even if the external field is changed. In the experiments of Deaver and Fairbank they observed that the flux trapped in the hole in a small superconducting cylinder is quantized. In particular, they observed that if the cylinder is cooled down in a magnetic field of such a size that the flux in the hole of the cylinder is less than half a flux unit no flux at all is trapped in the hole. Thus it is possible to obtain a truly zero magnetic field inside a hollow superconducting shield provided the shield is cooled through its transition temperature in a magnetic field sufficiently small that the total flux passing through the shield is less than half a flux unit.

London's theory also predicted another interesting property in a superconductor. He predicted that if the superconducting material were rotated it would spontaneously develop a magnetic moment along the direction of the spin axis. This magnetic moment has been called the London moment. If a body is rotated at a frequency ω, the London moment is such that it will develop a spontaneous magnetic moment along the direction of spin of $10^{-7}\omega$ gauss. The existence of the London moment was demonstrated in 1964 by Bol and Fairbank [6] at Stanford, supported by AFOSR, and also by Hildebrandt [7], and by King, Hendricks and Rorschach [8]. The experimental evidence agrees very closely with the predictions of the London theory, see Fig. 2. The existence of the London moment makes possible a novel and very sensitive readout for a gyroscope as will be described below.

L. I. Schiff [9] has proposed an experiment to check the equations of motion in Einstein's general theory of relativity by means of a gyroscope which is forced to go around the earth either in a stationary laboratory fixed to the earth or a satellite. The early efforts of our research under AFOSR were directed towards designing an apparatus to perform this experiment with the expectation that the final experiment would be financed and flown by NASA. Schiff has calculated from Einstein's general theory of relativity that a perfect gyroscope subject to no external torques will experience an anomalous precession with respect to the fixed stars as it travels around the earth. A second anomalous precession arises due to the rotation of the earth. The relativity effect on a gyroscope in a satellite in a 500 mile polar orbit is illustrated in Fig. 3. The spin axis of gyro 1 is parallel to the axis of the earth and at right angles to the axis of the orbit. The predicted precession of such a gyroscope is 7 seconds of arc per year in the direction shown. This is the effect due to rotation 15 times a day about the earth. The axis of gyro 2 is oriented parallel to the satellite
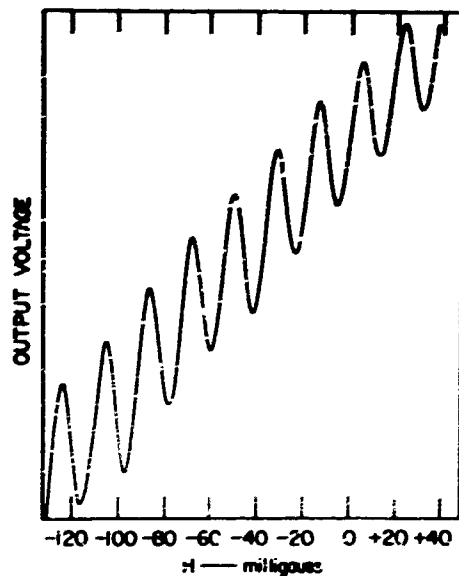
Figure 1. Voltage Picked up by a Coil Wrapped Around a Hollow Cylinder Which is Driven Alternately Superconducting and Normal at 20,000 cps in an External Field. The periodicity is due to flux quantization in the hollow cylinder. From Deaver and Kwirim, Reference 5
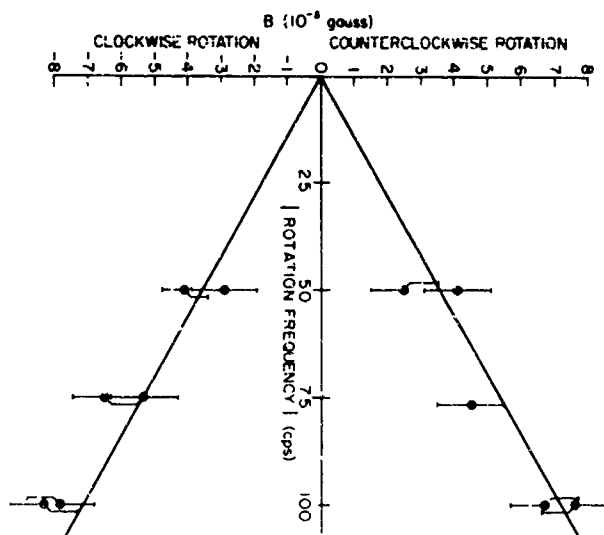

Figure 2. The Original Data Illustrating the Existence of the London Moment. The line is that predicted by London. From Bol and Fairbank, Reference 6

orbit and at right angles to the axis of the earth. The predicted precession of the axis of this gyro due to the rotation of the earth is 0.05 seconds of arc per year in the direction shown in the diagram. Under the conditions shown the two effects do not interfere.

An experiment performed to an accuracy of 0.01 seconds of arc per year would adequately check both effects. It would give a completely new check to the general theory of relativity. We have addressed ourselves to the problem of how such a gyroscope can be made. It should be capable of being readout to 0.01 seconds of arc and should have a drift rate due to all external torques of less than 0.01 seconds of arc per year.

Because of the necessity of supporting the gyroscope against the gravitational pull of the earth it is impossible to make a mechanical gyroscope on earth which approaches within several orders of magnitude these requirements on drift rate. However in a satellite it is possible to reduce the effective gravitational field sufficiently to reduce the support torques to the required level. The gravity-gradient torques which exist on any gyroscope which is not perfectly spherical remain as large in the satellite as they are on earth. To reduce the dirft from these torques to less than 0.01 seconds of arc per year it is necessary to have the ball as nearly as possible perfectly spherical. This poses a readout problem. Conventional readouts require knowing the position of the axis of rotation with respect to the ball. If the moments of inertia of all the axes of the ball are the same it is impossible to anticipate about which axis the gyroscope will spin.

The London moment provides a unique way of solving this readout problem. As we mentioned earlier, a spinning superconductor produces along its axis of spin a magnetic field of $10^{-7}\omega$ gauss. With a gyroscope spinning at an ω of 4×10^3 radians/sec this would give 4×10^{-4} gauss along the axis of spin. The question then arises how can one detect to .01 seconds of arc the orientation of such a gyroscope by use of this very small magnetic field. Figure 4 shows the proposed readout which makes use of a superconducting loop. Shown in the figure is a spinning superconductor with a magnetic field as indicated along the axis of the spin. Around the spinning sphere is placed, as a method of readout, a superconducting loop. Since the resistance of the superconducting loop is zero, any change in the flux through the loop caused by a change in orientation of the gyro-sphere will cause a current to flow in the loop which exactly cancels this change of flux. If one could read out this current, one could determine the change in orientation of the direction of the ball. Figure 5 shows the method we have developed to read out this current. In series with the first loop is placed a second superconducting loop indicated with an arrow through the loop. The current that flows in the two superconducting loops now produces a cancelling flux which is distributed in the two loops instead of being confined to the one loop. The ratio of the flux in the two loops is equal to the ratio of the inductances of the two loops. Thus the change in flux through the first loop caused by the reorientation of the
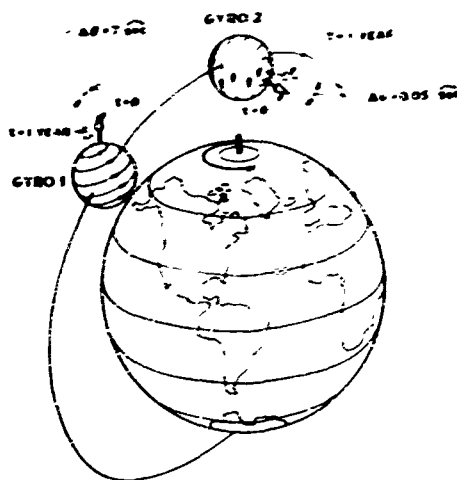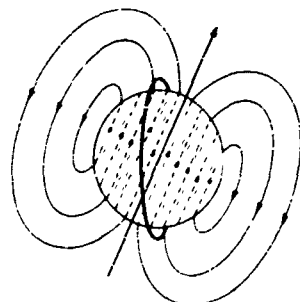
Figure 3. Relativistic Precessions of Gyroscopes in 500 mile Polar Orbit

Figure 4. Principle of London Moment Readout

ball produces a cancelling flux distribution in the two loops. If the inductance of the second loop is changed, the current flowing in the two loops changes and the distribution of the cancelling flux in the two loops changes. If the inductance is changed one million times per second then a one megacycle AC signal is produced which can be detected by a readout coil. Figure 6 shows such a circuit, including a readout and a nulling field. The modulator consists of a long super-conducting lead evaporated on the surface of a quartz crystal. Adjacent to this ' ʋ superconducting wire, is a superconducting ground plane evapoɪ .. ɔn a second crystal. The crystals placed about 2000 angstroms apart, are run in push-pull operation in the fundamental thickness mode such that the ground plane periodically approaches and recedes from the superconducting circuit. This modulates the inductance of the circuit and causes the flux to be pumped back and forth between the two loops. The oscillating current in the two loops flows through the coil as indicated and is read out through a transformer by an amplifier. It is possible to increase the sensitivity of this circuit by placing a condenser in the circuit as indicated on the diagram. The modulating current flows in and out of the condenser plates in such a way as to provide additional parametric amplification. John Pierce at Stanford has worked out in detail the sensitivity of such a circuit compared with the theoretical Johnson noise in an amplifier. It is given by the following equation:

$$\Phi^2 \geq \frac{27\pi}{16} \ \frac{L}{Q} \ (\frac{L}{\Delta L})^2 kT \ \frac{\Delta \nu}{\nu}$$

where L is the total inductance of the circuit, ΔL the inductance change, T the noise temperature of the circuit, Q the quality factor of the circuit, ν the frequency of modulation, and $\Delta \nu$ the bandwidth. We have verified the validity of this equation both with experiments and by model circuits on an analog computer. With the modulating crystal operating at 1 megacycle and a Q of 100, with room temperature amplifier noise figure the sensitivity is predicted to be 10^{-10} gauss which would allow an accuracy of readout of 0.10 of a second of arc. By averaging over a year or by reducing the noise temperature in the receiver to helium temperatures the sensitivity can be increased to at least 0.01 seconds of arc as required by the experiment.

Figure 7 is a diagram of the gyroscope. The gyroscope will consist of a very homogeneous quartz ball, 1-1/2 inches in diameter coated with a thin layer of niobium. The ball is made as spherical as possible. It is electrostatically supported across a supporting space of 1 1/2 thousandths of an inch. The ball is spun up in the super-conducting state by helium gas spin up jets. The ball is normally operated in a vacuum with no friction. The readout system introducing essentially no losses in the ball. The ball is kept cold by black-body radiation to the walls. Surrounding the entire gyroscope is a super-conducting 4-inch diameter spherical shield from which the last quantum of flux has been excluded. This is absolutely necessary if one is to
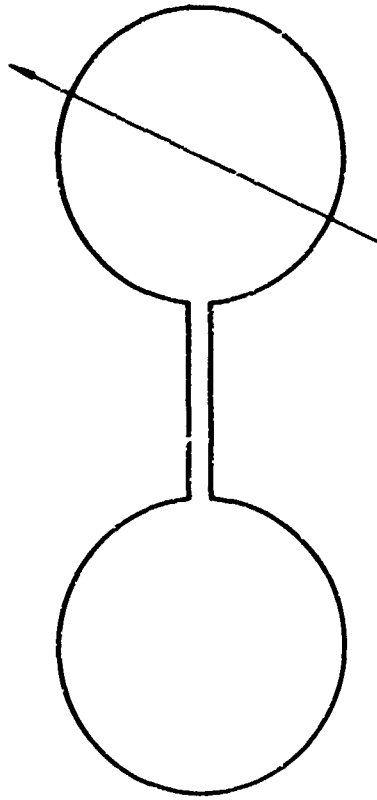
Figure 5. Schematic Illustration of the Superconducting Detection Circuit. The arrow indicates that the inductance of that loop can be varied periodically
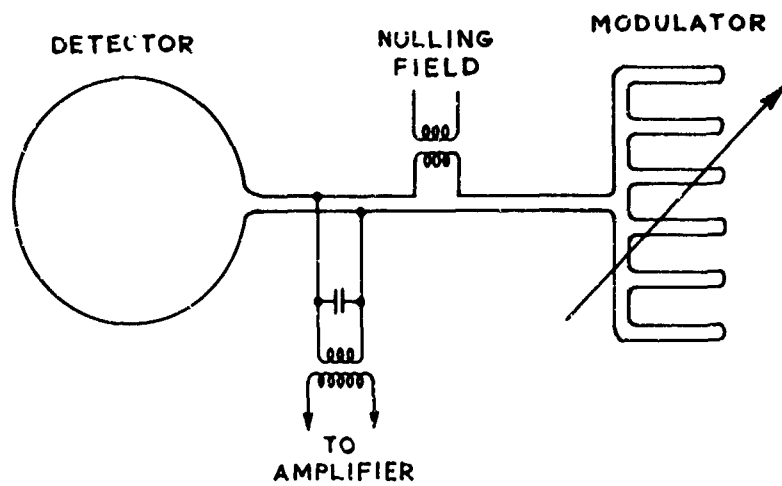

Figure 6. The Detection Circuit as it will be Used for the London Moment Readout and Readout of the Nuclear Gyro

make use of the sensitive magnetic readout discussed above. The readout loop is evaporated on an optically flat piece of quartz which is made an integral part of a telescope as shown in Fig. 8. The telescope will be used to compare the axis of the gyroscope with the position of the star. Both the telescope which is made of quartz and the gyroscope will be operated at liquid helium temperature. Since the temperature will be kept very constant and since the coefficient of expansion is nearly zero there should be no change in the relative orientation of the telescope and gyro readouts to within 0.01 seconds of arc. We have calculated all the known torques on the above gyroscope in a 500 mile polar orbit and find the net drift rate to be less than 0.01 seconds of arc per year. The gyroscope and telescope parts are being constructed by Honeywell and Davidson Optronics.

Figure 9 shows a proposed complete experiment including the helium dewar used to produce a low temperature environment. Included in the experiment are 4 gyroscopes, 2 checking the rotational effect of 7 seconds per year, and 2 checking the earth's rotational effect of 0.05 seconds per year. The entire dewar contains about 75 lbs liquid helium which is calculated to keep the experiment cold for more than a year. In order to protect the superinsulation which contains about 150 layers of aluminum foil separated by nylon setting during take off, the entire dewar is supported inside a vacuum shield by inflatable pillows as indicated in the diagram. These are inflated just before take off to atmospheric pressure and supply both a shock mount and sufficient support to allow the helium contained experiment to survive take off. In orbit the pillows are evacuated to space. The superinsulation then fluffs out from 3 inches to 4 inches and provides sufficiently good insulation to keep the helium for a year. Interspersed between the layers of insulation are flexible copper shields which are gas cooled from the escaping helium. It is suspected that such a dewar could be a prototype for other low temperature experiments in space. It is essential if liquid helium alone is used, that the amount of power dissipated at helium temperatures be kept below 0.01 watt for a one year experiment. The total losses in all the readout circuits will be less than 0.01 watt. After initial support by AFOSR, NASA is supporting this project.

Although the relativity experiment on earth requires a gyroscope millions of times more sensitive than any existing gyroscope it is interesting to contemplate whether there is any possibility at all of building an earth-bound gyroscope sensitive enough to do the experiment. For many years it has been realized that a spinning nucleus is a gyroscope which is unaffected by the usual torques caused by the necessity of supporting the gyroscope against the forces due to gravity. Schiff and Currin [10] have demonstrated theoretically that nuclei are subject to the same relativity precessions as regular gyros. The question arises, could nuclei be used as a gyroscope? Two kinds of nuclear gyroscopes are possible. One is a rate gyro, which would be slaved to an external magnetic field, the other is a free precession
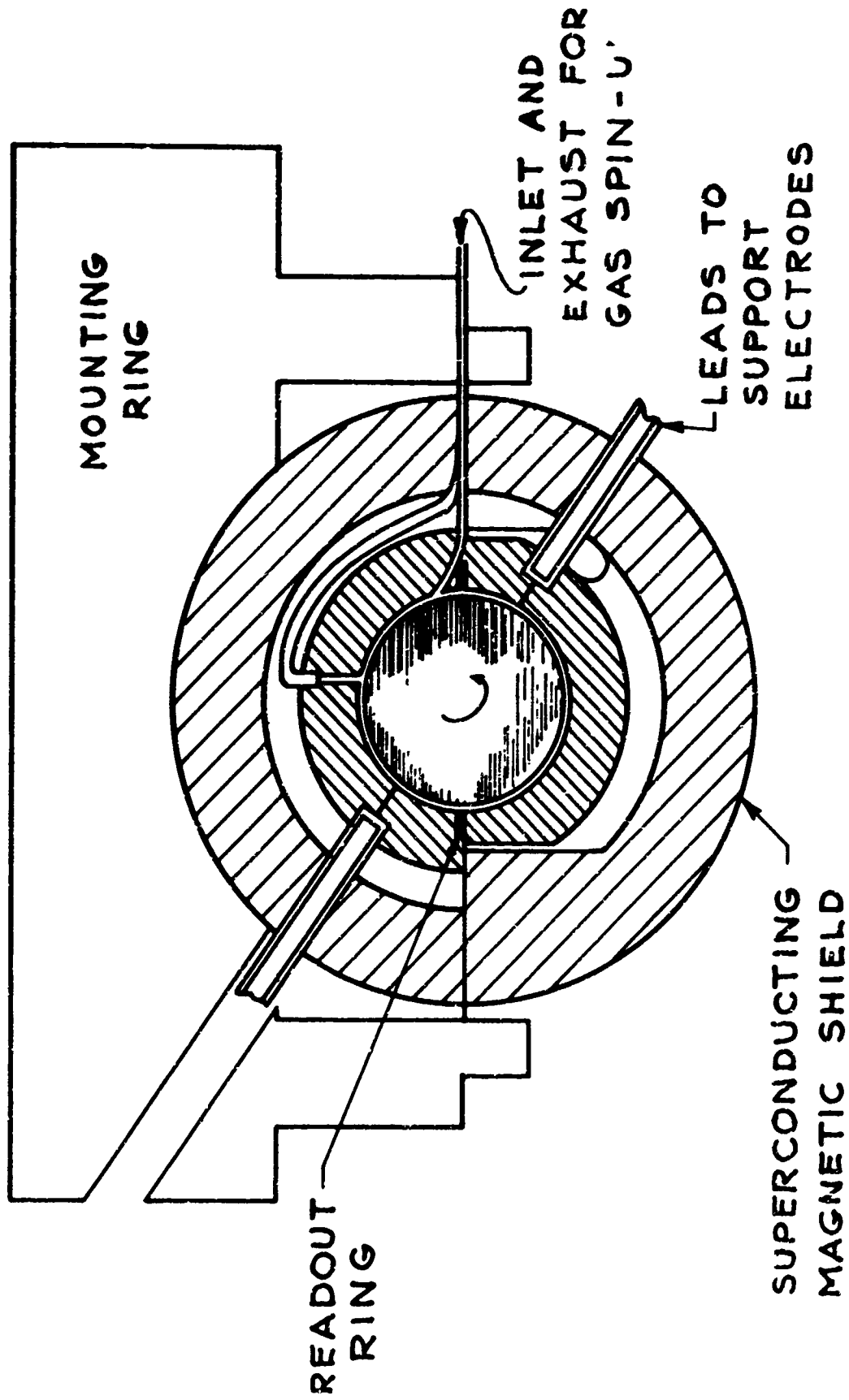
Figure 7. Gyroscope for Laboratory Test of Relativity Experiment

MOUNTING RING

INLET AND EXHAUST FOR GAS SPIN-U'

LEADS TO SUPPORT ELECTRODES

READOUT RING

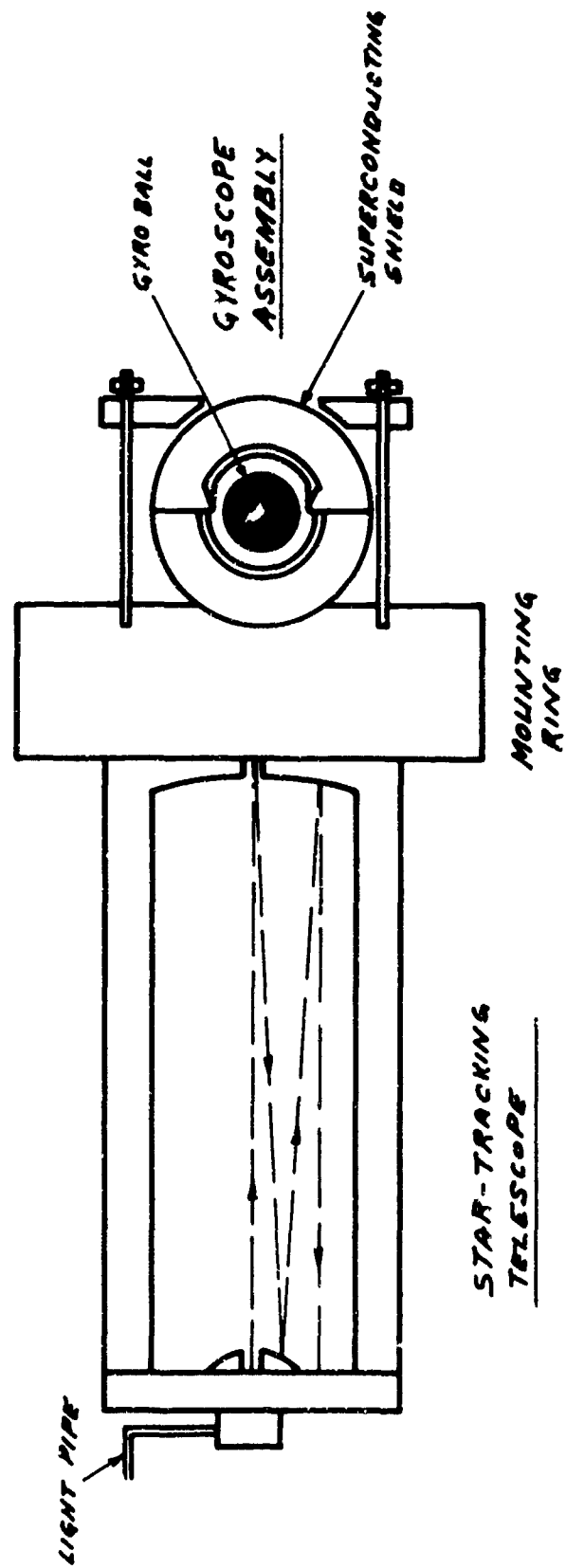SUPERCONDUCTING MAGNETIC SHIELD

Figure 8. Gyroscope and Telescope Mounted Together for Laboratory
Test of Relativity Experiment

gyro. A rate nuclear gyro using water nuclei has been constructed. But in the relativity experiment we are interested only in a free precession gyro which will remain unaffected by all external torques.

There is, however, one overwhelming torque, which is the torque due to an external magnetic field. In contrast with the London-moment superconducting gyroscope which is very heavy and produces a very weak magnetic field along its axis, a nucleus is extremely tiny and produces, relatively speaking, a very large magnetic field along its axis. Thus a very weak external field oriented in any other direction than along the axis of spin will produce a torque. In fact, a magnetic field oriented at right angles to a He^3 nucleus will cause a precession of 2×10^4 radians per second per gauss. To do the relativity experiment with an He^3 nuclear gyro one would require in an earth bound laboratory at Palo Alto, California, a magnetic field less than 5×10^{-18} gauss in order that the magnetic field produce a precession of less than 7×10^{-14} radians per second as predicted by the relativity effect. Previous proposals for free nuclear gyroscopes have not been successful because of the impossibility of making the ambient field sufficiently small. With the discovery of quantized flux it has suddenly become possible to produce a truly zero magnetic field. We have demonstrated this in the initial experiment of Deaver and Fairbank as previously described.

Figure 10 shows a diagram of the proposed He^3 gyroscope. In order to have a free precession nuclear gyro that will be readable for a period of a year it is necessary that the relaxation times T_1 and T_2 of He^3 nuclei be longer than a year. The nuclei must be first polarized so that essentially all their spins point in the same direction. It must be a liquid or gas in order that the magnetic fields of the neighbors are effectively cancelled out giving a long T_2. It must have sufficiently small magnetic field due to the electrons that the relaxation time T_1 is as long as a year. Only one nucleus satisfies the requirements for such a free precession gyro. The He^3 nucleus has an inherent relaxation time in pure liquid He^3 of about 500 seconds. If the He^3 is diluted by the completely non-magnetic He^4, the relaxation time can be made longer linearly with the percent dilution [11]. Thus a solution of 1 part of He^3 in 10^5 parts of He^4 would have relaxation times longer than a year. The He^3 nuclei can be polarized either by an optical pumping method [12] or by cooling them to $0.01^\circ K$ in a field of 100 kilogauss. Completely polarized He^3 nuclei of the desired concentration will produce along their axis of spin a magnetic field of about 10^{-5} gauss which is an order of magnitude smaller than the magnetic field expected from the superconducting gyro designed for space.

The detection circuit designed for the relativity experiment using He^3 nuclei as gyroscopes presents a very difficult experimental problem. Not only must one be able to detect the orientation of the He^3 nuclei to within a few hundredths of a second of arc over a period of a year, but the detection circuit must not produce a magnetic disturbance
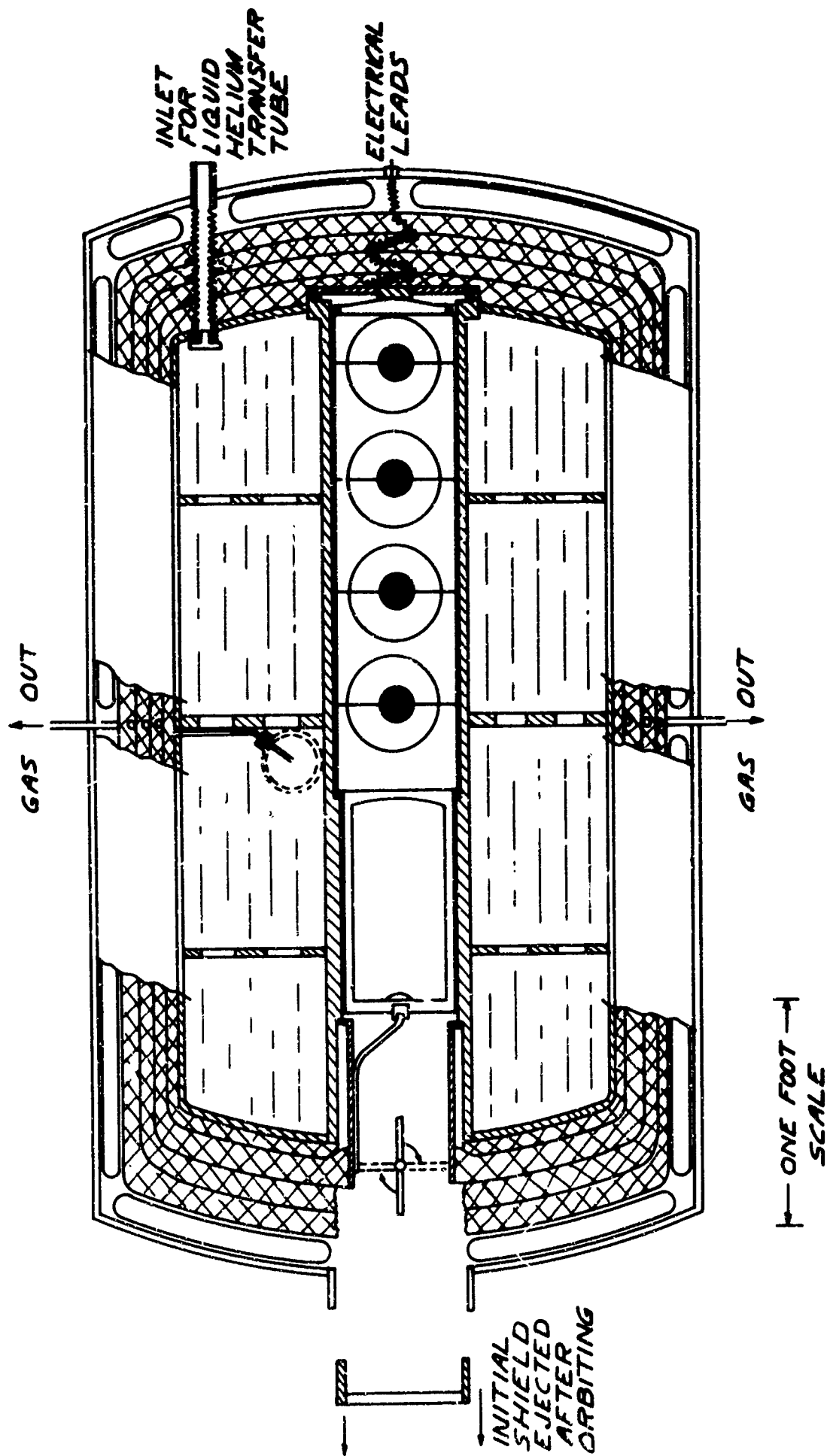
Figure 9. Flyable Low Temperature Apparatus for Relativity Experiment

which reacts back on the He^3 nuclei sufficiently to mask the He^3 precession. Such a detection circuit is uniquely made possible by the discovery of quantized flux. Basically, this circuit is the same one described for the superconducting gyroscope in space. However, an additional property makes this circuit valuable for the He^3 gyro. It is possible to make the loop normal or superconducting by changing the temperature of a portion of the loop. When the loop is made completely superconducting a current will flow such that the current through the loop is changed to the nearest integral flux unit. Since the amount of flux from the He^3 nuclei passing through the loop depends on the relative orientation of the loop and the direction of the magnetization of He^3, as discussed for the London moment readout, a measure of this current determines the relative orientation of the loop and the He^3. The direction of the magnetization of the He^3, will be as nearly as possible in the plane of the loop. Under these conditions the flux from the He^3 will be less than half a flux unit and the current will flow so as to make the net flux passing through the loop zero. Since this current will produce a magnetic field to cause the He^3 nuclei to precess, the loop will be kept in the non-superconducting state except during brief periods when a measurement is being made. Because of quantized flux, for small angular displacement of He^3 the current will always be that required to give zero flux through the loop. Thus a measurement of the current will provide an absolute reference even though the current is turned off for most of the time. This assumes a sufficiently long relaxation time for the He^3 which can be obtained as described above. The effect of the readout on the He^3 nuclei can be further reduced by a nulling circuit as shown in the diagram for the gyroscope in space. It may be possible in fact to develop a He^3 gyro that for most purposes can be continually read out.

The magnetic shield which surrounds the He^3 must be very carefully made because although all the flux has been excluded from the surrounding shield, the magnetic field produced inside the shield will still be reflected back on the nuclei. Hence all ferromagnetic material must be removed from inside the shield. In addition, the He^3 itself produces a magnetic field which will be reflected back by the shield. If the shield is completely symmetrical it will not cause any change in the alignment of the nuclei. However, if the shield and the nuclei are symmetrically placed with respect to each other or if the shield is not perfectly spherical, the reflected field can cause a precession of the He^3 nuclei. Davidson Optronics Inc. is making the gyroscope parts, the sphere is a solid fused quartz sphere, 11 1/2 inches in diameter, spherical to a few millionths of an inch. The hole in the center is about 4 millimeters in diameter. The He^3 will be polarized as mentioned above and condensed through a small capillary into the hole. The readout loop is evaporated on optically flat quartz and is sufficiently thin so as not to interfere with the orientation of the He^3 nuclei. It is estimated that a field reflected from the sphere back on the nuclei will have a disturbing effect equivalent to less than 10^{-14} gauss, and eventually it may be possible to make the apparatus sufficiently perfect to do the relativity experiment. However, long before the
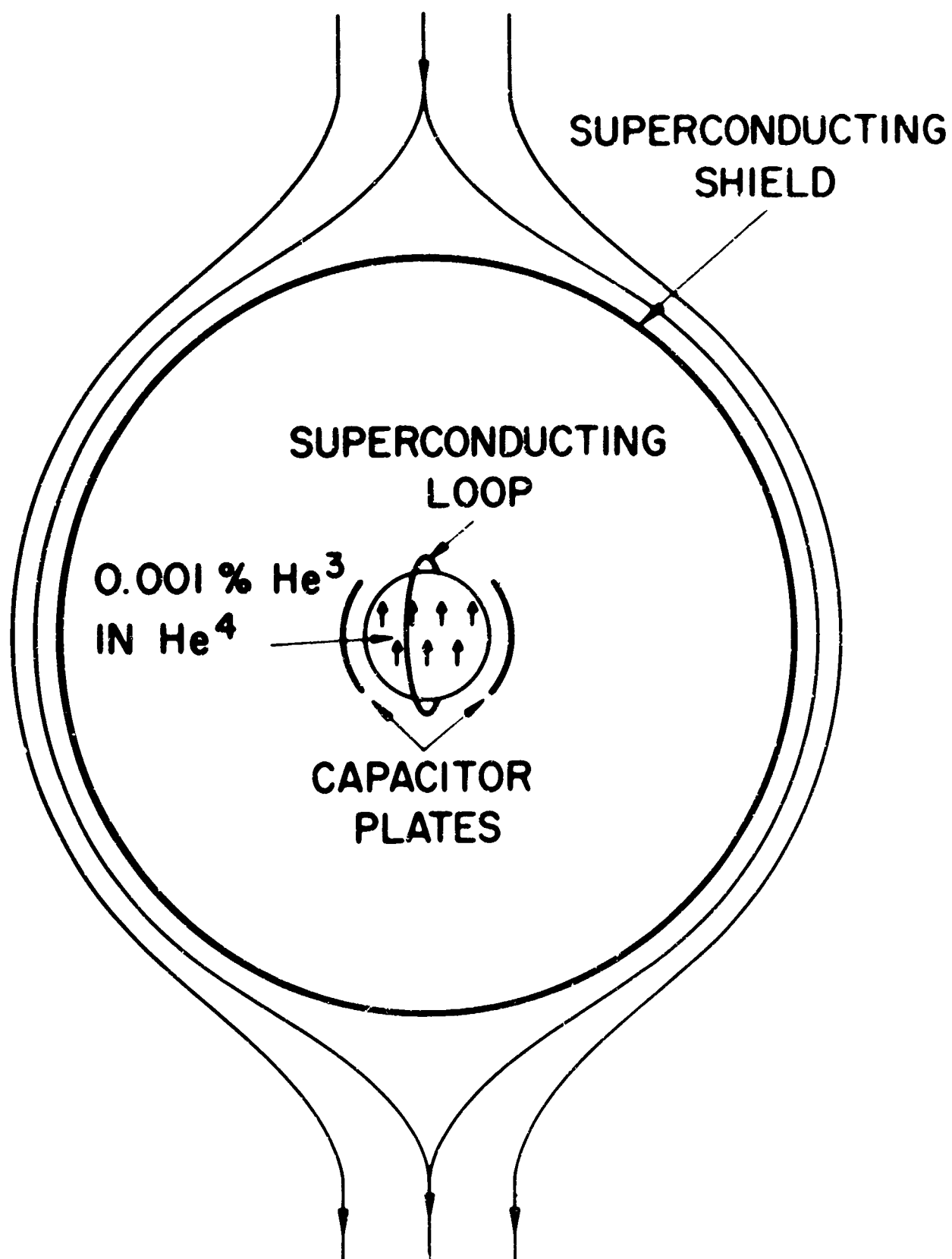
Figure 10. Schematic of the Free Precession Nuclear
Gyroscope. The condenser plates are for use in the
experiment to seek nuclear electric dipole moment

relativity experiment is accomplished it is possible to perform another very exciting experiment.

A very exciting experiment in physics at the present time would be an experiment to see if the nuclei are really perfect gyros. If the positive and negative electric charges in the proton or the neutron are slightly displaced from each other, then an external electric field placed on the nucleus would cause the nucleus to precess. We would say that the nucleus had a permanent electric dipole moment. Such a permanent electric dipole would violate the principle of time reversal invariance which has been found to be valid in every previous experiment in physics until a recent experiment in high energy physics at Princeton [13]. From these experiments it appears possible that time reversal invariance is violated in the weak interactions or in the electromagnetic interactions. If this is true then it may be possible that the He^3 nucleus is not a perfect gyroscope and an experiment to test this would test the fundamental symmetry laws of physics. To perform such an experiment, condenser plates will be placed around the He^3 as shown in Fig. 10. Between these condenser plates can be placed an electric field of a few hundred thousand volts/cm. This will cause the nucleus to move off center in the atom. The electric field itself, of course, will be exactly cancelled, because the nucleus must find itself in a zero-force field. However, there will be a field gradient and just as gravitational field gradients in the satellite experiment would cause a torque on the gyroscope if the gyroscope were elliptical, so the electric gradient in the atom will cause a torque on the gyroscope if the gyroscope has a permanent electric dipole moment [14].

In the remaining part of this paper we will describe how we expect to obtain regions of zero magnetic field. It will be recalled that when flux is trapped in a superconductor it is trapped in integer quanta. We have already pointed out that if the magnetic field through the super-conductor can be reduced to less than half a flux unit before the super-conductor is made superconducting, no flux will be trapped. The magnetic field can be reduced easily to 10^{-5} to 10^{-6} gauss with con-ventional magnetic shielding. Fig. 11 illustrates the method that will be used to reduce the field still further. This method consists of suc-cessive expansions of a flexible superconducting bladder, e.g., a bladder made of lead coated mylar. The bladder is initially folded to occupy as small a volume as possible. It will, when it is made super-conducting, trap the flux passing through it. When the bladder is expanded in the superconducting state the magnetic flux trapped in the lead will remain constant. However, due to expansion of the bladder, the flux lines will be expanded and the magnetic field will be decreased by the ratio of the areas before and after the expansion. If the second superconducting bladder has been placed in the center of the one pre-viously expanded it will trap less flux when it is made superconducting due to the fact that the magnetic field is decreased. If it is then ex-panded the magnetic field inside it will be further decreased. This

process can be continued until the magnetic flux through an unexpanded superconducting bladder is less than half a flux unit. The bladder, when it is made superconducting, will then expel all the flux and when it is expanded there will be no trapped flux.

Fix. 12 shows a schematic diagram of the apparatus which is now under construction for creating a region of zero magnetic field. The superconducting bladders used in this experiment are in the shape of a sock, open at the top to allow access. The hole at the top makes the requirement that these socks be long enough so that the magnetic field which enters the bladder through the hole is sufficiently attenuated at the bottom of the sock to be less than half a flux unit for an experimental magnetic shield which might be put into this low field region. The transverse magnetic fields are attenuated by 7.7 db for each radius one goes down in the bladder and longitudinal magnetic fields are attenuated by 16 db for each radius. Once the last superconducting bladder is expanded with no trapped flux it is desired to keep the apparatus in this condition permanently. This means that the dewar must be made so as to minimize the helium boiloff and thus make it economically feasible to keep this region permanently.

An experiment where it is desired to obtain zero magnetic field can be built into a dewar which is lowered into the central room temperature space depicted in the figure. The superconducting shield of the experiment is then cooled slowly through the transition temperature. Since the magnetic field region has decreased the ambient magnetic field to less than half a flux unit, when the magnetic shield goes superconducting it will trap no flux and inside the shield there will be a region of zero magnetic field.

The room temperature insert will be 30 inches in diameter, into which the He^3 gyro dewar can be lowered prior to cooling. The zero magnetic field region will also be used to prepare the magnetic shields used in the relativity gyro experiment. Because of the necessary size of the bladders the dewar will be approximately 18 feet long and 6 feet in diameter. The dewar will be made completely of non-magnetic materials: aluminum and titanium alloys. The insulation is of a new and very efficient design and the boiloff gas is utilized as fully as possible. We estimate that the dewar will boil off less than 10 liters per day. This is less than 0.3 percent per day. This dewar is now under construction by the Vacuum Barrier Corporation.

Thus we see in these experiments a very perfect example of the interplay between basic research and possible applications. Ever since the discovery of superconductivity there has been a constant question whether superconductors would in fact be practical for some real commercial application. As late as 1952 at a low temperature conference the main speaker pointed out that the field of low temperature physics was the last ivory tower field of physics. It used to be that nuclear physics was considered completely impractical, he said, but that feeling is now of course completely gone. However, the speaker
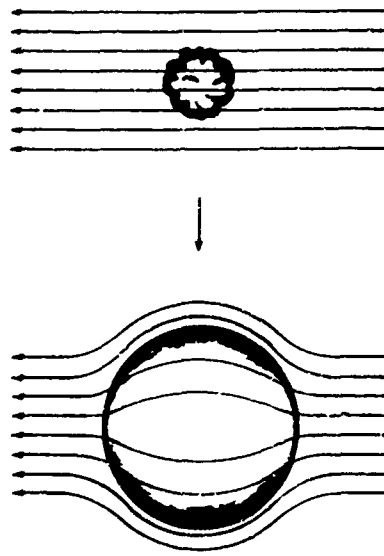
Figure 11. Principle for Obtaining Reduced Magnetic Fields by Expansion of a Superconducting Bladder
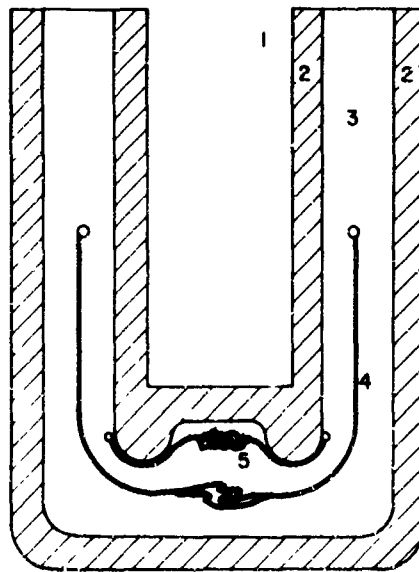

Figure 12. Apparatus for Obtaining a Zero Magnetic Field Region. Number 1 is room temperature space; No. 2 is insulation; No. 3 is the helium temperature space; No. 4 is a partially expanded bladder; No. 5 illustrates the next bladder, before expansion, kept above its transition temperature in a region filled with warm Helium gas

could not imagine any condition under which a practical use could be made of the strange effects which occur at temperatures near the absolute zero. The first breakthrough occurred in 1956 with the discovery of the Cryotron which gave promise of computer circuits using superconducting elements. It was enhanced by the development of superconducting magnets which can in principle produce fields as high as 200,000 gauss. We at Stanford are now building under ONR sponsorship a superconducting linear accelerator using superconducting cavities with a Q more than 100,000 times higher than the Q of room temperature copper cavities. Through the experiments we have described here we see that the basic discovery of one of the fundamental properties of superconductors, the property of macroscopic flux quantization, has led to the possibility of making a truly zero magnetic field region and a readout such that a free precession nuclear gyro can be made which in principle has very much smaller drift rates than any known man made gyroscope and which is unaffected by linear accelerations. The peculiar properties of a superconductor with respect to a magnetic field developed along its rotating axis and the associated perfect magnetic shields give rise to the possibility of a gyro in space which is more sensitive than any existing gyroscope. These two gyroscopes in turn make it possible for the first time a test of the equations of motion in Einstein's general theory of relativity and a new test of the fundamental symmetry law of time-reversal invariance. So we have come full sweep, a fundamental experiment makes possible a practical application which in turn makes possible a still more fundamental experiment.

REFERENCES

1. F. London, <u>Superfluids</u>, Vol. I (John Wiley and Sons, New York, 1950 and Dover Publications, Inc., New York 1961) .

2. B. S. Deaver, Jr. and W. M. Fairbank, <u>Phys. Rev. Let. 7</u>, 43 (1961).

3. R. Doll and M. Näbauer, <u>Phys. Rev. Let. 7</u>, 51 (1961).

4. J. Barbeen, L. N. Cooper, and R. Schrieffer, <u>Phys. Rev. 108</u>, 1175 (1957).

5. Alvin L. Kwiram and B. S. Deaver, Jr., <u>Proc. of IX Int. Conf. on Low Temp. Phys.</u>, Columbus, Ohio, August 31 - September 4, 1964, (Plenum Press, p. 451 1965).

6. M. Bol and W. M. Fairbank, <u>Ibid</u> p. 471.

7. A. F. Hildebrandt, <u>Phys. Rev. Let. 12</u>, 190 (1964).

8. A. King, Jr., J. B. Hendricks, and H. E. Rorschach, Jr., <u>Proc. IX Int. Conf. on Low Temp. Phys.</u> (Plenum Press, p. 466 1965).

9. L. I. Schiff, <u>Proc. Natl. Academy 46</u>, 871 (1960).

10. J. D. Currin, Ph. D. thesis, Stanford University, 1963. Thesis done under the direction of L. I. Schiff.

11. R. H. Romer, <u>Phys. Rev., 115</u>.

12. G. K. Walters, F. D. Colegrove and L. D. Schearer, <u>Phys. Rev. Let.</u>, 8 439 (1962).

13. J. H. Christenson, J. W. Cronin, V. L. Fitch and R. Turlay, <u>Phys. Rev. Let., 13</u> 138 (1964).

14. L. I. Schiff, <u>Phys. Rev., 132</u> 2194 (1963).